JOURNAL OF PETROLOGY

Journal of Petrology, 2019, Vol. 60, No. 5, 907–944
doi: 10.1093/petrology/egz020
Advance Access Publication Date: 1 April 2019
Original Article

OXFORD

Mantle Melting and Magmatic Processes Under La Picada Stratovolcano (CSVZ, Chile)

Jacqueline Vander Auwera[1]*, Olivier Namur[1,2,3], Adeline Dutrieux[1,4], Camilla Maya Wilkinson[5], Morgan Ganerød[5], Valentin Coumont[1] and Olivier Bolle[1]

[1]Département de Géologie, Université de Liège, B-4000 Liège, Belgium; [2]Leibniz Universität Hannover Institute of Mineralogy, D-30167 Hannover, Germany; [3]Department of Earth and Environmental Sciences, University of Leuven, B-3001 Leuven, Belgium; [4]Ocean and Earth Science, University of Southampton, Southampton S017 1BJ, UK; [5]Geological Survey of Norway, NO-7491 Trondheim, Norway

*Corresponding author. Département de Géologie, Université de Liège, B-4000 Liège, Belgium. Telephone: +32 4 366 2253. Fax: +32 4 366 2921. E-mail: jvdauwera@uliege.be

Received June 24, 2018; Accepted March 22, 2019

ABSTRACT

Where and how arc magmas are generated and differentiated are still debated and these questions are investigated in the context of part of the Andean arc (Chilean Southern Volcanic Zone) where the continental crust is thin. Results are presented for the La Picada stratovolcano (41°S) that belongs to the Central Southern Volcanic Zone (CSVZ) (38°S–41·5°S, Chile) which results from the subduction of the Nazca plate beneath the western margin of the South American continent. Forty-seven representative samples collected from different units of the volcano define a differentiation trend from basalt to basaltic andesite and dacite (50·9 to 65·6 wt % SiO_2). This trend straddles the tholeiitic and calc-alkaline fields and displays a conspicuous compositional Daly Gap between 57·0 and 62·7 wt % SiO_2. Interstitial, mostly dacitic, glass pockets extend the trend to 76·0 wt % SiO_2. Mineral compositions and geochemical data indicate that differentiation from the basaltic parent magmas to the dacites occurred in the upper crust (~0·2 GPa) with no sign of an intermediate fractionation stage in the lower crust. However, we have currently no precise constraint on the depth of differentiation from the primary magmas to the basaltic parent magmas. Stalling of the basaltic parent magmas in the upper crust could have been controlled by the occurrence of a major crustal discontinuity, by vapor saturation that induced volatile exsolution resulting in an increase of melt viscosity, or by both processes acting concomitantly. The observed Daly Gap thus results from upper crustal magmatic processes. Samples from both sides of the Daly Gap show contrasting textures: basalts and basaltic andesites, found as lavas, are rich in macrocrysts, whereas dacites, only observed in crosscutting dykes, are very poor in macrocrysts. Moreover, modelling of the fractional crystallization process indicates a total fractionation of 43% to reach the most evolved basaltic andesites. The Daly Gap is thus interpreted as resulting from critical crystallinity that was reached in the basaltic andesites within the main storage region, precluding eruption of more evolved lavas. Some interstitial dacitic melt was extracted from the crystal mush and emplaced as dykes, possibly connected to small dacitic domes, now eroded away. In addition to the overall differentiation trend, the basalts to basaltic andesites display variable MgO, Cr and Ni contents at a given SiO_2. Crystal accumulation and high pressure fractionation fail to predict this geochemical variability which is interpreted as resulting from variable extents of fractional crystallization. Geothermobarometry using recalculated primary magmas indicates last equilibration at about 1·3–1·5 GPa and at a temperature higher than the anhydrous peridotite solidus, pointing to a potential role of decompression melting. However, because the basalts are enriched in slab components and H_2O compared to N-MORB, wet melting is highly likely.

Key words: arc magmatism; Chilean Southern Volcanic Zone; Daly Gap; magma differentiation; primary magmas

INTRODUCTION

The depth and detailed mechanisms of arc magma generation and differentiation are long standing debates that are crucial to the Earth Sciences as, at least since the Proterozoic, the continental crust is mainly built at subduction zones. The thickness of the crust seems to play a determining role. It influences the thermal structure of the mantle wedge and thus the compositional variability of primary arc magmas (Plank & Langmuir, 1988; Turner & Langmuir, 2015a, 2015b; Turner *et al.*, 2016; Chin *et al.*, 2018). It also controls magmatic differentiation processes and according to Farner & Lee (2017) average arc magmas are more evolved, enriched in incompatible elements and more oxidized when the crust is thick. Finally, it determines the depth of magma differentiation; a thicker continental crust appears to promote deep crustal differentiation. It is currently acknowledged that during their transit through the crust, magmas probably stall and are stored at various depths within protracted or transient reservoirs. Yet constraining the location of prolonged storage sites is challenging. The recognition that the crust–mantle boundary could act as a density filter and induce the stalling of basaltic magmas has prompted several authors to favor deep fractionation (e.g. Annen *et al.*, 2015, 2006), a process that is indeed supported by the occurrence of lower crustal mafic and ultramafic cumulates in some arc sections (e.g. Searle *et al.*, 1999). However, petrological and geochemical arguments question this model and point to the shallow crust as the main site of differentiation (e.g. Turner & Langmuir, 2015a; Adam *et al.*, 2016). A striking characteristic of arc magmas is the abundance of andesitic rocks (e.g. Wörner *et al.*, 2018), but the relative paucity of true andesitic liquids (Daly Gap) (e.g. Reubi & Blundy, 2009) compared to mafic and silicic endmembers. Several processes that have been proposed to take into account this compositional bimodality take place in the lower crust (Reubi & Blundy, 2009; Melekhova *et al.*, 2013) and, accordingly, andesitic rocks are interpreted as resulting from mingling/mixing between the two endmembers in shallow magmatic reservoirs. Lower crustal differentiation would thus be essential in producing the Daly Gap.

In this study, we focus on the central part of the Chilean Southern Volcanic Zone (SVZ) where the geochemical trends of several volcanoes, including La Picada and Osorno (Fig. 1), display a compositional (Daly) gap between dominant basaltic andesites and minor dacites. In this part of the Andean arc, the continental crust is thin (≈30 km) and its permeability is enhanced by a major regional structure, the Liquiñe–Ofqui Fault Zone, that likely facilitates magma ascent (Hickey-Vargas *et al.*, 2016a) (Fig. 1) suggesting that most of the differentiation could have taken place in the upper crust. The SVZ has been the subject of numerous studies that have mostly emphasized along arc regional trends in the eruptive products (Lopez-Escobar, 1984), correlating with geochemical trends (Deruelle *et al.*, 1983; Hickey *et al.*, 1984; Lopez-Escobar, 1984; Stern *et al.*, 1984; Hickey *et al.*, 1986; Hildreth & Moorbath, 1988; Morris *et al.*, 1990; Tormey *et al.*, 1991; Sigmarsson *et al.*, 2002; Jacques *et al.*, 2013; Hickey-Vargas *et al.*, 2016a) and were focused on the potential sources of the magmas. Specific volcanoes of the SVZ have also been investigated (e.g. Lopez-Escobar *et al.*, 1981; Lopez-Escobar *et al.*, 1995; Kratzmann *et al.*, 2010; Reubi *et al.*, 2011; Ruprecht *et al.*, 2012; Bouvet De Maisonneuve *et al.*, 2013; Higgins *et al.*, 2015; Hickey-Vargas *et al.*, 2016b; Ruth *et al.*, 2016). However, despite this abundant research, few detailed petrological studies (e.g. Ruprecht *et al.*, 2012; Watt *et al.*, 2013) that take into account the whole life cycle of a volcano and constrain the sites and conditions of mantle melting and magma differentiation have been undertaken in this part of the arc. In this study, our aims are thus : (1) to provide new detailed geochemical and mineralogical data, as well as new ^{40}Ar–^{39}Ar (hereafter Ar–Ar) ages on a collection of samples from La Picada; (2) to constrain the magma storage conditions and processes of magma differentiation under La Picada; and (3) to place additional constraints on mantle melting in this part of the arc.

THE SOUTHERN VOLCANIC ZONE OF THE ANDEAN ARC AND LA PICADA VOLCANO

The Andean arc results from the subduction of the Cocos, Nazca and Antarctica plates under the South American plate. It has been subdivided in several volcanic zones, namely the North (10°N–5°S), Central (5°S–33·5°S), Southern (33·5°S–46·5°S) and Austral (46·5°S–56°S) zones, separated by volcanic gaps (Fig. 1a inset) (Stern, 2004). In the Chilean Andes, the Southern Volcanic Zone (SVZ) stretches from 33·5° to 46·5°S, its northern and southern limits corresponding to subduction of, respectively, the Juan Fernández Ridge and the Chile Rise that separates the Nazca and Antarctic plates (Stern, 2004) (Fig. 1a). The SVZ has itself been subdivided into northern (NSVZ: 33°S–34·5°S), transitional (TSVZ: 34·5°S–37°S), central (CSVZ: 37°S–41·5°S) and southern (SSVZ: 41·5°S–46°S) zones by Lopez-Escobar & Moreno (1994) and Lopez-Escobar *et al.* (1995). Recently, Hickey-Vargas *et al.* (2016b) proposed to move the northern limit of the CSVZ from 37°S to 38°S, this new limit corresponding to the northern extremity of an important intra-arc, transpressional dextral strike-slip structure, the 1200 km-long Liquiñe–Ofqui fault

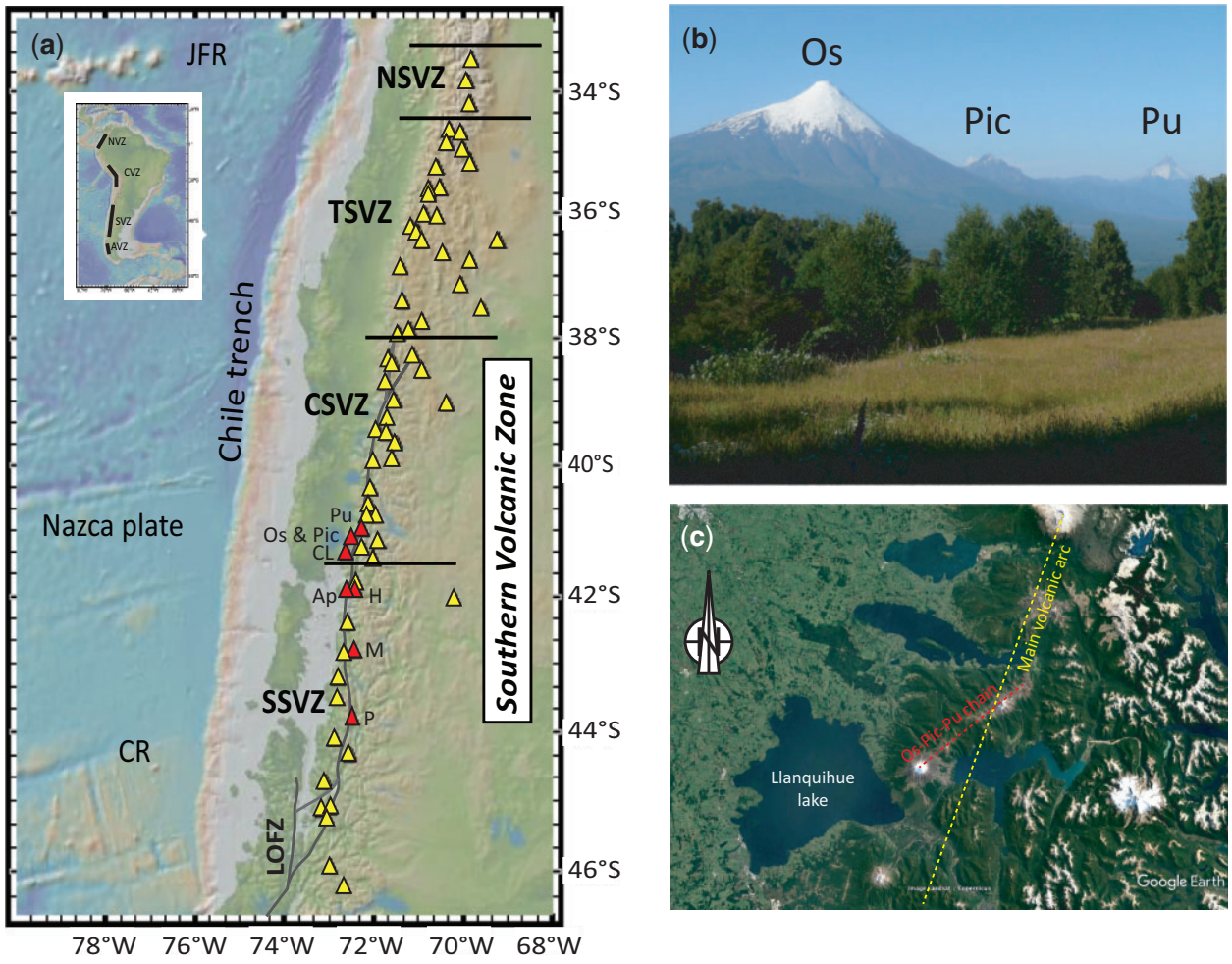

Fig. 1. Location of the La Picada volcano. (a) Global multi-resolution topography (GMRT) map of the Andean Southern Volcanic Zone (SVZ) showing the position of La Picada (Pic), merging with that of Osorno (Os), among the chain of active volcanoes. Also shown are the Palena (P), Minchinmavida (M), Apagado (Ap), Hornopiren (H), Calbuco (CL) and Puntiagudo–Cordon Cenizos (Pu) volcanoes. Cordon–Cenizos is a chain of scoria cones and stratovolcanoes extending to the NE of Puntiagudo. Volcanoes discussed in this study are shown with red trinagles, others with yellow triangles. NSVZ, TSVZ, CSVZ and SSVZ designate the different segments of the SVZ, respectively the Northern, Transitional, Central and Southern SVZ (after Lopez-Escobar *et al.*, 1995; Hickey-Vargas *et al.*, 2016b). LOFZ is the Liquiñe–Ofqui Fault Zone (after Cembrano & Lara, 2009). The Juan Fernandez Ridge (JFR) and Chile Rise (CR) are also indicated. The inset map shows subdivision of the Andean arc into North, Central, Southern and Austral Volcanic Zones (NVZ, CVZ, SVZ and AVZ, respectively). Maps constructed using GeoMapApp. (b) Photograph, taken to the northeast, showing the position of La Picada (Pic) close to the northern flank of Osorno (Os), with Puntiagudo (Pu) in the background. (c) Google Earth image displaying the Osorno–La Picada–Puntiagudo small chain oblique to the main volcanic arc and oriented at N45°E.

zone (LOFZ) extending from 38° to 47°S (Cembrano *et al.*, 1996), to which the SSVZ is related (Fig. 1a). At 38°S, the composition of the basement also changes from Meso-Cenozoic volcano-sedimentary rocks in the north to Meso-Cenozoic plutonic rocks of the Patagonian Batholith in the south (Cembrano & Lara, 2009). The convergence between the Nazca plate and South America is slightly oblique to the trench direction (~26° at 40°S; Jarrard, 1986) and occurs at a rate of 66 mm/y (Angermann *et al.*, 1999). At Osorno (41·1°S), the normal component of plate convergence rate is 72·1 mm/y (Syracuse & Abers, 2006). In the SVZ, the thickness of the continental crust under the arc, i.e. the depth of the Moho, varies from 50 km in the north to about 30 km in the south (Assumpção *et al.*, 2013; Hickey-Vargas *et al.*, 2016b), with a value of 32 km at a latitude of 39·5°S (Syracuse *et al.*, 2010). According to Syracuse & Abers (2006), at Osorno, the volcano–slab distance is 72 km, the volcano–trench distance perpendicular to the slab strike is 220 km and the average dip of the slab is 39°.

La Picada together with Osorno, Puntiagudo and Cordón Cenizos define a small chain that is oriented at N45°E, oblique to the main volcanic arc (Fig. 1a–c). Available K–Ar and Ar–Ar ages indicate that the history of this oblique chain started at about 500 ky ago, before the onset of Osorno at 300 ky, and lasted until 60 ky corresponding to the ultimate building phase of Osorno (Moreno *et al.*, 2010). La Picada is located about 6 km to the north-east of the Osorno volcano summit. It is older

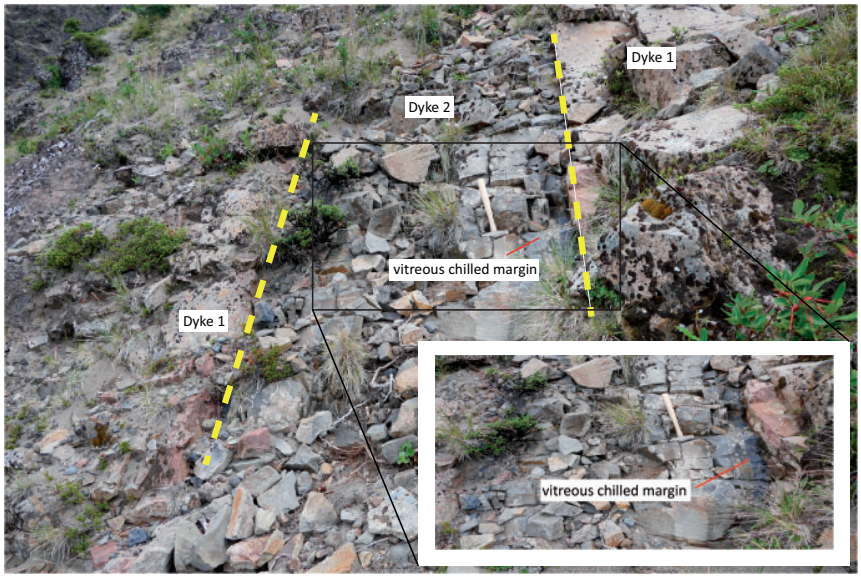

Fig. 2. Photograph of a composite dyke from the southern flank of La Picada (hammer for scale). The inner body (dyke 2) and outer portions (dyke 1) result from dyke-in-dyke intrusion.

than Osorno and thus recorded the early activity of the Osorno–Puntiagudo–Cordón Cenizos chain. It has not erupted in historical time, whereas Osorno last erupted in 1830. La Picada is now extinct, but its geochemistry and close proximity to Osorno indicate possible interaction of the plumbing systems of the two volcanoes during the early stages of Osorno (Moreno *et al.*, 2010; Biggs *et al.*, 2016). It has been deeply eroded by the Santa Maria and Llanquihue glaciations (58 000 to 14 200 y BP; Porter, 1981). The flanks of La Picada expose a series of intercalated 5–15 m thick units made of basaltic lavas and breccias, that are cut by numerous subvertical dykes (Moreno *et al.*, 2010). These dykes are well exposed on the southern flank of La Picada that faces Osorno. It will be shown that these dykes are mostly dacitic and were probably located below small dacitic domes, now eroded away, similar to the two domes that have been mapped on the southern and western flanks of Osorno (Moreno *et al.*, 2010). At least two generations of dykes have been observed on the southern flank as illustrated in Fig. 2, where an inner dyke, referred to as dyke 2, displays conspicuous chilled margins at the contact with an outer dyke, called dyke 1, indicating that dyke 2 was emplaced after dyke 1, within the same weakness zone (dyke-in-dyke intrusion). Dark black pyroclastic deposits are rather abundant in some parts of La Picada and were most probably emplaced during the last eruption of Osorno. They were thus not considered in this study. Blocks of gabbroic rocks are frequent and are interpreted as fragments from the plutonic basement.

SAMPLE COLLECTION

Samples were collected during three field seasons (2013, 2014, 2015) that focused on the La Picada, Osorno and Calbuco volcanoes. La Picada samples comprise 30 lavas, 13 samples from the dykes and 4 gabbroic fragments, hence a total of 47. Samples PIC39, 40, 47 and 48 were collected from dyke 2, whereas samples PIC38, 42 and 49 are from dyke 1. Sample PIC41 was collected just at the contact between the inner and outer dykes and was initially considered as part of dyke 1 but its trace elements content clearly indicate that it belongs to dyke 2 (see below). PIC51 and 52 were sampled from a non-composite dyke and grouped with dyke 1. Samples PIC05, 06, 30, 31, 34 and 35 are from homogeneous blocks within the breccias. The location of each sample (latitude, longitude) is reported in Table 1.

Crystal terminology

Detailed observations, geochemical data and quantification of crystal textures in volcanic rocks have revealed the occurrence of multiple crystal populations (e.g. Davidson *et al.*, 2007). This has prompted the use of several terms (phenocrysts, xenocrysts, antecrysts and microlites) that are genetic (e.g. Jerram & Martin, 2008). More particularly, the term phenocryst has evolved from a descriptive meaning, large crystals in a finer grained matrix, to a genetic one, as for many petrologists it designates a crystal in equilibrium with the magma (e.g. Jerram & Martin, 2008). Here, we will follow the terminology recently adopted by several authors (e.g. Neave *et al.*, 2014) and use the non-genetic terms macrocrysts and microlites to refer to crystals with a long axis length respectively larger and smaller than 150 microns. The prefix « macro » does not mean that the crystals are significantly large, as in the La Picada lavas macrocrysts have a maximum long axis of 2 mm.

Table 1: Major and trace element analyses of La Picada whole rocks

Sample #	PIC01	PIC02	PIC03	PIC04	PIC05	PIC06	PIC07	PIC08	PIC09	PIC10	PIC11	PIC12	PIC13	PIC14	PIC15
Type	Int MgO-	Int MgO-	Int MgO+	High MgO	High MgO	High MgO	Int MgO-/Dyke	Int MgO-/Dyke	Int MgO+	Int MgO+	Gabbro	Int MgO+	Int MgO+	Int MgO-	Int MgO-
X (WGS84-18G)	0712088	0712088	0712088	0714173	0714334	0714334	0713909	0713909	0713909	0713909	0713909	0714739	0714725	0715127	0715127
Y (WGS84-18G)	5449983	5449983	5449983	5450508	5450921	5450921	5450697	5450697	5450697	5450697	5450697	5450827	5450472	5451328	5451328
wt%															
SiO_2	53·72	53·34	53·96	51·61	50·63	50·38	53·57	53·18	52·18	52·74	52·36	55·85	53·60	52·56	52·52
TiO_2	0·84	0·82	0·82	0·87	0·83	0·83	0·95	0·96	0·87	0·94	0·64	0·94	0·94	0·90	0·89
Al_2O_3	19·29	18·94	18·84	17·46	17·25	17·18	18·42	18·77	18·11	18·68	18·37	19·09	18·36	18·49	18·52
Fe_2O_3	8·50	8·70	8·82	9·54	9·46	9·46	8·82	8·78	9·04	8·94	8·23	8·19	9·62	8·91	8·76
MnO	0·12	0·18	0·15	0·15	0·15	0·15	0·14	0·14	0·14	0·14	0·10	0·13	0·16	0·15	0·15
MgO	3·52	3·60	4·94	7·55	7·28	7·12	4·59	4·57	5·84	5·48	5·71	3·05	4·97	4·94	4·81
CaO	9·10	9·76	8·76	10·01	9·50	9·55	10·59	10·60	10·40	10·27	8·48	8·64	9·44	10·72	10·79
Na_2O	3·36	3·20	3·28	2·73	2·58	2·55	3·06	3·01	2·84	2·96	2·84	3·54	3·04	2·89	2·82
K_2O	0·48	0·48	0·52	0·47	0·50	0·50	0·50	0·48	0·41	0·44	0·61	0·84	0·50	0·64	0·68
P_2O_5	0·14	0·13	0·13	0·13	0·10	0·12	0·13	0·12	0·11	0·12	0·07	0·15	0·12	0·16	0·15
LOI	1·03	1·99	1·03	0·04	1·04	0·78	0·18	0·32	0·17	0·71	2·65	0·01	0·22	0·46	0·60
Total	100·11	101·16	101·24	100·55	99·33	98·61	100·96	100·92	100·12	101·42	100·05	100·43	100·96	100·82	100·70
Mg#	0·45	0·45	0·53	0·61	0·60	0·60	0·51	0·51	0·56	0·55	0·58	0·42	0·51	0·52	0·52
ppm															
Sc	26	29	25	34	33	34	33	28	33	33	34	27	32	31	31
V	215	224	200	240	235	233	277	229	230	252	230	206	231	236	238
Cr	47	59	49	203	203	201	64	57	125	115	121	11	40	47	41
Co	26	29	28	35	36	35	34	33	30	32	42	19	28	27	27
Ni	25	31	33	73	70	70	34	33	54	47	47	8	14	14	14
Zn	86	86	77	76	75	73	70	63	85	74	44	79	82	80	82
Ga	20	20	17	16	17	16	17	15	16	17	16	19	18	17	18
Rb	11	13	13	7.3	12	13	12	12	10	10	18	28	12	16	16
Sr	467	459	450	443	414	406	421	440	447	454	334	396	363	551	532
Y	18	18	18	18	15	17	20	22	18	20	15	22	22	22	21
Zr	66	63	65	59	60	64	65	67	60	66	64	87	75	79	77
Nb	2·3	2·2	2·2	1·8	1·8	1·7	1·7	1·9	1·8	2·1	2·3	3·4	2·8	2·7	2·7
Cs	0·71	0·85	0·42	0·20	0·79	0·83	0·91	0·91	0·64	0·85	0·43	0·69	0·81	0·91	0·59
Ba	161	170	159	142	146	145	147	154	145	159	227	229	170	224	224
La	5·7	5·5	5·6	5·5	3·6	5·5	5·2	6·5	5·6	5·8	10	8·6	7·4	11	11
Ce	14	13	14	14	11	13	14	14	13	14	15	20	16	24	24
Pr	2·3	2·2	2·3	2·2	1·7	2·0	2·3	2·4	2·2	2·4	2·2	3·1	2·5	3·3	3·3
Nd	10	10	10	10	7·7	9·0	10	11	10	11	9·0	13	11	14	14
Sm	2·6	2·5	2·6	2·7	2·3	2·5	2·8	2·9	2·6	2·9	2·1	3·3	2·9	3·4	3·3
Eu	0·94	0·90	0·93	0·93	0·81	0·89	0·99	1·0	0·95	1·0	0·78	1·1	0·98	1·1	1·1
Gd	3·0	2·8	2·8	2·9	2·4	2·7	3·1	3·4	2·8	3·2	2·1	3·5	3·2	3·4	3·3
Dy	3·0	2·9	3·0	3·0	2·7	2·9	3·2	3·5	3·0	3·3	2·4	3·8	3·6	3·4	3·4
Ho	0·60	0·58	0·60	0·62	0·54	0·60	0·68	0·73	0·62	0·69	0·51	0·77	0·75	0·73	0·71
Er	1·8	1·7	1·8	1·8	1·6	1·8	1·9	2·1	1·8	2·0	1·5	2·2	2·2	2·1	2·1
Yb	1·8	1·7	1·7	1·7	1·6	1·7	1·9	2·0	1·7	1·9	1·6	2·1	2·2	2·1	2·0
Lu	0·27	0·27	0·26	0·27	0·25	0·27	0·29	0·33	0·27	0·31	0·26	0·34	0·32	0·33	0·31
Hf	1·8	1·8	1·8	1·7	1·7	1·8	1·9	1·9	1·7	1·9	1·9	2·5	2·0	2·2	2·0
Ta	0·14	0·12	0·13	0·10	0·10	0·09	0·09	0·10	0·08	0·13	0·19	0·23	0·15	0·14	0·14
Pb	6·8	5·8	4·8	6·2	7·5	7·2	8·2	7·7	11	12	8·5	8·4	6·3	9·5	10
Th	0·90	0·83	0·92	1·0	1·2	1·2	0·97	0·97	0·95	1·1	2·4	2·4	1·6	5·7	5·7
U	0·30	0·24	0·26	0·31	0·33	0·34	0·29	0·31	0·30	0·34	0·61	0·65	0·40	1·2	1·2
(La/Yb)N	2·1	2·2	2·2	2·1	1·5	2·2	1·8	2·2	2·2	2·1	4·4	2·7	2·3	3·5	3·7
(Eu/Eu*)N	1·0	1·0	1·1	1·0	1·1	1·1	1·0	1·0	1·1	1·0	1·1	1·0	1·0	1·0	1·0

(continued)

Table 1: Continued

Sample #	PIC18	PIC19	PIC21	PIC24	PIC25	PIC28	PIC29	PIC30	PIC31	PIC32	PIC33	PIC34	PIC35	PIC36	PIC37
Type	Int MgO-	Int MgO-	Int MgO+	Low MgO	Gabbro	Gabbro	Gabbro	Low MgO	Low MgO	High MgO	High MgO	Int MgO+	Low MgO	Int MgO+	Low MgO
X (WGS84-18G)	0715978	0715978	0715957	0715427	0714670	0714283	0714283	0712490	0712490	0712108	0712108	0712108	0712089	0712089	0712434
Y (WGS84-18G)	5451799	5451799	5451763	5451444	5451021	5450935	5450935	5450146	5450146	5450107	5450107	5450107	5450000	5450000	5450149
wt%															
SiO_2	55·52	54·93	53·22	53·76	52·87	50·79	49·52	49·19	49·18	56·27	56·35	53·84	52·50	53·00	51·43
TiO_2	1·03	1·04	0·86	1·06	1·32	1·35	1·20	0·94	0·96	0·82	0·82	1·09	0·91	0·85	0·96
Al_2O_3	18·95	18·83	18·53	18·94	15·41	16·46	16·18	18·16	18·49	18·41	18·45	18·10	18·54	18·61	19·36
Fe_2O_3	8·37	8·25	8·66	8·49	9·41	10·55	10·08	9·66	9·82	7·78	7·66	8·84	9·71	8·83	9·30
MnO	0·14	0·14	0·15	0·15	0·19	0·20	0·17	0·16	0·16	0·12	0·13	0·14	0·17	0·13	0·15
MgO	2·65	2·64	5·07	2·72	4·45	5·49	6·16	6·14	6·38	4·02	4·09	3·95	4·07	4·75	5·07
CaO	8·86	8·96	10·51	8·98	8·79	11·08	9·00	11·01	10·94	7·50	7·48	8·77	10·15	8·86	9·97
Na_2O	3·69	3·67	2·87	3·65	3·58	2·51	2·58	2·37	2·46	3·85	3·84	3·37	2·89	3·29	3·03
K_2O	0·72	0·65	0·60	0·48	1·07	0·28	0·37	0·40	0·45	0·71	0·70	0·77	0·60	0·52	0·44
P_2O_5	0·19	0·18	0·14	0·17	0·23	0·06	0·21	0·13	0·13	0·17	0·17	0·24	0·14	0·15	0·15
LOI	0·84	0·95	0·42	1·00	2·11	1·25	4·47	1·97	1·51	0·43	0·36	0·68	0·85	1·14	0·43
Total	100·96	100·24	101·03	99·39	99·43	100·01	99·94	100·14	100·50	100·07	100·04	99·78	100·55	100·13	100·30
Mg#	0·38	0·39	0·54	0·39	0·48	0·51	0·55	0·56	0·56	0·51	0·51	0·47	0·45	0·52	0·52
ppm															
Sc	26	26	33	27	38	40	40	35	30	22	22	29	30	23	28
V	222	214	235	223	320	602	543	238	236	169	176	233	240	182	219
Cr	8·3	7·7	52	5·2	57	145	103	107	112	64	63	55	74	45	67
Co	19	18	26	21	26	27	21	34	33	24	24	24	30	27	28
Ni	6	6	18	7	29	47	42	45	45	37	37	22	19	31	29
Zn	83	85	76	87	82	58	53	74	70	74	71	74	122	67	71
Ga	20	19	18	19	18	16	15	17	17	17	17	17	16	16	16
Rb	20	17	18	9·3	34	4·3	13	10	10	20	20	19	14	12	11
Sr	387	396	464	385	332	343	312	449	436	447	448	396	396	413	432
Y	24	25	20	25	60	22	22	25	20	17	16	28	23	16	20
Zr	99	98	73	106	137	59	138	67	68	81	82	121	71	63	70
Nb	3·2	3·6	2·5	3·6	9·9	2·8	2·6	2·2	2·2	2·7	2·7	4·0	2·2	2·0	2·3
Cs	0·85	1·2	1·0	0·82	0·72	0·10	0·37	0·93	0·75	0·93	1·1	1·3	0·93	0·23	0·65
Ba	218	222	180	240	268	136	99	171	150	231	231	252	172	155	168
La	7·4	8·1	7·2	8·6	22	5·3	8·4	8·0	6·3	8·0	8·1	12	8·8	5·9	7·2
Ce	19	19	17	21	58	14	20	15	15	19	18	28	18	15	17
Pr	2·9	3·1	2·6	3·1	9·3	2·2	3·1	2·9	2·3	2·7	2·6	3·9	2·8	2·2	2·6
Nd	13	14	11	13	40	10	13	13	11	12	11	17	13	10	11
Sm	3·4	3·4	2·8	3·5	9·1	2·7	3·3	3·3	2·9	2·8	2·8	4·2	3·3	2·5	3·0
Eu	1·1	1·1	0·92	1·2	1·8	1·0	1·1	1·2	0·99	0·94	0·93	1·3	1·1	0·87	1·0
Gd	3·5	3·7	3·0	3·7	9·1	3·1	3·4	3·6	3·1	2·8	2·9	4·6	3·6	2·8	3·4
Dy	3·9	4·0	3·3	3·9	9·2	3·5	3·6	3·8	3·1	2·6	2·6	4·3	3·4	2·6	3·2
Ho	0·81	0·85	0·71	0·84	1·9	0·74	0·76	0·79	0·67	0·57	0·56	0·94	0·75	0·57	0·70
Er	2·4	2·6	2·0	2·5	5·6	2·2	2·2	2·3	1·9	1·5	1·5	2·7	2·1	1·6	1·9
Yb	2·3	2·4	2·0	2·5	5·3	2·2	2·0	2·1	1·9	1·6	1·6	2·7	2·1	1·6	2·0
Lu	0·38	0·37	0·31	0·38	0·81	0·35	0·33	0·35	0·29	0·25	0·24	0·40	0·32	0·25	0·30
Hf	2·7	2·7	2·1	2·8	4·2	1·7	3·7	1·9	1·9	2·1	2·1	3·1	1·9	1·7	1·8
Ta	0·19	0·23	0·17	0·20	0·43	0·18	0·18	0·11	0·11	0·12	0·13	0·21	0·10	0·08	0·09
Pb	6·9	8·9	7·5	6·1	5·8	6·9	5·5	6·7	7·0	5·1	4·8	5·4	5·6	3·2	4·0
Th	1·8	1·9	2·1	2·0	3·2	0·85	2·4	1·1	1·1	1·4	1·4	2·2	1·2	0·85	1·1
U	0·49	0·48	0·54	0·47	0·65	0·25	0·69	0·28	0·27	0·36	0·36	0·49	0·29	0·21	0·26
(La/Yb)N	2·2	2·2	2·4	2·3	2·8	1·6	2·8	2·5	2·2	3·3	3·3	2·9	2·8	2·4	2·4
(Eu/Eu*)N	1·0	1·0	1·0	1·0	0·6	1·1	1·0	1·0	1·0	1·0	1·0	0·9	0·9	1·0	1·0

(continued)

Table 1: Continued

Sample #	PIC38	PIC39	PIC40	PIC41	PIC42	PIC43	PIC44	PIC 47	PIC48	PIC49	PIC 50	PIC51	PIC52
Type	Dyke1	Dyke2	Dyke2	Dyke2	Dyke1	Int MgO+	Int MgO+	Dyke2	Dyke2	Dyke1	High MgO/Dyke	Dyke1	Dyke1
X (WGS84-18G)	0712427	0712427	0712427	0712427	0712427	0712427	0714222	0712436	0712436	0712436	0712422	0712368	0712368
Y (WGS84-18G)	5450157	5450157	5450157	5450157	5450157	5450157	5449276	5450147	5450147	5450147	5450167	5450162	5450162
wt%													
SiO_2	60·31	64·46	63·64	64·67	60·86	49·92	55·69	64·66	64·61	61·49	50·06	63·91	64·44
TiO_2	0·80	1·00	1·02	1·00	0·79	0·94	0·97	0·97	0·95	0·75	0·82	0·81	0·80
Al_2O_3	16·52	15·09	15·48	15·10	16·56	17·67	19·02	15·54	15·28	16·82	17·61	16·32	16·16
Fe_2O_3	6·94	6·25	6·29	6·20	7·00	9·75	8·14	6·05	6·07	6·76	9·37	5·97	6·11
MnO	0·13	0·11	0·11	0·11	0·10	0·15	0·13	0·10	0·11	0·10	0·15	0·14	0·13
MgO	1·52	1·30	1·30	1·27	1·18	6·47	2·86	1·24	1·30	1·57	7·49	1·30	1·38
CaO	4·70	3·99	4·01	3·99	4·75	10·09	8·45	4·11	4·09	5·27	10·85	4·36	4·47
Na_2O	4·51	4·36	4·23	4·29	4·47	2·75	3·57	4·38	4·24	4·77	2·48	5·35	5·33
K_2O	0·92	2·23	2·27	2·23	0·93	0·44	0·84	2·24	2·40	0·90	0·29	1·23	1·25
P_2O_5	0·25	0·29	0·30	0·30	0·25	0·17	0·17	0·30	0·29	0·25	0·10	0·27	0·26
LOI	2·47	1·10	1·68	1·04	3·00	1·42	0·00	1·09	1·22	1·65	0·74	0·68	0·22
Total	99·06	100·18	100·33	100·20	99·90	99·77	99·84	100·69	100·56	100·34	99·96	100·35	100·54
Mg#	0·30	0·29	0·29	0·29	0·25	0·57	0·41	0·29	0·30	0·32	0·61	0·30	0·31
ppm													
Sc	19	20	20	21	20	32	26	21	18	19	29	20	21
V	88	72	72	72	95	251	203	73	63	93	220	52	51
Cr	<0·2	5	1	0·7	8	143	17	5	<0·2	2	232	0·8	0·8
Co	11	11	11	11	12	37	19	11	9	11	37	8	9
Ni	4	6	3	4	9	69	9	4	2	5	99	2	1
Zn	94	75	75	79	92	87	69	73	69	96	60	84	82
Ga	18	17	17	17	18	16	18	17	16	18	14	18	18
Rb	23	81	81	80	28	9	27	81	84	22	6	31	38
Sr	362	248	258	257	365	436	377	254	253	379	398	353	351
Y	29	43	47	51	27	20	23	45	46	35	20	34	31
Zr	127	258	272	269	128	71	89	261	262	129	53	149	146
Nb	4·1	6·9	7·2	7·0	4·0	2·3	3·2	6·8	6·8	4·0	1·4	4·2	4·8
Cs	0·61	5·0	5·1	4·6	1·3	0·39	0·59	5·0	5·4	1·4	0·46	1·5	3·0
Ba	317	538	570	551	334	186	223	547	546	323	110	384	380
La	14	23	24	26	14	8·7	10	24	25	16	6·5	16	12
Ce	31	52	56	57	29	20	21	54	57	35	13	33	33
Pr	4·7	7·0	7·5	8·3	4·6	2·9	3·1	7·4	7·7	5·1	2·2	4·9	4·7
Nd	20	29	31	34	19	13	13	31	32	22	10	21	20
Sm	4·9	6·8	7·3	8·0	4·7	3·1	3·3	7·3	7·5	5·1	2·7	5·0	4·8
Eu	1·3	1·5	1·6	1·6	1·3	1·1	1·1	1·5	1·5	1·4	0·94	1·4	1·3
Gd	4·9	7·0	7·5	8·1	4·6	3·4	3·7	7·4	7·8	5·4	3·1	5·0	4·9
Dy	4·6	6·6	7·0	7·5	4·2	3·1	3·5	6·9	7·3	5·0	2·9	4·8	4·6
Ho	0·97	1·4	1·5	1·6	0·90	0·67	0·77	1·5	1·5	1·1	0·64	1·1	0·98
Er	2·7	4·0	4·2	4·6	2·5	1·8	2·1	4·2	4·4	3·1	1·8	3·0	2·9
Yb	3·0	4·2	4·6	4·8	2·8	1·9	2·2	4·5	4·6	3·4	1·8	3·1	3·0
Lu	0·44	0·63	0·68	0·71	0·44	0·29	0·33	0·69	0·69	0·53	0·27	0·49	0·47
Hf	3·3	6·6	6·9	6·9	3·2	1·8	2·3	6·9	7·0	3·3	1·4	3·9	3·9
Ta	0·20	0·42	0·45	0·44	0·20	0·08	0·18	0·42	0·42	0·19	0·04	0·22	0·32
Pb	7·5	16	16	16	8·0	3·0	4·4	16	15	8·0	2·7	10	12
Th	2·0	6·7	7·1	6·9	1·9	1·3	2·3	6·8	6·9	2·0	0·72	3·1	3·1
U	0·56	1·7	1·8	1·8	0·49	0·31	0·56	1·8	1·8	0·50	0·20	0·84	0·82
(La/Yb)N	3·2	3·6	3·6	3·7	3·3	3·1	3·1	3·5	3·6	3·1	2·4	3·3	2·8
(Eu/Eu*)N	0·8	0·7	0·7	0·6	0·9	1·0	0·9	0·6	0·6	0·8	1·0	0·8	0·9

Table 2: Ar–Ar dating results and irradiation parameters

	Sample	PIC04	PIC06	PIC07	PIC09
	Material	WR	WR	WR	WR
	Steps	1–4(4)	1–5(5)	2–6(5)	1–4(4)
	Irradiation parameter	6·09E-05	6·00E-05	5·96E-05	5·96E-05
Spectrum	$\%^{39}Ar$	100	100	75·74	100
	Age ± 1.96σ	304 ± 95	250·3 ± 60·9	451·8 ± 25·4	478·1 ± 92·3
	MSWD (P)	2·7712(0·0400)	0·8495(0·4935)	6·8854(0·0000)	9·6533(0·0000)
	TGA ± 1.96σ	344·2 ± 125·3	236·3 ± 92·3	671·4 ± 80·4	428·5 ± 104·2
	K/Ca ± 1.96σ	0·1586 ± 0·0021	0·0863 ± 0·0009	0·1803 ± 0·0012	0·1084 ± 0·0012
Inverse Isochron	Age ± 1.96σ	236 ± 101	221·7 ± 70	361·1 ± 45·1	557·9 ± 127·9
	MSWD (P)	1·9200(0·0000)	0·5087(0·0000)	1·7997(0·0000)	14·2602(0·0000)
	Trapped $^{40}Ar/^{36}Ar$	301·7313 ± 2·9248	299·6557 ± 1·4724	306·2943 ± 3·2306	296·3933 ± 3·9705
	Spread (%)	17·6	15·6	9·2	5·4
Normal Isochron	Age ± 1.96σ	**218 ± 60**	**220 ± 36·2**	**360 ± 23·264**	**546 ± 87·9**
	MSWD (P)	2·124 (0·0)	0·519 (0·669)	1·722 (0·160)	14·28 (0·0)
	Trapped $^{40}Ar/^{36}Ar$	301·925 ± 2·96	299·670 ± 1·47	306·287 ± 3·23	296·304 ± 4·00

	Sample	PIC11_1	PIC11_3	PIC12
	Material	Plag	Plag	WR
	Steps	4–5(2)	1–15(15)	3–9(5)
	Irradiation parameter	6·14E-05	6·14E-05	6·24E-05
Spectrum	$\%^{39}Ar$	46·63	100	35·43
	Age ± 1.96σ	13·98 ± 0·179	25·477 ± 0·14	166·1 ± 27·6
	MSWD (P)	84·583 (–)	2181·7907(0·0000)	2·4144(0·0466)
	TGA ± 1.96σ	34·398 ± 0·257	45·063 ± 0·247	206·9 ± 20·1
	K/Ca ± 1.96σ	0·3427 ± 0·0032	0·1606 ± 0·0010	0·4058 ± 0·0036
Inverse Isochron	Age ± 1.96σ	**9·551 ± 0·885**	11·97 ± 0·126	158 ± 27·8
	MSWD (P)	–	1545·0935(0·0000)	1·9278(0·0000)
	Trapped $^{40}Ar/^{36}Ar$	320·9270 ± 4·3654	374·7601 ± 0·7379	300·0685 ± 1·4224
	Spread (%)	4·6	26·6	26·3
Normal Isochron	Age ± 1.96σ	9·551 ± 0·452	8·348 ± 0·108	**152 ± 14·4**
	MSWD (P)	–	1296·773 (0·0)	1·87 (0·132)
	Trapped $^{40}Ar/^{36}Ar$	320·927 ± 4·37	372·874 ± 0·72	300·127 ± 1·42

Steps, number of steps releasing sufficient gas to define a plateau in the incremental step-heating method with n as number of steps used to fit the isochron. $\%^{39}Ar$, percentage of the total ^{39}Ar released during the incremental step-heating method. Age, expressed in ky except for PIC11 (Ma). 1·96σ, 95% confidence level. MSWD, mean square weighted deviation. P, probability of fit. TGA, total gas age, in ky except for PIC11 (Ma). Spread, deviation from the fitted isochron. Bold font, best estimated accepted age. Corrections factors for Ca and K interferences are reported:
- $(^{39}Ar/^{37}Ar)Ca = (6·1062 \pm 0·1859) * 10–4$.
- $(^{36}Ar/^{37}Ar)Ca = (2·619 \pm 0·14) * 10–4$.
- $(^{40}Ar/^{39}Ar)K = (5·065746 \pm 3·509317) * 10–2$.

ANALYTICAL METHODS

Ar–Ar ages

Six samples were dated using the Ar–Ar method to complement existing data (Moreno *et al.*, 2010): basalts PIC04 and PIC06 and basaltic andesites PIC07, PIC09, PIC11 and PIC12. Fragments of the bulk-rocks were crushed and the coarse grain fraction (0·5–1 mm) was retained while finer fractions were discarded. The groundmass was separated from macrocrysts (e.g. altered grains, glass, olivine and pyroxene macrocrysts) under a binocular microscope and washed in a solution of 5% HNO_3 to remove alteration products before repeated rinses with de-ionized water to remove traces of HNO_3. Approximately 500 mg of clean matrix was wrapped in aluminium foil and irradiated in the nuclear reactor at the Institutt for the Energiteknikk (Kjeller, Norway) for 4 hours with an integrated flux of $1·32x10^{13}$ neutrons/cm^2.s. The sanidine from Alder Creek (ACS) having an age of 1·206 ± 0·002 Ma (Renne *et al.*, 2010) was selected as a monitor mineral to constrain and interpolate the irradiation parameters essential in the radiometric dating equation. For irradiation each sample was bracketed by two aliquots of the monitor mineral. Samples and standards were loaded in an aluminium holder and placed in an ultrahigh vacuum extraction line. Samples and standards were degassed incrementally using a CO_2 laser probe (λ = 10600 nm) and the gas analysed isotopically using a MAP215-50 noble gas mass spectrometer (Geological Survey of Norway (NGU), Trondheim). Due to the anticipated young age and potassium-poor nature of the samples, cautious monitoring of the mass discrimination of the mass spectrometer (via calibration air shots measurement prior to each sample) and volume reduction of the extraction line system were carried out in order to measure the small volume of radiogenic Ar. Corrections for irradiation induced excess Ar from calcium and potassium interferences were applied. Correction factors, irradiation parameters, number of incremental heating steps and age results are shown in Table 2.

Table 3: Raw point counting data and mass fractions for samples of La Picada

		Raw counts							Mass fractions (%)						
Type	Sample#	gm	plg	ol	cpx	opx	mgt	ves	gm	plg	ol	cpx	opx	mgt	macro
High MgO	PIC50*	1216	301	81	19		1	10	74·2	18·3	6·0	1·4	0·0	0·1	25·8
High MgO	PIC06	658	194	58				566	71·3	21·0	7·7	0·0	0·0	0·0	28·7
High MgO	PIC33*	930	456	5		148	2		59·2	29·0	0·4	0·0	11·2	0·2	40·8
Low MgO	PIC37	814	543	53	10			115	56·8	37·9	4·5	0·8	0·0	0·0	43·2
Low MgO	PIC24*	1021	195	4	4			340	83·3	15·9	0·4	0·4	0·0	0·0	16·7
Low MgO	PIC31*	599	560	76	26			308	46·7	43·7	7·2	2·4	0·0	0·0	53·3
Low MgO	PIC35	994	537	48	5			9	62·3	33·7	3·7	0·4	0·0	0·0	37·7
Int MgO	PIC12	1111	354	5	1	37			73·3	23·3	0·4	0·1	2·9	0·0	26·7
Int MgO	PIC09*	1121	421	49	1	1		19	69·9	26·2	3·7	0·1	0·1	0·0	30·1
Int MgO	PIC03	938	445	23	10	35		63	64·1	30·4	1·9	0·8	2·8	0·0	35·9
Int MgO	PIC34*	950	454	10	14	6		122	66·0	31·5	0·8	1·2	0·5	0·0	34·0

gm, groundmass ; plg, plagioclase ; ol, olivine ; cpx, clinopyroxene ; opx, orthopyroxene ; mgt, Ti-magnetite ; ves, vesicle ; macro, macrocryst.
*Samples counted three times.

Mineral chemistry

The major element composition of minerals and glasses in the La Picada samples was measured with a CAMECA SX100 electron microprobe at the University of Hannover, using an accelerating voltage of 15 kV. Mineral analyses were performed with a focused beam (1 μm) and a beam current of 5 nA. Each element was measured for 15–20 s. For the glass analyses, the beam current was set at 8 nA and the beam was defocused to 5 μm. The following standards were used: albite for Na, orthoclase for K, wollastonite for Si and Ca, TiO_2 for Ti, Fe_2O_3 for Fe, MgO for Mg, and Mn_3O_4 for Mn. Raw data were corrected with the CATZAF program. In order to detect the possible occurrence of different crystal populations, profiles across grains or from rims to cores were realized in olivine (873 analyses: Supplementary Data Table S1; supplementary data are available for downloading at http://www.petrology.oxfordjournals.org), plagioclase (2904 analyses: Supplementary Data Table S2), orthopyroxene (258 analyses: Supplementary Data Table S3) and clinopyroxenes (607 analyses: Supplementary Data Table S3) in a series of samples (PIC01, 02, 03, 04, 06, 07, 08, 10, 12, 19, 24, 30, 31, 33, 34, 35, 36, 37, 41, 43, 44, 48, 50) representative of the different facies of the volcano. Titanomagnetite was also analysed in 10 samples (PIC02, 12, 14, 15, 24, 32, 33, 38, 48, 50: Supplementary Data Table S4), together with ilmenite (PIC02, 03, 12, 15, 24, 32: Supplementary Data Table S4) that occurs as small exolution lamellae in Ti-magnetite, whereas chromite inclusions were analysed in the olivine of sample PIC50. Glass composition (Supplementary Data Table S5) was measured in a few basalts (PIC31, 50), basaltic andesites (PIC07, 10, 14) and dacites (PIC39, 41). In the basalts and basaltic andesites, glass occurs in very small interstitial pockets that locally contain microlites of Fe–Ti oxides and possibly plagioclase. Contrarily, the dacites are poor in macrocrysts enabling analyses of microlite-free glass.

Whole-rock chemistry

Forty-seven samples were crushed with a hammer and then ground in agate mortar with a Fritsch pulverisette planetary mill. Major elements were measured by X-ray fluorescence at the University of Liège. An ARL 9400 XP spectrometer was used for samples PIC01 to PIC13 and a Thermofisher PERFORM'X for the rest of the samples. Both spectrometers were equipped with a Rh tube. The major elements were measured on fused glass discs that were prepared with 0·35 g of rock powder, previously dried at 1000°C for two hours in the oven, and lithium- and tetra-borate. Calibration curves were calculated by measuring a series of 47–66 international standards that are mostly rock samples (basalts to granites, syenites, ultramafic rocks, sedimentary rocks) but also include a few minerals and two soils. Repeated analyses of external standards, not included in the calibration curves, indicate that the accuracy is better than ±3·5% for all major elements, except for TiO_2 (±4·9%), Na_2O (±12·4%) and P_2O_5 (±10·3%). The 1σ analytical precision is better than 1% for all major elements, except for Na_2O (±1·3%) and P_2O_5 (±3·2%). A Thermo Scientific X-Series 2 ICP-MS (MRAC Tervuren, Belgium) equipped with a collision cell was used to analyse trace elements in samples that were put into solution by alkali fusion. Calibration was performed with international standards prepared in the same way as the rock samples, as well as with standard solutions prepared with element solutions. Accuracy and precision were estimated by repeated analyses of 12 standards and range between 2·0 and 5·7% and between 1·5 and 5·2%, respectively (one sigma) (Navez, 1995). Results are shown in Table 1.

Point counting

The proportions of macrocrysts, vesicles and matrix were determined by point counting with a PELCON Automatic Point Counter for 12 samples ranging from basalt to basaltic andesite. Steps of 0·5 mm were used along the x- and y-axes, giving about 1500 points per sample. Vesicles, macrocrysts of plagioclase, olivine, orthopyroxene, clinopyroxene and Ti-magnetite were counted. Crystals smaller than 100 microns were considered as groundmass. The mass proportions of

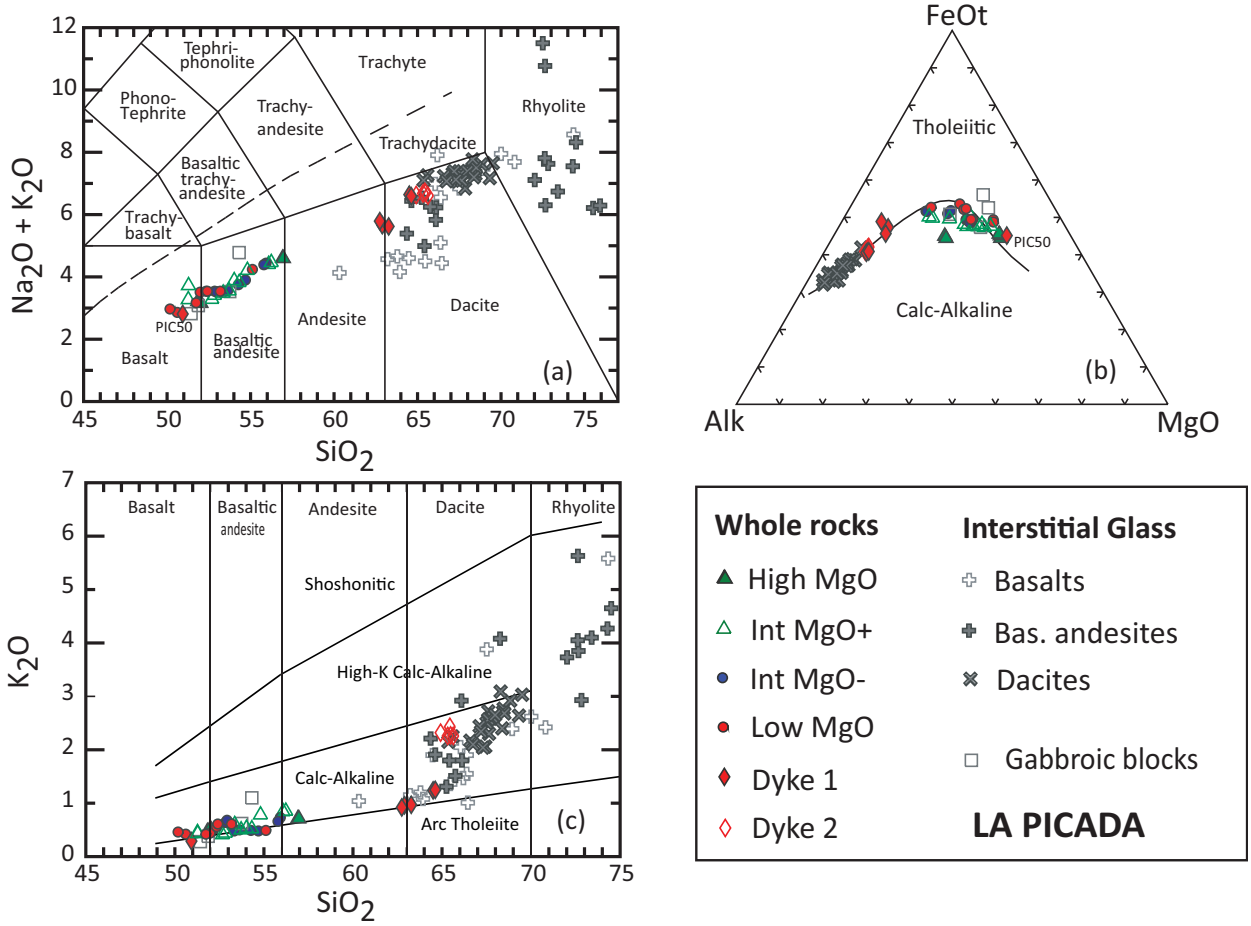

Fig. 3. Geochemical classification diagrams. (a) TAS diagram (dashed line is the limit of Irvine & Baragar (1971) between alkaline and subalkaline fields). (b) AFM diagram with the limit of Irvine & Baragar (1971) between tholeiitic and calc-alkaline fields. (c) K_2O vs SiO_2 diagram (limits between fields from Peccerillo & Taylor (1976)). See Major Elements section for the definition of High-, Low-, Int-MgO. Analyses recalculated to 100% on a volatile free basis with total Fe as FeO_t.

crystals on a vesicle-free basis were obtained by considering the following densities: 2·7 g/cm^3 for plagioclase and groundmass, 3·3 g/cm^3 for olivine, 3·2 g/cm^3 for pyroxenes and 5·0 g/cm^3 for Ti-magnetite. Variation of density due to the compositional evolution of the solid solutions influences the calculated mass proportions, but the error on the reproducibility of the point counting is much higher (Table 3) and constant densities have thus been considered. The proportion of macrocrysts ranges from 28·7% to 54·4%. Plagioclase displays the highest proportion within the macrocrysts, from 68% to 99%.

PETROGRAPHY, MINERAL CHEMISTRY AND PHASE PROPORTIONS

La Picada samples range from basalts (PIC04, 5, 6, 30, 31, 37, 43, 50) to dacites (38, 39, 40, 41, 42, 47, 48, 49, 51, 52), basaltic andesites being dominant (PIC01, 2, 3, 7, 8, 9, 10, 12, 13, 14, 15, 18, 19, 21, 24, 32, 33, 34, 35, 36, 44) and andesites conspicuously absent (see TAS diagram in Fig. 3). The dacites were all collected from dykes crosscutting the southern flank. The textures are mostly microlitic porphyric, hyalopilitic or trachytic. All samples contain macrocrysts of plagioclase except PIC04 in which olivine is the sole macrocryst (Fig. 4a).

Basalts and basaltic andesites

Basalts and basaltic andesites are variably vesicular (up to 40%) and display changing proportions (18–54 vol. %) of plagioclase, olivine and pyroxene macrocrysts dispersed in a groundmass that is usually microcrystalline. Glomerocrysts are nearly ubiquitous and are dominated by plagioclase grains showing either a shape-preferred or a random orientation. Plagioclase, up to 2 mm long and 600 μm large, ranges in composition from An_{92} (basalts)/An_{93} (basaltic andesites) in the cores to An_{39} (basalts)/An_{28} (basaltic andesites) in the rims. Compositional histograms display corresponding peaks at about An_{85} (basalts)/$An_{82–90}$ (basaltic andesites) and An_{65} (basalts)/An_{60} (basaltic andesites) (Fig. 5a). Typical core-rim compositional profiles display a core surrounded by a zone of decreasing anorthite content followed by a rim that usually has a constant

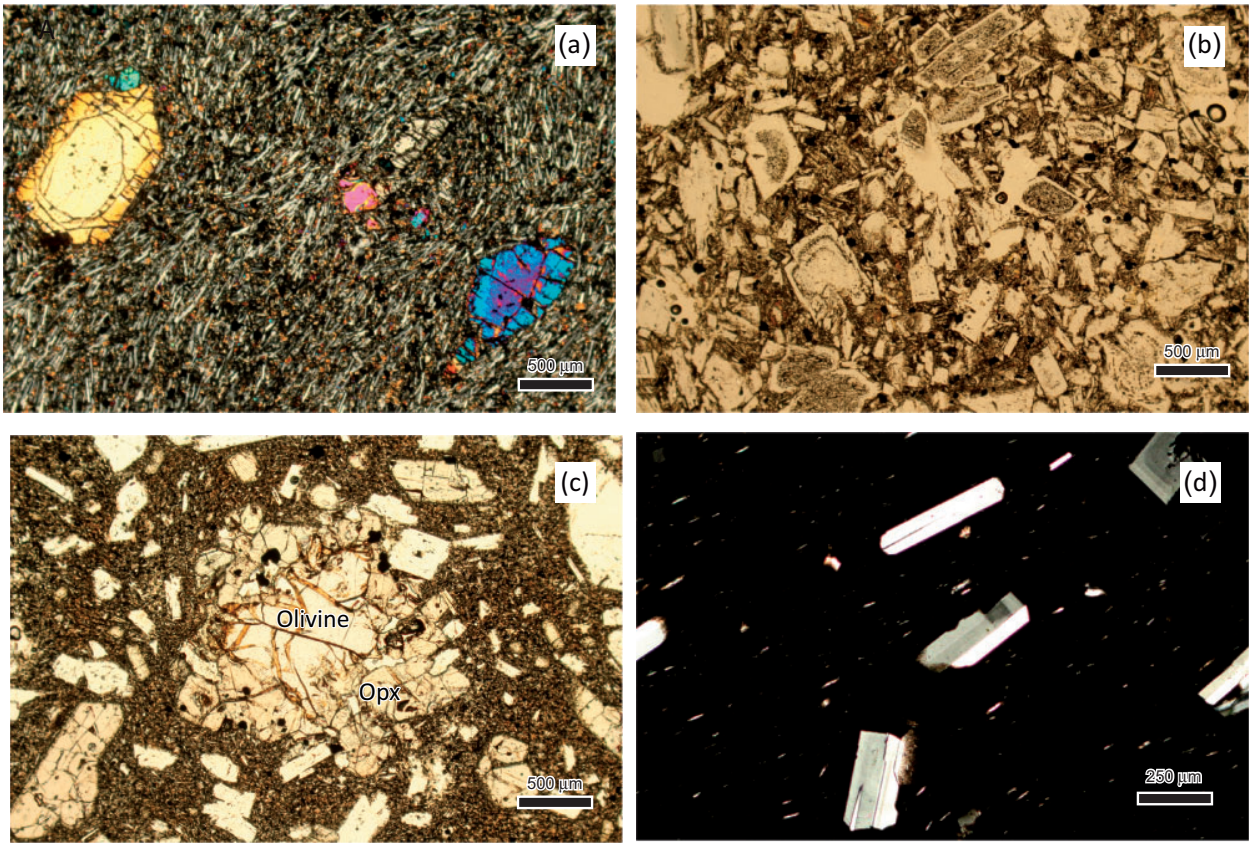

Fig. 4. Photomicrographs of selected samples, taken in transmitted light. (a) Olivine macrocrysts in basalt PIC04 (crossed nicols). (b) Zoned plagioclase macrocrysts in basaltic andesite PIC13 (note the abundance of inclusions) (parallel nicols). (c) Orthopyroxene corona around olivine macrocryst in basaltic andesite PIC33 (parallel nicols). (d) Sparse population of plagioclase macrocrysts in the PIC52 dacite (note the low abundance of inclusions, the slight zoning and the shape-preferred orientation) (crossed nicols).

composition (Fig. 6). Plagioclase shows a large range of textures depending on the amount and location of inclusions in the grains (Fig. 4b). Partly to totally recrystallized melt inclusions may be present throughout the crystal or concentrated in concentric zones or in the core. The mineralogy of the ferromagnesian macrocrysts varies with the whole-rock composition. In the basalts (up to 52·50% SiO_2, PIC 35), olivine ($Fo_{86–65}$, Fig. 5a), up to 2 mm-long and 1·5 mm-large, is the dominant ferromagnesian mineral and is accompanied by some augite (Mg# = 71·6–57·7: Fig. 5a, b), up to 700-μm long and 400-μm large. Augite is locally surrounded by pigeonite that also occurs in the groundmass. Olivine is usually idiomorphic and contains small inclusions of dark brown chromite in several basaltic samples (PIC04, 06, 50). Titanomagnetite has not been observed as a macrocryst in the basalts, but is abundant as microlites ($Uvsp_{63}$). In the basaltic andesites (from 52·52% to 56·35% SiO_2), olivine ($Fo_{80–51}$: Fig. 5a) is accompanied by orthopyroxene (Mg# = 74·2–59·2: Fig. 5a, b) and augite (Mg# = 82·8–64·7: Fig. 5a, b). Here too, augite is locally surrounded by pigeonite also occurring as microlites in the groundmass. Olivine usually occurs as isolated grains displaying varying transformation into iddingsite that grew preferentially from the rim of the grains and along microfractures. A thin rim of opaque grains surrounding olivine is nearly ubiquitous. Orthopyroxene and clinopyroxene also occur as idiomorphic grains. Locally orthopyroxene is surrounded by a rim of pigeonite. In about half of the basaltic andesites, titanomagnetite, locally displaying exsolution lamellae of ilmenite, occurs as microlites ranging from 50 to 100 μm. In several glomerocrysts, crystals of olivine are surrounded by coronae of orthopyroxene grains, suggestive of a peritectic reaction between olivine and the liquid (Fig. 4c).

Contrary to basalts and basaltic andesites, dacites display few plagioclase, pyroxene and titanomagnetite macrocrysts dispersed in a crypto- to microcrystalline groundmass in which some microlites of plagioclase usually define a trachytic texture (Fig. 4d). Plagioclase (An_{46} to An_{68}) has usually a high aspect ratio, up to 1·5 mm-long and 500-μm large, but more equant grains are locally observed. In striking contrast with what is seen in the basalts and basaltic andesites, plagioclase has few to no inclusions and displays less complex zoning patterns (Fig. 4d). Olivine is absent, whereas idiomorphic orthopyroxene (Mg# = 63·0: Fig. 5a, b), up to 1 mm-long and 250-μm large, together with augite (Mg# = 72·2–60·3; Fig. 5a, b), up to 500-μm long and 250-μm large, occur in nearly equal abundances. Augite is frequently twinned and equant grains of titanomagnetite are larger, about 125 μm, than in the basaltic andesites.

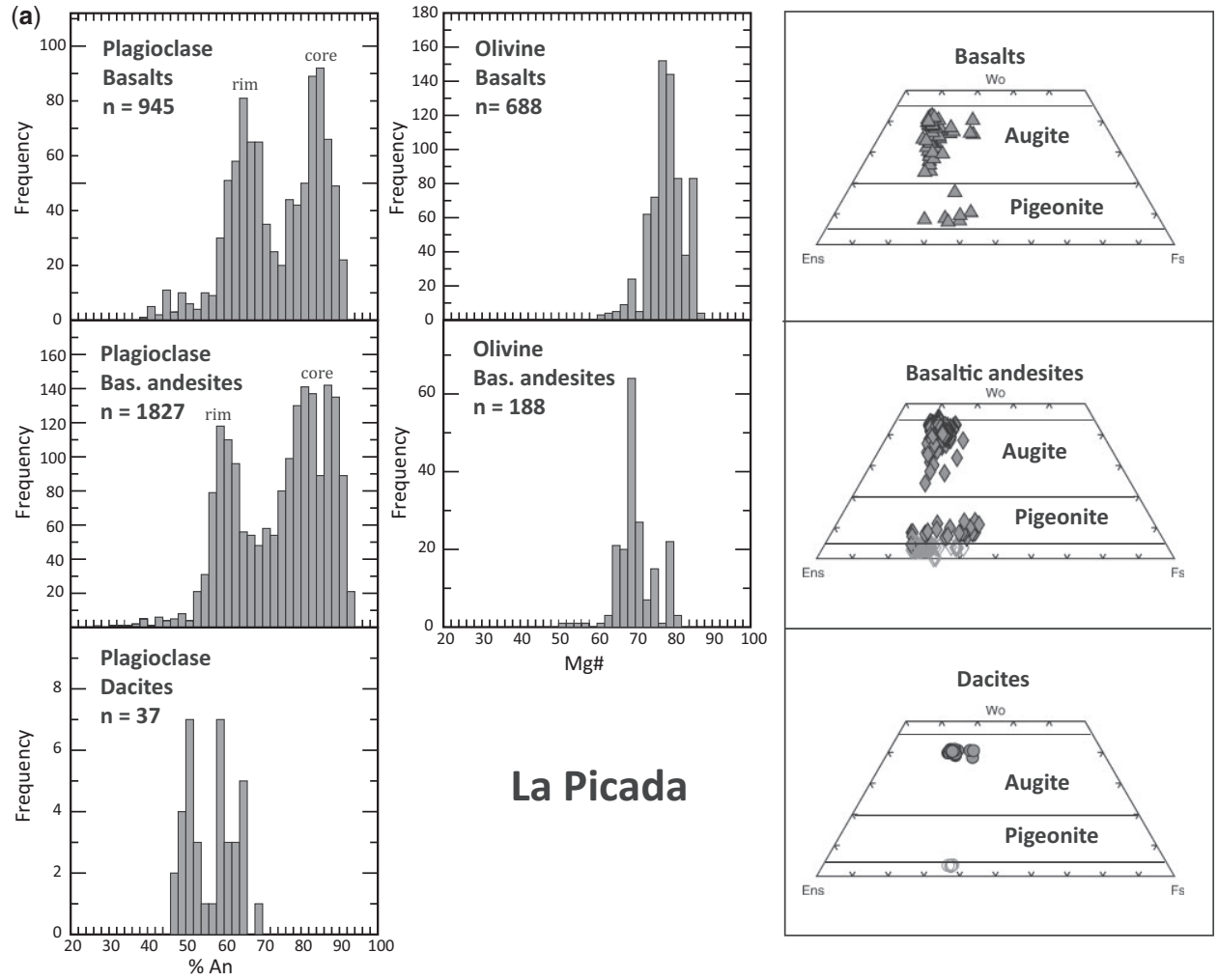

Fig. 5. (a) Summary of macrocryst compositions in the basalts, basaltic andesites and dacites determined by electron probe microanalysis. %An = Ca*100/(Ca+Na) in moles of cations, Mg# = 100*Mg/(Fe+Mg) in moles of cations and Fe is total Fe, n is number of analyses. (b) Pyroxene Mg# in the basalts, basaltic andesites and dacites. Mean is the average Mg# for the number n of analyses.

Amphibole is lacking in the whole series of La Picada samples. The petrographic observations suggest that olivine appears first on the liquidus, either together with plagioclase or shortly followed by it. After some differentiation, clinopyroxene crystallizes and olivine reacts to form orthopyroxene. Titanomagnetite is a late phase.

Rhodes diagrams (Fig. 7) show that the cores of olivine in the basalts and basaltic andesites (K_D^{Fe-Mg} = 0·30 ± 0·03; Roeder & Emslie, 1970) and of augite in the basaltic andesites (K_D^{Fe-Mg} = 0·27 ± 0·03 : Putirka, 2008) are in equilibrium with the whole rock. The K_D^{Fe-Mg} proposed by Putirka (2008) for clinopyroxene-melt equilibria is appropriate here as experimental data performed on starting compositions similar to the parent magmas of La Picada and with variable H_2O contents (0 to 8·98 wt %; Draper & Johnston, 1992; Blatter *et al.*, 2013; Andújar *et al.*, 2015) give an average K_D^{Fe-Mg} = 0·26 ± 0·04. In the dacites, the clinopyroxene macrocrysts are scarce and of small size (up to 500 μm). Available data indicate that their Mg# (0·68 to 0·72) is generally too high to be in equilibrium with the WR (Mg# = 0·.60), but is appropriate for clinopyroxenes in equilibrium with the most evolved basaltic andesite (Fig. 7). However, three analyses performed on the rims of clinopyroxenes from sample PIC48 have a lower Mg # (0·60 to 0·62) that is in equilibrium with the whole rock (Fig. 5b, Supplementary Data Table S3). An equilibrium test was not performed for plagioclase because the composition of this mineral depends on several parameters (magma composition, temperature, pressure and H_2O content; e.g. Waters & Lange, 2015). We however note An rich plagioclase cores (An_{93}) in the basaltic andesites, suggesting equilibrium with the whole-rock (see thermobarometry section below). Moreover, plagioclase rims from the basaltic andesites have overlapping compositions with plagioclase from the dacites (Fig. 5a). As will be shown below, the dacitic composition (dyke 1) can be produced by fractional crystallization from the basalts and basaltic andesites and we interpret the normal zoning of the plagioclase as

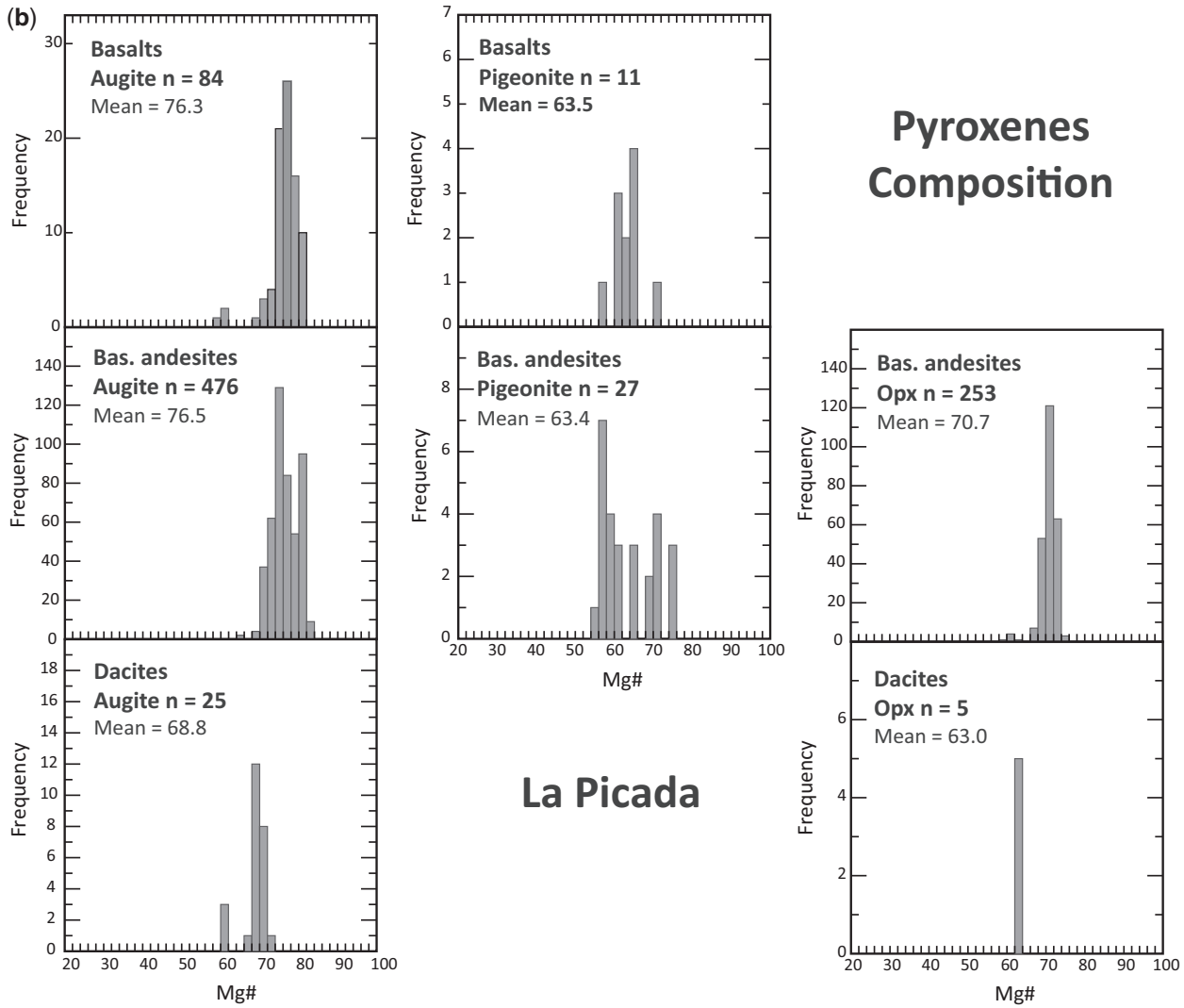

Fig. 5. Continued.

resulting from differentiation of the interstitial melt in a crystal mush, the plagioclase rims being in equilibrium with a more evolved composition than the bulk-rock. Analogy can be made here with what is observed in layered intrusions such as the Skaergaard (e.g. Namur *et al.*, 2014). Mineral data thus suggest that the basalts and basaltic andesites mainly entrained their own crystals, whereas in the dacites, the clinopyroxene may have been captured from a crystal mush and the small plagioclase crystals probably crystallized from the dacitic melt during the ascent.

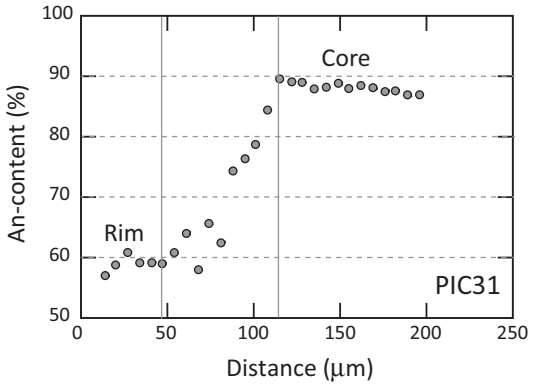

Fig. 6. Plagioclase grain from PIC31 showing a typical compositional profile from core to rim. %An = Ca*100/(Ca+Na) in moles of cations.

RESULTS

Whole-rock and glass chemistry

Rock classification

As already noted, whole-rock samples range from basalts to dacites with dominant basaltic andesites (Fig. 3a). The conspicuous absence of andesites results in a compositional (Daly) gap between 56·96 wt % SiO_2 (PIC33) and 62·74 wt % SiO_2 (PIC49), in striking contrast with what is observed in the Central Andes where lavas of andesitic composition are dominant (Wörner *et al.*,

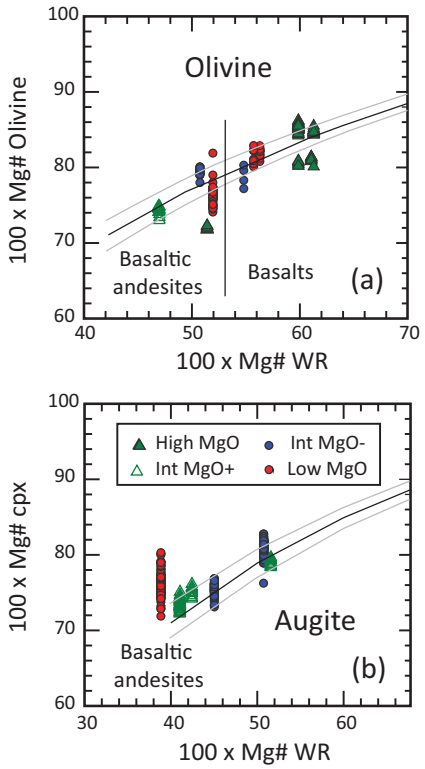

Fig. 7. Rhodes diagrams plotting the Mg# of the whole-rocks (WR) vs the Mg# of (a) olivine and (b) augite. Curves were calculated with a K_D^{Fe-Mg} of 0·3 for olivine (Roeder & Emslie, 1970) and 0·27 for augite (Putirka, 2008). Microprobe profiles displaying a clear compositional difference between the core and the rim were selected. Indeed, a profile with a nearly constant composition could represent only one zone of a zoned crystal because of a cutting effect. The central black curve was calculated with the equilibrium K_D^{Fe-Mg} and the light grey curves were calculated with error bounds of 0·03 for K_D^{Fe-Mg}. FeO_t was used in the calculations.

2018). One of the least differentiated basalt samples (PIC 50) has been collected from a dyke (Fig. 3a). The La Picada trend is at the boundary between the tholeiitic and calc-alkaline fields (Irvine & Baragar, 1971) (Fig. 3b) and at the boundary between the low-K tholeiite and calc-alkaline fields, except for some dacites that are higher in K_2O and thus plot in the calc-alkaline field (Peccerillo & Taylor, 1976) (Fig. 3c). The least differentiated compositions are tholeiitic basalts. Interstitial glass pockets are dacitic in the dacites, but with higher SiO_2 than the whole-rocks and dacitic to rhyolitic in the basalts and basaltic andesites, with the exception of one andesitic glass analysed in a basalt. The composition of the glass pockets in the basalts and basaltic andesites is rather scattered, particularly for FeO_t, TiO_2 and Al_2O_3. This scatter is probably due to their very small size and to the presence of some microcrystals of oxides and/or plagioclase as the electron microprobe beam was defocused during their analysis. The composition of these glass pockets should be different from the composition of the interstitial liquid of the basaltic to basaltic andesitic crystal mush as most microlites crystallized during final magma ascent to the surface (e.g. Erdmann *et al.*, 2016). We have calculated the composition of such an interstitial melt for sample PIC33 by subtracting the composition of the macrocryst assemblage from the composition of the bulk-rock. In this calculation, we used the proportions of macrocrysts measured by point counting. The composition of the macrocrysts was taken as the average of all analyses of each mineral present in sample PIC33. Sample PIC33 was selected because it is the most evolved basaltic andesite, analyses are available for all macrocrysts and the proportions of macrocrysts were measured three times, the average being used in the calculation. The calculated matrix is andesitic, similar to the andesitic glass pocket analysed in a basalt and slightly less differentiated than the dacites from the glass pockets and the dykes (Supplementary Data Fig. S6).

Major elements

In Harker diagrams (Fig. 8 and Supplementary Data Fig. S6, Table 1), MgO, FeO_t and CaO decrease with increasing SiO_2, whereas K_2O and P_2O_5 increase, but only slightly for P_2O_5. TiO_2 is relatively constant with differentiation, whereas Al_2O_3 is at first constant and then decreases with increasing SiO_2 in the dacites. Contrarily, Na_2O first increases and then remains constant in the dacites. In the MgO–SiO_2 diagram, basalts and basaltic andesites display variable MgO contents for a given value of SiO_2. We have thus discriminated these samples as High-MgO and Low-MgO, as well as Intermediate (Int)-MgO^+ and Intermediate (Int)-MgO^- for MgO contents plotting between the High- and Low-MgO samples, the Int-MgO^+ samples having slightly higher MgO contents than the Int-MgO^- samples. Low-MgO samples are also higher in Al_2O_3 than the High-MgO samples. These differences are indeed due to variable MgO contents and not to variable SiO_2 contents as they are observed in all major elements variation diagrams when MgO is used as a differentiation index.

Trace elements

Ni and Cr strongly decrease with increasing SiO_2 (Fig. 9, Table 1) and to a lesser extent, Sc, V and Co, whereas Zn and Ga are rather constant (not shown). Rb, Ba, Cs (not shown) and High Field Strength elements (HFSE) (Zr, Hf, Nb, Ta, U, Th, Y, REE) are incompatible, whereas Sr remains first constant but is lower in the dacites. The Pb data (not shown) display a rather constant trend in the basalts and basaltic andesites and then a strong increase in the dacites. LREE are slightly fractionated with $(La/Yb)_N$ overlapping among the High-MgO to Low-MgO samples and displaying a restricted range from 2·44 in the least differentiated sample (PIC50) to 3·67 in the most evolved dacite (PIC41) (Fig. 10; Table 1). There is a slightly negative to virtually absent Eu anomaly in the basalts and basaltic andesites ($(Eu/Eu^*)_N$ = 0·87 to 1·06) and a slightly more negative one in the dacites ($(Eu/Eu^*)_N$ = 0·60 to 0·85) (Table 3). N-MORB normalized

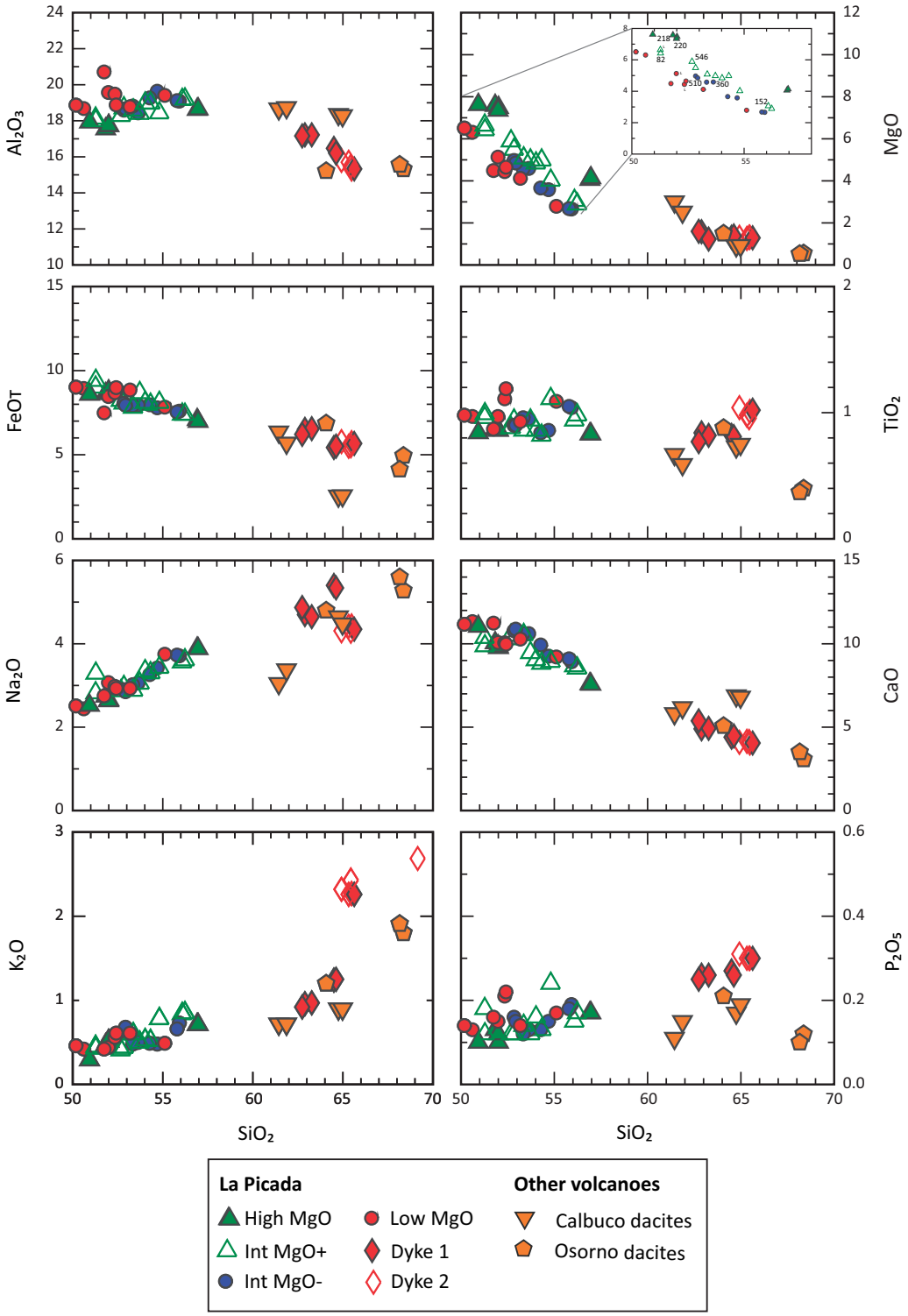

Fig. 8. Harker diagrams showing the major element composition of the La Picada lavas and dykes as well as the Osorno (Moreno *et al.* (2010) and unpublished data) and Calbuco dacites (Sellés & Moreno, 2011). Inset in the MgO diagram displays the position of the Moreno *et al.* (2010) samples (L) and the Ar–Ar ages in ka (Moreno *et al.* (2010) and this study). Analyses recalculated to 100% on a volatile free basis with total Fe as FeO_t.

trace element patterns (Fig. 10) are typical of arc magmas with strong enrichments in LILE (Rb, Cs, Ba), as well as in Th and U, negative anomalies in Nb and Ta that display similar contents to N-MORB and positive anomalies in Pb, as well as in Sr, for the basalts and basaltic andesites. We observe differences in the trace element composition of dacitic samples from dykes 1 and 2: compared to the former, the latter are enriched in

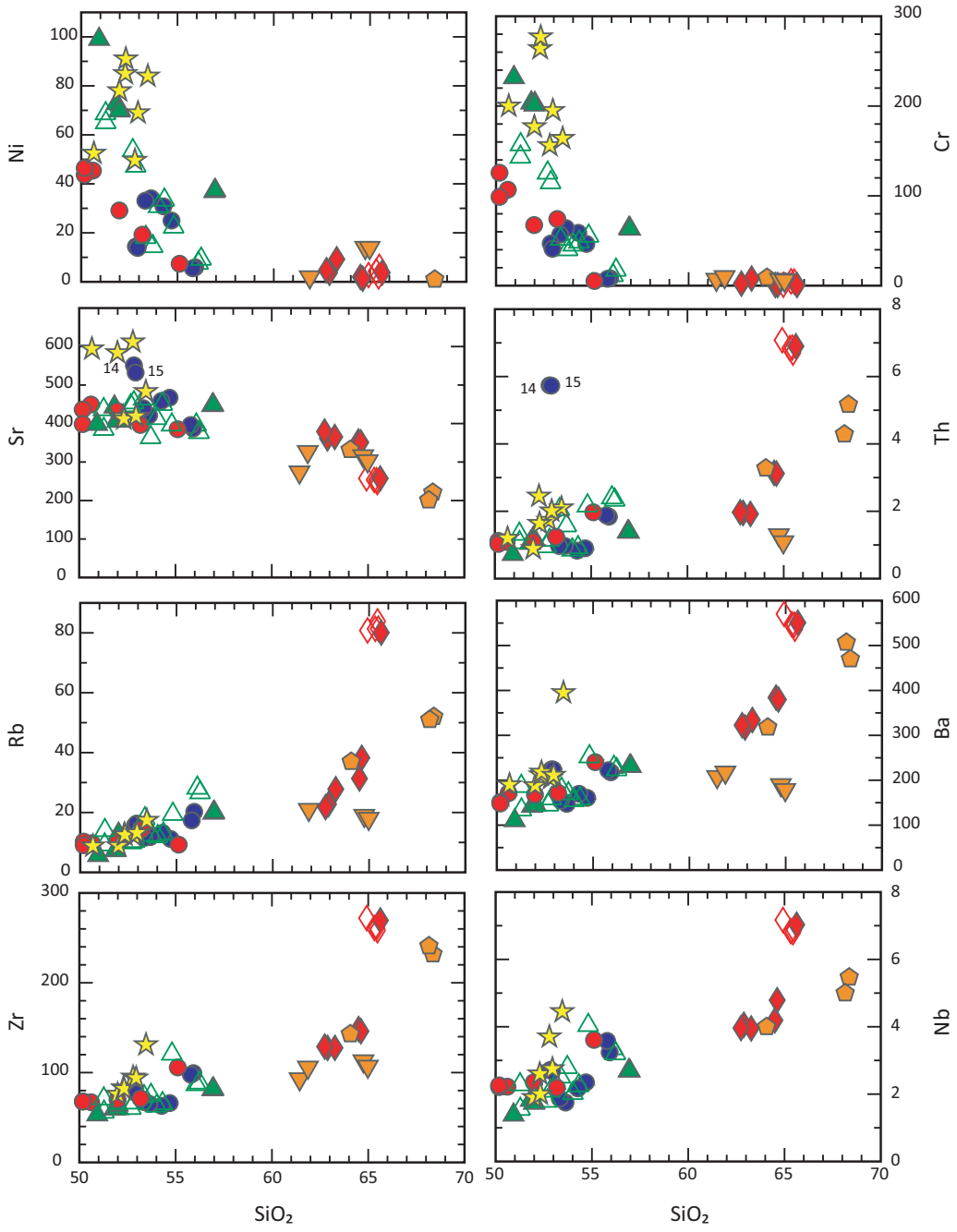

Fig. 9. Harker diagrams showing the trace element composition of the La Picada lavas and dykes, the Minor Eruptive Centers (MEC : Lopez Escobar *et al.*, 1995) and the Osorno (Moreno *et al.* (2010) and unpublished data) and Calbuco dacites (Sellés & Moreno, 2011). Same symbols as in Fig. 8 (MEC shown as yellow stars).

Rb, Ba, Cs, Pb and HFSE (Fig. 9) and display a more pronounced Eu negative anomaly (Eu/Eu* = 0·60 to 0·67, with an average of 0·64 vs 0·81 to 0·87, with an average of 0·84) (Fig. 10). These differences cannot be attributed to analytical uncertainties, as they were verified with XRF analyses for a few elements (Rb, Sr, Y, Zr, Zn, Ni, Pb).

High-, Low- and Int-MgO samples display overlapping trace element compositions, except for Cr and Ni that are distinctly higher in the High-MgO samples than in the Low-MgO samples. Samples PIC14 and 15 (Int-MgO^-) are conspicuously rich in Sr, Th and U. This observation has been tested by replicating the ICP-MS analyses on several aliquots (three for PIC14 and two for PIC15; averages are shown in Fig. 9). The trace element compositions can be compared to data for Chile trench sediments (Lucassen *et al.*, 2010; Plank, 2014) and to the South Atlantic MORB field (Fig. 11). Indeed,

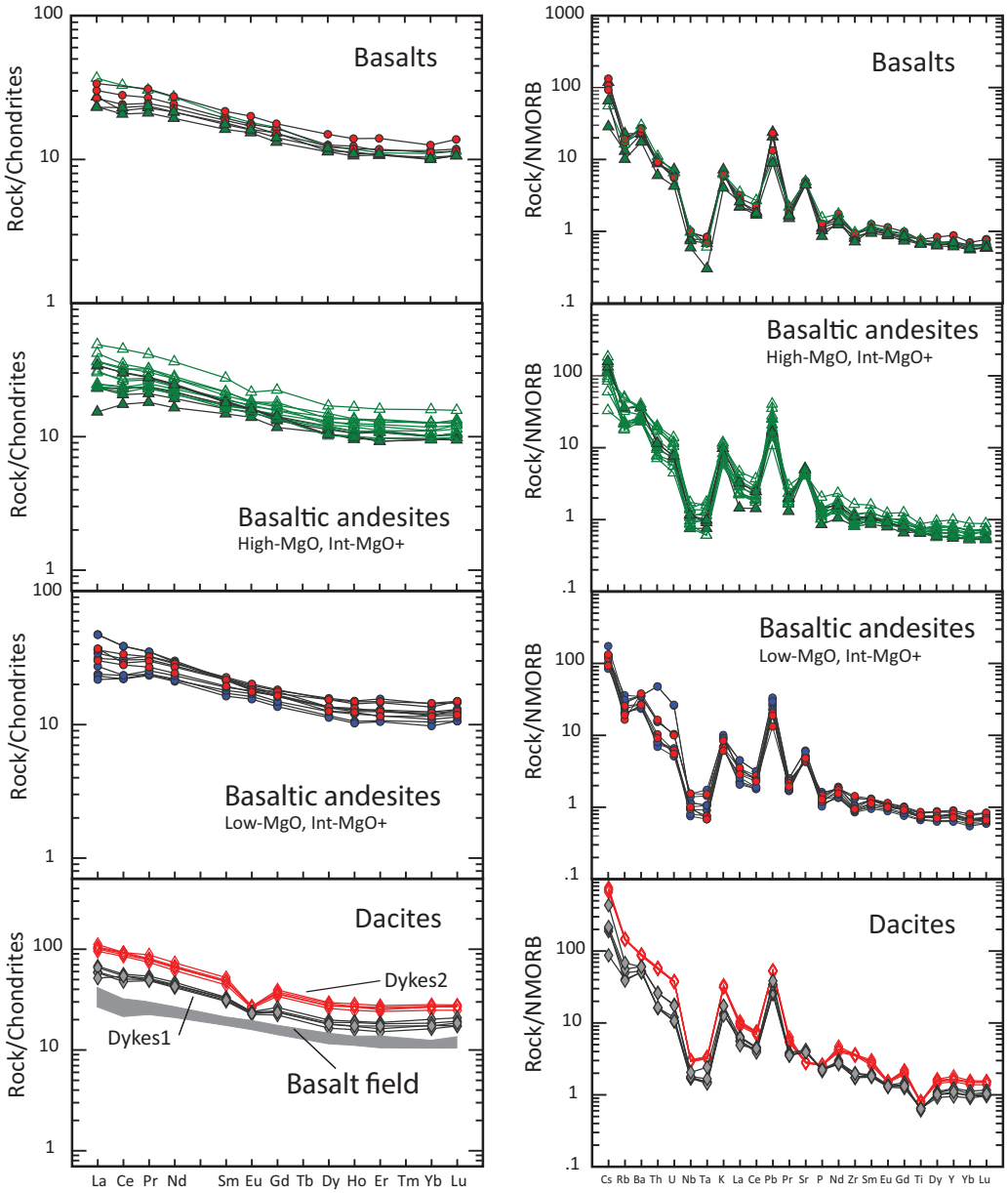

Fig. 10. REE patterns (left panel) normalized to C1 chondrite of Sun & McDonough (1989) and trace element patterns (right panel) normalized to N-MORB of Sun & McDonough (1989) for the La Picada lavas and dykes. Same symbols as in Fig.8, except for the dacites.

according to Husson *et al.* (2012) who modelled the flow of the South Atlantic mantle under the South American continent, this part of the mantle is convecting westward under the Andes and above the subducting Nazca plate. Moreover, Jacques *et al.* (2013) showed that the mantle source of the back-arc volcanic rocks of the TSVZ has a South Atlantic affinity. In the Nb/Yb vs Th/Yb diagram of Pearce & Peate (1995) (Fig. 11a), the La Picada samples have higher Th/Yb ratios than MORB, but lower than the Chile trench sediments. In the La/Sm vs Ba/Th plot of Elliott (2003) (Fig. 11b), they overlap in composition with South Atlantic MORB and are stretched towards the field of the Chile trench sediments. They display higher $(Ba/Nb)_N$, $(La/Nb)_N$ and $(Sr/Nb)_N$ ratios than South Atlantic MORB (Fig. 11c, d), but show no enrichment in Ba/Th (Fig. 11b). Finally, the La Picada samples and the Chile trench sediments have partly overlapping compositions in the $(Nb/U)_N$ vs $(Ce/Pb)_N$ diagram (Fig. 11e). The Low- and High-MgO basalts have overlapping normalized trace element patterns, particularly for the elements that track the slab components (Th, La, K, Pb, U, Sr) (Fig. 11f), but the High-MgO samples have a slightly higher $(Ba/Nb)_N$ (Fig. 11c) than the Low-MgO samples, and several High-MgO samples have a higher $(Sr/Nb)_N$ ratio (Fig. 11d) and a lower $(Ce/Pb)_N$ ratio (Fig. 11e) than

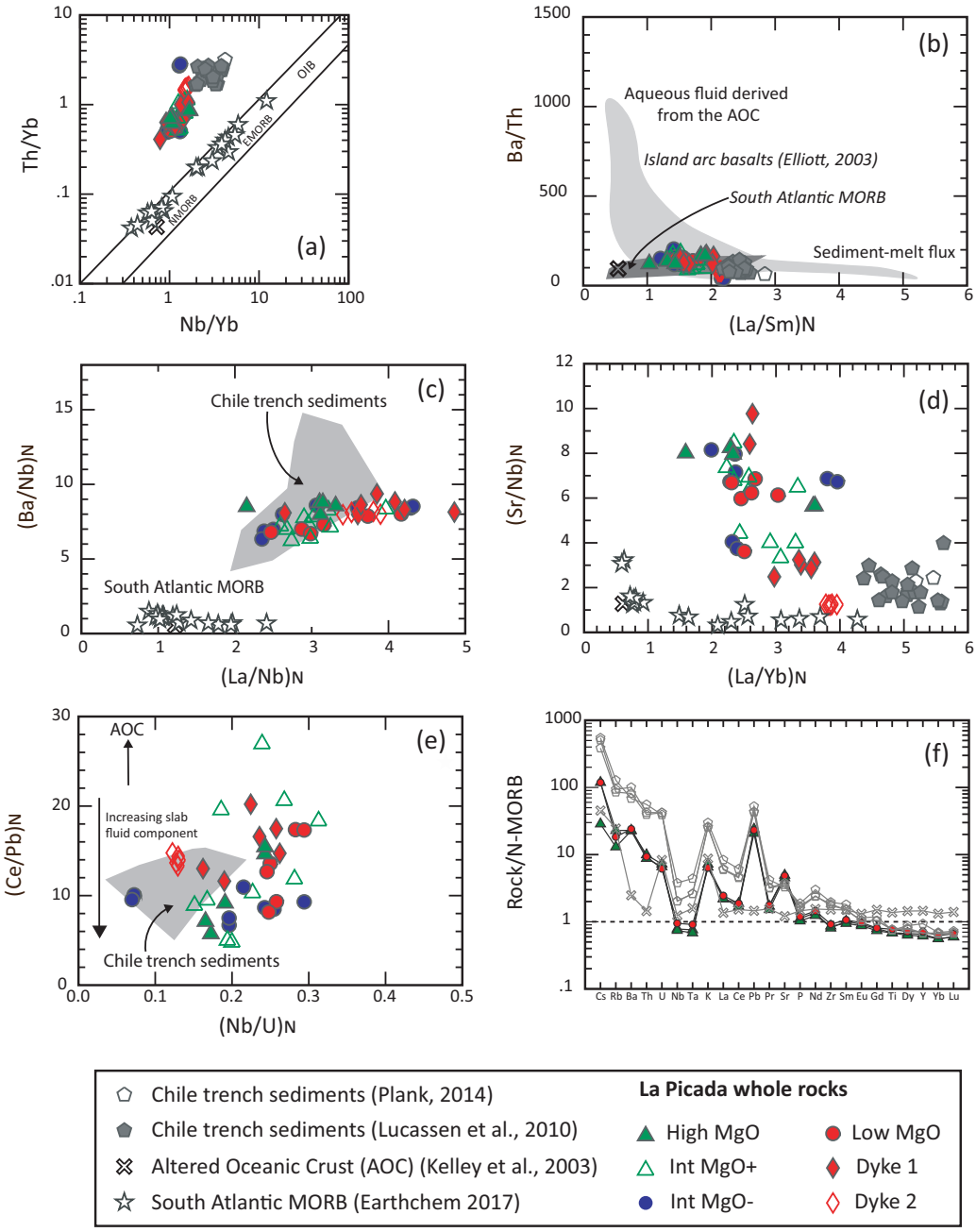

Fig. 11. Trace element composition of the La Picada lavas, compared with selected occurrences from elsewhere. (a) Th/Yb vs Nb / Yb diagram of Pearce & Peate (1995). (b) Ba/Th vs La/Sm (N is normalized to C1 chondrite of Sun & McDonough (1989)) diagram of Elliott (2003). The light grey field is the composition of island arcs basalts from Elliott (2003) and the dark grey field is the composition of South Atlantic MORB. (c) $(Ba/Nb)_N$ vs $(La/Nb)_N$. (d) $(Sr/Nb)_N$ vs $(La/Yb)_N$. (e) $(Ce/Pb)_N$ vs $(Nb/U)_N$. (f) Trace element patterns normalized to N-MORB of Sun & McDonough (1989) (note that the comparison concerns here only the composition of the basaltic parent magmas).

the Low-MgO samples. However, when all samples are taken into account, their variable ratios of incompatible elements overlap.

Ar–Ar ages

Samples PIC04 and PIC06 display, respectively, four and five continuous steps with 100% of degassed ^{39}Ar. The best estimated ages are calculated with a normal isochron giving an age of 218 ± 60 ka for PIC04 and of 220 ± 36 ka for PIC06 (Figs 12a and b). No plateau ages were obtained for PIC07, PIC09 and PIC12; however good estimated ages were calculated with a normal isochron (360 ± 23 ka for PIC07, 546 ± 88 ka for PIC09 and 152 ± 14 ka for PIC12: Fig. 12c–e). PIC07 yields a trapped Ar/Ar ratio that does not overlap with the atmospheric

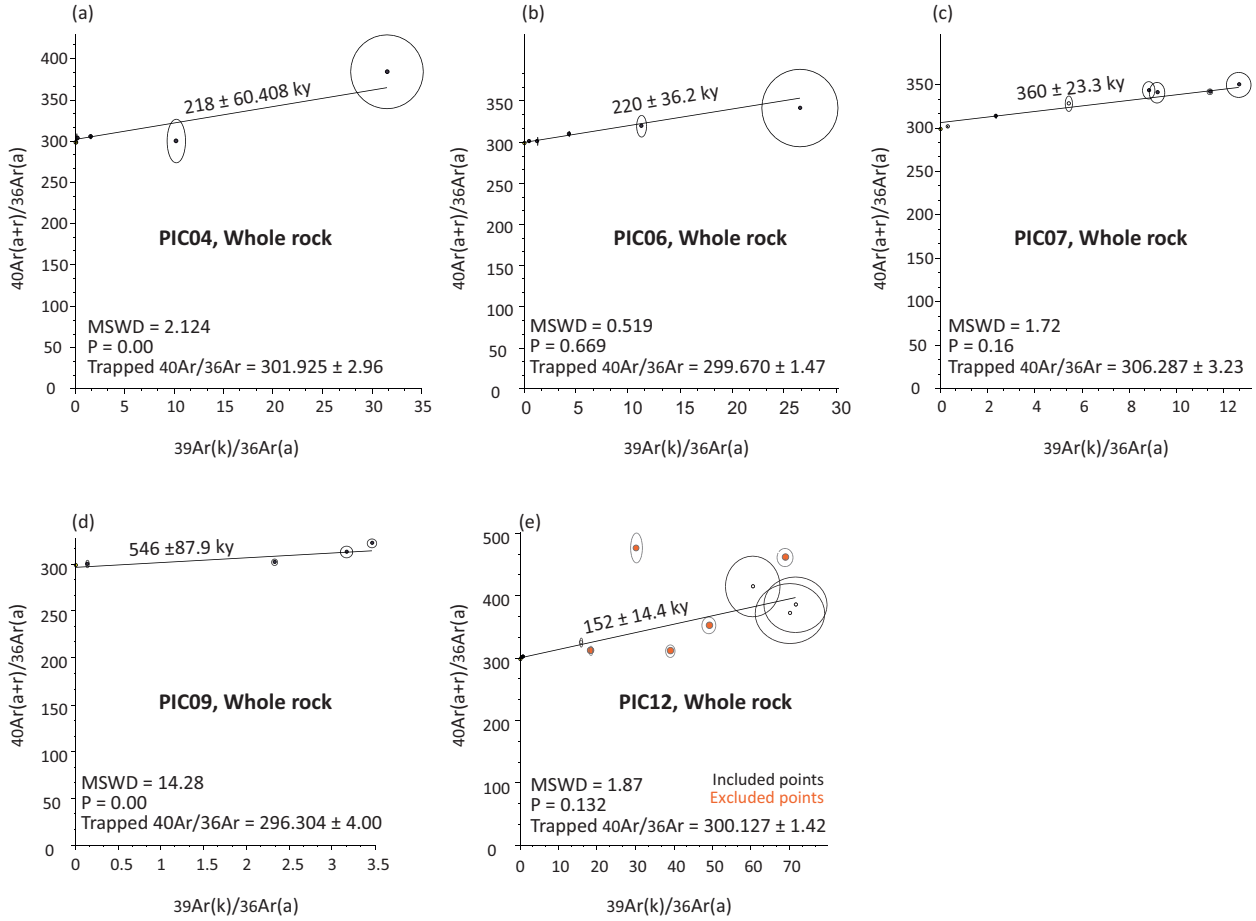

Fig. 12. Age spectra and isochrons showing Ar/Ar experimental results for samples (a) PIC04, (b) PIC06, (c) PIC07, (d) PIC09, (e) PIC12. Data are given in Table 2.

composition, suggesting a contribution from an excess Ar component. No satisfactory plateau age could be obtained for PIC11, a gabbroic block, and the best age estimation is given by the inverse isochron (9·5512 ± 0·89 Ma). Moreover, the composition of the trapped Ar/Ar does not overlap with the atmospheric composition, suggesting a significant amount of excess Ar. Reliable age criteria given by McDougall & Harrison (1999) are not always fully met due to the low K content and young age of the samples. Only PIC06 meets all criteria and, therefore, other ages must be cautiously considered although they remain meaningful. These new ages combined with previous results (Moreno *et al.*, 2010) indicate a continuous eruptive history at La Picada from about 546 ka (this study) to 60 ka (Moreno *et al.*, 2010). This activity was overlapping with that of Osorno (198 ka (Moreno *et al.*, 2010) to present) and Calbuco (342 ka (Sellés & Moreno, 2011) to present), starting, however, significantly earlier. La Picada thus recorded the early magmatic history of the Osorno–Puntiagudo–Cordón Cenizos active volcanic chain. There is no clear correlation between the age of the La Picada samples and their MgO content (Fig. 8). For example, samples PIC09 and PIC12 which are both Int-MgO^+ were respectively dated at 546 ± 88 ka and 152 ± 14 ka, thus covering nearly the whole period of activity at La Picada. The approximate age of 9·55 Ma obtained for the gabbroic fragment (PIC11) confirms that it belongs to the Miocene plutonic rocks forming the basement of the volcanoes in the area (Lambert & Wyllie, 1972).

Thermobarometry

A collection of geothermobarometers was used to estimate the depth (P) and the conditions (T, fO_2, H_2O) of differentiation from the basalts to the basaltic andesites and dacites.

The composition of clinopyroxene in equilibrium with the melt is dependent on pressure and can thus be used as a geobarometer, as proposed by Putirka (2008) (equation 32a). An improved version of this geobarometer (SEE = ± 0·14 GPa) was recently proposed by Neave & Putirka (2017) and can be applied to hydrous and anhydrous systems when temperature is above 1100°C and logfO_2 lower than QFM + 1 (see below). We selected clinopyroxene compositions that are in equilibrium with the whole-rock: $K_D^{Fe-Mg} = 0{\cdot}27 \pm 0{\cdot}03$ and $(DiHd)_{predicted} - (DiHd)_{observed} \leq |0{\cdot}05|$(Neave & Putirka,

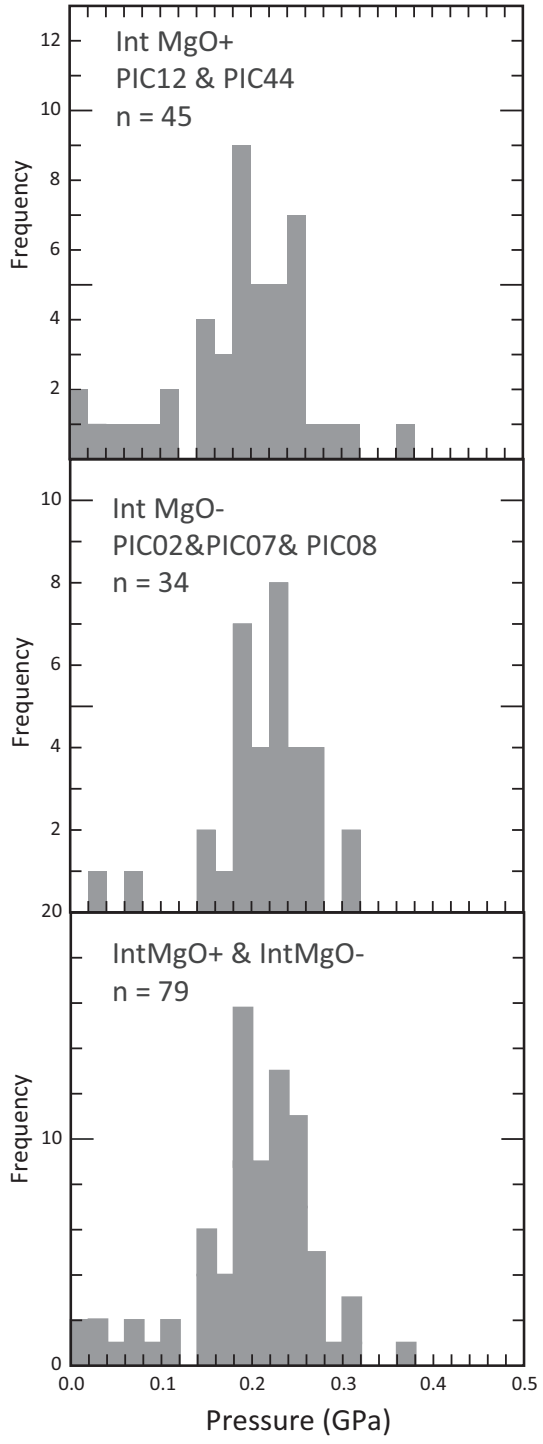

Fig. 13. Frequency distributions of pressure (GPa) estimated with the Neave & Putirka (2017) clinopyroxene-melt geobarometer for the Int-MgO^{+} and Int-MgO^{-} basaltic andesites (n, number of analyses).

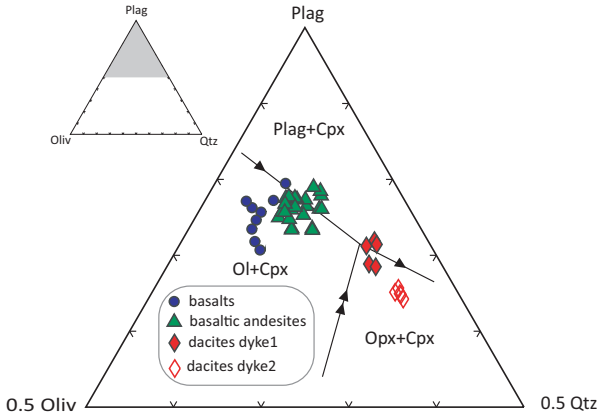

Fig. 14. Compositions of the La Picada whole-rock samples in the pseudoternary projection Olivine (Oliv)–Plagioclase (Plag)–Quartz (Qtz) projected from Clinopyroxene. Only the upper half of the triangle is shown (from 50% Oliv–50% Qtz to 100% Plag). The phase boundaries are those experimentally constrained by Grove *et al.* (2003) at 0·2 GPa and NNO for primitive arc magmas from the Cascades. Arrows indicate liquid evolution with decreasing temperature.

2017). This appeared to be true for several basaltic andesites (PIC02, 07, 08, 12 and 44) (Supplementary Data Table S7). Results indicate an average of 0·19 ± 0·07 GPa when considering all analyses, of 0·18 ± 0·08 GPa for the Int-MgO^{+} samples (PIC12 and 44) and of 0·21 ± 0·06 GPa for the Int-MgO^{-} samples (PIC02, 07, 08). Standard deviations of our results are given as the errors, as the pressure distribution probably reflects the uncertainty of the model (Neave & Putirka, 2017). These standard deviations are slightly lower that the SEE of 0·14 GPa given by Neave & Putirka (2017). The frequency distributions (Fig. 13) display overlapping maxima (0·18 to 0·26 GPa for the Int MgO^{+}; 0·18 to 0·28 GPa for the Int MgO^{-}) and except for a few analyses, pressures are below 0·3 GPa. Using a density of 2700 kg/m^3 for the upper crust (Tassara *et al.*, 2006), the pressures of 0.18 ± 0·08 to 0·28 ± 0·06 GPa translate into depths of 6·8 ± 3 km to 10·6 ± 2·3 km. Interestingly, this range of depths corresponds to the intracrustal discontinuity separating the upper and lower continental crust in this part of the Andean arc (Tassara *et al.*, 2006; Tassara & Echaurren, 2012). A low pressure of differentiation is supported by phase equilibria as the basaltic andesites and dacites of La Picada respectively plot close to the 0·2 GPa clinopyroxene-saturated olivine–plagioclase and orthopyroxene–plagioclase boundaries of Grove *et al.* (2003) (Fig. 14). It also agrees with the results of Turner & Langmuir (2015a) and Adam *et al.* (2016) and with the pre-eruptive conditions (0·2 GPa) experimentally constrained for the dacite of the San Pedro volcano (36°S SVZ) (Costa *et al.*, 2004). We thus conclude that differentiation from the basalts to the basaltic andesites and dacites dominantly took place in the upper crust.

Following the procedure proposed by Mandler *et al.* (2014), we first estimated the temperature and the H_2O content of the magma by combining empirical thermometers that are either independent or dependent on the H_2O content of the melt (Putirka, 2008). The former only depend on the melt composition (equations 13 and 16 from Putirka (2008)) whereas the latter either depend

Table 4: Temperature and %H_2O estimates for a range of upper crustal pressures using the Mandler et al. (2014) test

Sample#	P (GPa)	T (°C) (±10)	%H2O (±0·3)
PIC30	0·1	1137	1·1
Low MgO	0·2	1141	1·0
	0·3	1145	1·0
	0·4	1149	0·9
PIC31	0·1	1142	1·1
Low MgO	0·2	1146	1·1
	0·3	1150	1·0
	0·4	1154	0·9
PIC43	0·1	1145	1·5
Int MgO+	0·2	1149	1·5
	0·3	1153	1·3
	0·4	1157	1·2
PIC06	0·1	1163	1·5
High MgO	0·2	1167	1·4
	0·3	1171	1·4
	0·4	1175	1·3
PIC50	0·1	1171	1·2
High MgO	0·2	1175	1·1
	0·3	1181	1·0
	0·4	1183	0·9

on the composition of the melt (equations 14 and 15 of Putirka (2008)) or on the olivine-melt equilibrium (equations 22 and 21 of Putirka (2008)). We used a K_D $(Fe–Mg)^{ol–liq} = 0{\cdot}30 \pm 0{\cdot}03$ (Roeder & Emslie, 1970) as a test of equilibrium. The equations involving plagioclase were not considered at this stage because, as already stated above, its composition is controlled by several parameters thus precluding a simple equilibrium test. The temperature calculated with the H_2O-dependent equilibria strongly varies with the water content, that we allowed to increase from 0 to 4%, whereas the temperature of the no-H_2O term equilibria is nearly constant (a small change in the melt composition produced by the addition of an increasing amount of H_2O induces a slight temperature variation). A maximum of 4 wt % H_2O was considered based on the absence of amphibole in all La Picada samples. The intersection of the two groups of thermometers provides an estimation of the H_2O content of the magma. In the case of the Calbuco volcano (Montalbano *et al.*, 2017), the H_2O contents derived from the Mandler test and measured in olivine-hosted melt inclusions agree, suggesting that this test provides robust information. Calculations were performed at different pressures (0·1, 0·2, 0·3 and 0·4 GPa) for the High-MgO (PIC06, PIC50), Int-MgO^+ (PIC43) and Low-MgO (PIC30, PIC31) basaltic parent magmas (Table 4 and Supplementary Data Table S8). In these calculations, the bulk-rock compositions of the basalts were interpreted as representative of liquid compositions as they are in equilibrium with the cores of the olivine (Fig. 7). Total FeO was used, as the effect of the Fe^{3+}/Fe^{2+} ratio is negligable on temperature calculated with the olivine thermometers. Indeed, nearly identical temperatures and wt % H_2O were obtained for basalt PIC43 when considering total FeO or a FeO fraction of 0·9, appropriate for oxygen fugacities between FMQ and NNO (Putirka, 2008) (see Supplementary Data Table S8). Results indicate a liquidus temperature range of about 1140 to 1180°C (± 10°C) and an H_2O content varying from 1·0 to 1·5 wt % (± 0·3 wt %) at 0·2 GPa among the different basalts. This temperature range is in agreement with experimental data performed on starting compositions similar to the La Picada basalts (Draper & Johnston, 1992; Hamada & Fujii, 2008; Blatter *et al.*, 2013; Nandedkar *et al.*, 2014). The plagioclase hygrometer proposed by Waters & Lange (2015) was then used to further constrain the water content of the

Table 5: Calculated % H_2O contents using the Waters and Lange (2015) hygrometer

Sample #	% An (cores)	T (°C)	% H_2O (±0·35)
PIC30	0·9	1160	2·6
Low MgO		1150	2·7
		1140	2·9
		1130	3·0
		1120	3·6
	0·8	1160	2·3
		1150	2·5
		1140	2·6
		1130	2·8
		1120	3·6
PIC31	0·9	1160	2·5
Low MgO		1150	2·7
		1140	2·8
		1130	2·9
		1120	3·1
	0·8	1160	2·3
		1150	2·4
		1140	2·6
		1130	2·7
		1120	2·8
PIC43	0·9	1170	1·9
Int MgO+		1160	2·0
		1150	2·2
		1140	2·3
		1130	2·5
	0·8	1170	1·7
		1160	1·8
		1150	1·9
		1140	2·1
		1130	2·2
PIC06	0·9	1190	1·1
High MgO		1180	1·3
		1170	1·4
		1160	1·5
		1150	1·7
	0·8	1190	0·9
		1180	1·0
		1170	1·2
		1160	1·3
		1150	1·4
PIC50	0·9	1190	1·5
High MgO		1180	1·6
		1170	1·8
		1160	1·9
		1150	2·0
	0·8	1190	1·3
		1180	1·4
		1170	1·5
		1160	1·7
		1150	1·8

P, 0·2 GPa, plagioclase core composition (% An).

magma given that its standard error estimate (SEE) is 0·35 wt % H_2O. As this hygrometer depends strongly on temperature and plagioclase composition, but only slightly on pressure, the H_2O content was calculated at 0·2 GPa using, for each basalt, the temperature obtained with the procedure of Mandler *et al.* (2014) at this pressure and the range of compositions measured in the plagioclase cores of the basalts (X_{An} = 0·9 to 0·8) (Fig. 5a; Table 5). The choice of the plagioclase core composition is supported by two observations made for olivine. Firstly, the Fo-rich cores are in equilibrium with the bulk-rock composition and secondly, olivine has a higher Fo content in the High-MgO samples compared to the olivine of the Low-MgO samples (Fig. 7). Calculated H_2O contents are higher than the estimations from the Mandler *et al.* (2014) test, except for PIC06, and suggest a slight difference between the High-MgO (0·9–1·8 wt % H_2O) and Low-MgO basalts (2·3–3·1 wt % H_2O). Given the SEE of the plagioclase hygrometer (± 0·35 wt % H_2O), this increase seems to be significant, but small. In the following, we use the H_2O content calculated with An_{90} and the upper temperature of the Mandler *et al.* (2014) test: 2·5 wt % (Low-MgO), 1·5 wt % (Int-MgO+), 1·1 wt % (High MgO). These water contents are lower than or at the lower limit of the 2–6 wt % H_2O range obtained for mafic arc magmas in a series of volcanic arcs (Cascades, Aleutians, Mexico, Marianas, Kamchatka, Tonga, Centam; Plank *et al.*, 2013) but are in agreement with the observed mineralogy. The absence of amphibole indeed indicates an H_2O content lower than 4–6 wt % in the differentiated facies (e.g. Sisson & Grove, 1993; Andújar *et al.*, 2015) translating into a maximum of 1.6 to 2.4 wt % H_2O in the parent magmas if 60% differentiation (fraction of residual liquid = 0.4) is considered (see below). They are also concordant with results from Watt *et al.* (2013) who measured water contents between 1.3 and 2.1 wt % in olivine-hosted melt inclusions from several volcanoes of the SVZ (Hornopiren, South Michinmavida and Palena) (Fig. 1). We have no precise constraints on the CO_2 content of the La Picada magmas as pyroclasts unequivocally belonging to this volcano and carrying olivine with glassy melt inclusions were not recognized in the field. However, the highest CO_2 content reported by Watt *et al.* (2013) for their set of melt inclusions is 1238 ppm. The pressure of volatile saturation was thus estimated with the VolatileCalc_2.0 model of Newman & Lowenstern (2002) using an H_2O and CO_2 content of respectively 1·1 to 2·5 wt % and 1200 ppm and a temperature range of 1140–1180°C. Results indicate that under these conditions the La Picada magmas were volatile saturated at 0·25–0·3 GPa. Volatiles exsolution increases the viscosity of the magma as it promotes the polymerization of the melt structure and crystallization. However, it should also reduce the bulk density of the resultant vesicular magma. Consequently, if volatile exsolution indeed favored the stalling of the magma at about 0·2 GPa (Plank *et al.*, 2013), it suggests that the proportion of bubbles in the magma was never large and/or that the density contrast between fluid and melt was lower at that depth. As mentioned above, the presence of the intracrustal discontinuity at this pressure range is also a likely controlling factor and it is possible that volatile exsolution and crustal structure played a role concomitantly.

The oxygen fugacity was estimated with the temperature derived from the thermometers used in the Mandler *et al.* (2014) test and the composition of titanomagnetite. Estimates range from QFM + 0·5 (PIC14 at 1098°C, PIC50 at 1175°C) to QFM + 0·2 (PIC33 at 1067°C). Andújar *et al.* (2015) experimentally studied the Balos basalt from Santorini that is very close in composition to our sample PIC50. Using their experimental results, these authors derived an empirical equation giving the forsterite content of the olivine as a function of temperature, H_2O content of the melt and oxygen fugacity: Fo (mol %) = 0·1037 x T (°C) + 1·7638 x H_2O_{melt} (wt %) + 3·0234 x ΔNNO - 38·63. Considering the composition of olivine in PIC50 ($F0_{85}$), a temperature of 1175°C derived from the Mandler *et al.* (2014) test and an H_2O content varying from 1·1 to 1·8 wt %, the calculated oxygen fugacity is NNO-0·1 to NNO-0·5 corresponding to QFM + 0·8 and QFM + 0·40, respectively. These values overlap with those derived with the titanomagnetite composition and agree with the oxygen fugacity generally obtained for basalts that straddle the tholeiitic-calc-alkaline boundary (Sisson *et al.*, 2005). In the following, we will consider an oxygen fugacity of QFM + 0·5, close to NNO.

DISCUSSION

Geochemical variability at La Picada

As detailed above, basalts and basaltic andesites at La Picada display variable MgO, Al_2O_3, Cr and Ni contents at a given SiO_2 content, justifying the distinction between High-, Low- and Int-MgO samples (Figs 8 and 9). In the following, we discuss three processes that could potentially explain this observation: (1) preferential entrainment of plagioclase or ferromagnesian macrocrysts from the magma storage region's crystal mush, inducing lower MgO, Cr, Ni and higher Al_2O_3 contents in the Low-MgO samples; (2) differentiation of the same parent magma at different pressures, as higher pressure respectively expands and decreases the stability fields of clinopyroxene and plagioclase, thus inducing lower MgO (Yoder, 1976); and (3) variable extent of fractional crystallization of the same parent magma. Entrainment of macrocrysts is probably not a reasonable assumption as it would produce more scattered data. It has nonetheless been tested quantitatively as the relative proportions of plagioclase and ferromagnesian minerals are slightly higher in the Low-MgO samples than in the High-MgO samples (Fig. 15). We have thus verified if adding 5 to 10% plagioclase to the composition of the High-MgO basalt could reproduce the composition of the Low-MgO basalt. Results are presented in Table 6a. The trace element content of

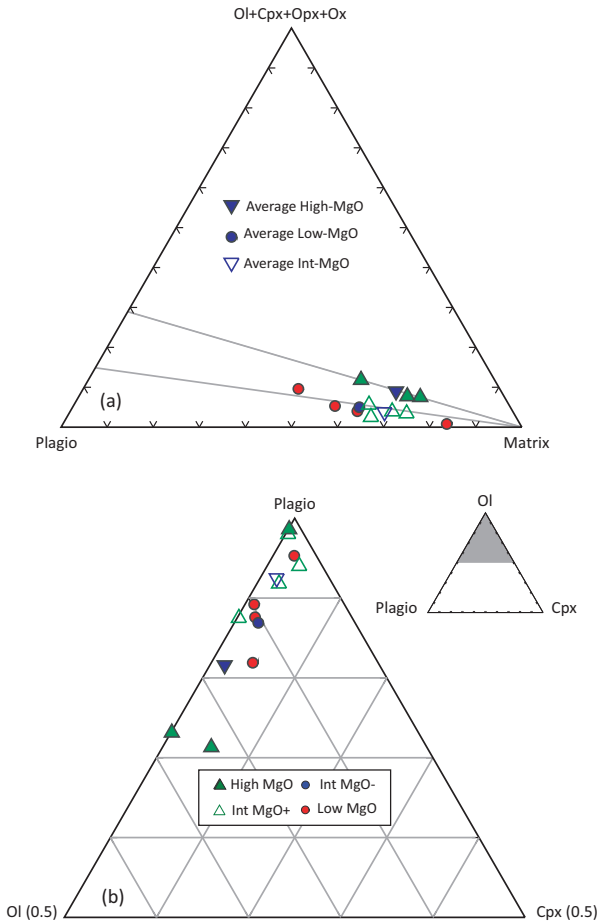

Fig. 15. Relative proportions of macrocrysts and matrix (a) and of macrocrysts (b) in the basalts and basaltic andesites as obtained from point counting. The two lines joining the « Matrix » corner with the Ol+Cpx+Opx+Ox–Plagio segment in (a) indicate a slightly higher proportion of plagioclase in the Low-MgO samples.

plagioclase in equilibrium with the High-MgO basalt was calculated using the trace element content of basalt PIC50 (High-MgO) and appropriate partition coefficients (see Table 10 below). Eu and Sr are commonly used as a test for plagioclase accumulation because plagioclase preferentially incorporates these elements. However, we note that, as the calculated Eu and Sr contents of plagioclase are respectively low and moderate (Table 6a), loading the High-MgO basalt with plagioclase does not have much effect on the resulting Eu and Sr contents of the magma. Consequently, the similar Sr (Fig. 9) and REE (Fig. 10) patterns of the High- and Low-MgO samples does not necessarily preclude plagioclase accumulation. Contrarily, results clearly indicate that FeO_t, MnO, Cr and Ni are too high in the calculated composition compared to the Low-MgO samples. Consequently, even if some plagioclase accumulation may have occurred in the Low-MgO samples, as suggested by their higher proportion of plagioclase, this process cannot take into account the geochemical variability at La Picada. We have also tested the possibility that different entrainment of olivine and clinopyroxene produced the variable MgO, Al_2O_3, Cr and Ni contents (titanomagnetite was not considered as it is not present as a macrocryst in the basalts and basaltic andesites). As Ni is preferentially incorporated in olivine and clinopyroxene, whereas Cr substitutes in clinopyroxene, these trace elements were used to calculate the amount of olivine and clinopyroxene that must be added to the composition of the Low-MgO basalt in order to obtain the observed Ni and Cr contents of the High-MgO basalt. These calculated proportions were then used to test if they can explain the different MgO and Al_2O_3 contents of the Low- and High-MgO samples. Results indicate that the calculated proportions of olivine (6%) and clinopyroxene (18%) added to the Low-MgO basalt fail to reproduce the observed MgO and Al_2O_3 contents of the High-MgO basalt (Table 6b). Preferential entrainment of macrocrysts cannot thus be retained as an explanation for the compositional diversity at a given SiO_2. The higher Fo content of olivine cores in the High-MgO samples, indicating equilibrium with a more magnesian melt, supports this conclusion. It is also worth noting that the high mass proportions of plagioclase in the La Picada lavas (Fig. 15) are very similar to the relative abundances of plagioclase and olivine ($Plag_{70}$: Ol_{30}) typically observed in the cumulus assemblages of many mafic layered intrusions (e.g. Rhum intrusion, Brown (1956); Kiglapait intrusion, Morse (1979); Sept Iles Layered Intrusion, Namur *et al.* (2011)) and calculated from experimental data (e.g. Grove & Baker, 1984; Toplis & Carroll, 1995).

Several experimental studies (e.g. Draper & Johnston, 1992; Müntener *et al.*, 2001; Grove *et al.*, 2003) have demonstrated that with increasing pressure, the stability field of clinopyroxene and plagioclase respectively expands and decreases. Moreover, at high pressure, garnet becomes stable. Here, we focus on the experiments of Draper & Johnston (1992) (1 atm, 1, 1·2, 1·5, 2 GPa; anhydrous conditions) because their starting composition is very close to the La Picada basalts. Their dataset indicate that the composition of the liquids becomes increasingly enriched in Na_2O and K_2O and depleted in CaO with increasing pressure. The different samples of La Picada overlap for these three elements (Fig. 8) and are similar to the 1 atm liquid line of descent of Draper & Johnston (1992). Moreover, the experimental fractionation trend obtained at 0·4 GPa by Blatter *et al.* (2013) on a starting composition very close to the parent magma of La Picada, except that it is slightly higher in P_2O_5, Na_2O and TiO_2 and slightly lower in Al_2O_3 and CaO, also reproduces the trend observed in this study (Fig. 16). These upper crustal pressures are also in agreement with results obtained with the cpx-melt geobarometer. Thus fractionation at significantly different pressures cannot predict the geochemical variability. We have further tested the hypothesis of fractionation at slightly different pressures, between 0·2 and 0·4 GPa, by simulating the fractional crystallization of the PIC50 basalt (High-MgO) with the Rhyolite-Melts

Table 6a: Test of macrocrysts (plag) preferential entrainment

	PIC50 High-MgO	Plagioclase composition	Liq High-MgO + 10% plagio	Liq High MgO + 5% plagio	PIC30 Low-MgO	PIC31 Low-MgO
SiO_2	51·11	48·76	50·88	51·00	50·61	50·18
TiO_2	0·84	0·05	0·76	0·80	0·97	0·98
Al_2O_3	17·99	32·17	19·40	18·69	18·68	18·87
FeOt	8·61	0·80	7·83	8·22	8·94	9·02
MnO	0·15	0·00	0·14	0·14	0·17	0·17
MgO	7·65	0·00	6·88	7·27	6·31	6·51
CaO	11·08	16·28	11·60	11·34	11·33	11·17
Na_2O	2·17	2·55	2·21	2·19	2·44	2·51
K_2O	0·29	0·07	0·27	0·28	0·42	0·46
P_2O_5	0·10	0·00	0·09	0·10	0·13	0·14
Total	100·00	100·68	100·07	100·03	100·00	100·00
Sc	29	1·2	26	28	35	30
V	220	6·6	199	210	238	236
Cr	232	9	209	221	107	112
Co	37	3·3	33	35	34	33
Ni	99	12	90	95	45	45
Zn	60	10·2	55	57	74	70
Rb	5·6	0·1	5·1	5·4	10	10
Sr	398	676	426	412	449	436
Ba	110	26	102	106	171	150
Ce	13	1	12	13	15	15
Eu	0·9	0·2	0·9	0·9	1·2	1·0
Sm	2·7	0·1	2·5	2·6	3·3	2·9
Yb	1·8	0·0	1·6	1·7	2·1	1·9

The test is made for the accumulation of 10% to 5% of plagioclase in the High-MgO basalt represented by sample PIC50 to produce the composition of the Low-MgO basalts represented by samples PIC30 and PIC31. The major element composition of plagioclase is the average of 127 analyses (core, mantle, rim) of plagioclase from PIC50. The trace element composition was calculated with the partition coefficients of Table 10 (see below) and the trace element composition of PIC50. See text for explanation.

algorithm (Ghiorso & Gualda, 2015; Gualda *et al.*, 2012) at an oxygen fugacity of NNO and with 1·5 wt % H_2O in the starting composition. Results are illustrated in Fig. 16. MgO is indeed lower at 0·4 GPa and reaches the Low-MgO basalts after some fractionation of olivine and plagioclase, but at a higher SiO_2. Also, the 0·2 GPa trend is much lower in Al_2O_3 than the High-MgO samples. Finally, the 0·4 GPa trend is respectively much lower and much higher in CaO and in Na_2O than the Low-MgO samples because of clinopyroxene fractionation. In conclusion, fractionation at different pressures does not appear plausible, especially because the different trends of La Picada should have different Na_2O contents as this element is strongly influenced by the decreasing stability field of plagioclase with pressure (Fig. 8).

When using a perfectly incompatible element such as Zr as the differentiation index (Supplementary Data Fig. S9), the La Picada samples define a continuous trend of decreasing MgO, Ni and Cr with increasing Zr, suggesting that differentiation can explain the occurrence of the High- and Low-MgO basalts. A fractional crystallization model (see below, Supplementary Data Fig. S9) indeed perfectly fits the Ni–Zr data. Interestingly, when incompatible elements such as Rb, La or Ba are used as the differentiation index, the data are more scattered, perhaps because these elements are variably contributed by the slab component among the La Picada samples, whereas Zr is a 'conservative' element (Pearce & Peate, 1995) (Fig.11). We thus conclude that the High- and Low-MgO basalts result from a different extent of fractionation.

Mantle melting conditions under La Picada

The mantle melting conditions under La Picada were estimated with the Lee *et al.* (2009) and Putirka (2008) (equations 42, 13 and 14) geothermobarometers and the approach of Kelley *et al.* (2006) and Kelley *et al.* (2010). The Lee *et al.* (2009) and Putirka (2008) (equation 42) geothermobarometers are based on the equilibrium between a basaltic melt, olivine and orthopyroxene. They are thus appropriate here as primary basalts equilibrate with these minerals in their mantle source. The representative composition of the parent magmas was calculated as the average composition of samples PIC04, 05 and 06 for the High-MgO basalts and of samples PIC30 and PIC31 for the Low-MgO basalts. The High-MgO sample PIC50 was also selected. Their Mg# lower than 0·7 (e.g. Grove *et al.*, 2012) (0·6 for the High-MgO, 0·56 for the Low-MgO, 0·61 for PIC50) and Cr (202 for the High-MgO, 110 for the Low-MgO, 232 for PIC50) and Ni (71 for the High-MgO, 45 for the Low-MgO, 99 for PIC50) contents respectively lower than 232 ppm and 99 ppm preclude them to be primary magmas in equilibrium with a mantle source (>1000 ppm Cr, 400–500 ppm Ni). In order to estimate the temperature and pressure of last equilibration with the mantle source using the Lee *et al.* (2009) and Putirka (2008) (equations 42, 13 and 14) geothermobarometers, we have thus corrected the composition of the parent

Table 6b: Test of macrocrysts (ol, cpx) preferential entrainment

	Ni (ppm)	Cr (ppm)
High-MgO basalt (PIC05-06)	70	202
Low-MgO basalt (PIC37)	29	68
Olivine in equilibrium with PIC37	435	
Clinopyroxene in equilibrium with PIC37	120	816
$(Ni)_{High\text{-}MgO} = (Ni)_{Low\text{-}MgO}.\ X_{liq} + (Ni)_{ol}.X_{ol} + (Ni)_{cpx}.\ X_{cpx}.$		
$(Cr)_{High\text{-}MgO} = (Cr)_{Low\text{-}MgO}.\ X_{liq} + (Cr)_{cpx}.\ X_{cpx}.$		
$X_{liq} + X_{ol} + X_{cpx} = 1.$		
$--> X_{ol} = 0.06$ and $X_{cpx} = 0.18.$		
	Al_2O_3 (%) Observed	Al_2O_3 (%) Calculated
High-MgO basalt (PIC05-06)	17·72	15·23
Olivine	0·00	
Clinopyroxene	2·01	
	MgO (%) Observed	MgO (%) Calculated
High-MgO basalt (PIC05-06)	7·42	9·15
Olivine	38·00	
Clinopyroxene	16·50	

The following partition coefficients were used to calculate the Ni and Cr contents in olivine and clinopyroxene: DNi (ol/melt) = 15 (Kinzler *et al.* (1990)); DNi (cpx/melt) = 4·13; DCr (cpx/melt) = 12 (Norman *et al.*, 2005). The Al_2O_3 and MgO contents of olivine and clinopyroxene correspond to the core compositions in equilibrium with the WR. The Al_2O_3 and MgO contents of the High-MgO basalt were calculated using the proportions of liquid, olivine and clinopyroxene deduced from the trace elements. The whole rocks (matrix + macrocrysts) are considered as the liquid in these calculations and the test is made for additional olivine and clinopyroxene added to the Low-MgO basalt.

magmas in the following way. The experimental data of Draper & Johnston (1992) used sample ID-16, a primary magma from the Aleutian arc (Grove *et al.*, 2012), as a starting composition. At 1 atm, after 20·6% crystallization of a troctolitic cumulate (53·40% olivine + 46·60% plagioclase) from this sample, the residual liquid is very close in composition to the La Picada basalts. We have thus added 20·6% of this cumulate to the composition of the La Picada parent magmas using olivine (Fo_{86}) and plagioclase (An_{88} for the High-MgO, An_{92} for the Low-MgO, An_{90} for PIC50) core compositions in order to reach the composition of a liquid in equilibrium with olivine only. Two percent of olivine (Fo_{88} from Draper & Johnston, 1992) were then added to obtain the composition of near primary magmas with MgO contents ranging from 10·68 wt % to 11·73 wt % appropriate for the use of the Lee *et al.* (2009) geothermobarometer (Table 7). Their H_2O content (0·9 to 2·0 wt %) was calculated using results obtained with the Waters & Lange (2015) hygrometer on the basalts and taking into account the added cumulates (Table 7). They represent minimum values if the basaltic parent magmas reached vapor saturation and started degassing at a slightly higher pressure than 0·2 GPa. This correction procedure relies on the hypothesis that the differentiation of the near primary magma to the basaltic parent magma took place in the upper crust as the 1 atm experimental data were used. However, as this part of the differentiation could have taken place close to the Moho, we have tested the same procedure using the experimental dataset of Müntener *et al.* (2001) where the phase equilibria of primary arc magmas were studied at 1·2 GPa, conditions corresponding to the arc lower crust. Adding 16·5% of their B736 cumulate (52·12% olivine + 46·06% cpx + 1·82% opx) to the composition of the PIC50 basalt results in calculated pressure and temperature that are within errors of those deduced with the above procedure. We acknowledge that this procedure represents a significant correction, however, we think that the close compositional similarity between the La Picada samples and the experimental melts provides some robustness to these calculations. The composition of primary magmas in equilibrium with olivine Fo_{90} was then obtained by incremental addition of olivine to the compositions of the near primary magmas using the Lee *et al.* (2009) algorithm. Their MgO content ranges from 12·37 to 13·02 wt % (Table 7), they are thus close to picritic compositions. Temperatures (1321°C to 1341°C) and pressures (1·2 to 1·4 GPa) calculated with the Lee *et al.* (2009) geothermobarometer overlap within uncertainties for the different samples (± 50°C, ± 0·2GPa) (Table 7). Temperatures and pressures obtained with equations 13 (1320°C to 1337°C), 14 (1315°C to 1329°C) and 42 (1·2 to 1·4 GPa) of Putirka (2008) agree within errors (± 51/71°C, ± 0·3GPa) with those derived from the Lee *et al.* (2009) geothermobarometer (Table 7). These *P*–*T* conditions are higher than the dry peridotite solidus of Hirschmann (2000), suggesting that adiabatic decompression melting could have taken place (Fig. 17a). However this does not preclude flux melting, as the basaltic parent magmas at La Picada are clearly enriched in slab-derived components compared to MORB (Fig. 11). *P* and *T* obtained for La Picada overlap with those calculated by Watt *et al.* (2013) for volcanic centers (Hornopiren, Apagado, Palena, South Minchinmavida) located further south in the Andean arc, using the composition of olivine-hosted melt inclusions corrected for post entrapment crystallization and fractionation (Fig. 17a).

Table 7: Pressure and temperature of last equilibration in the mantle

	Type Samples	High-MgO PIC04 05 06	High-MgO PIC50	Low-MgO PIC30 31
Composition of the Calculated near primary magmas used in the Lee et al. (2009) geothermobarometer	SiO2 TiO2 Al2O3 FeOt MnO MgO CaO Na2O K2O P2O5 H2O Total	49·41 0·67 16·82 8·47 0·15 11·62 9·33 2·19 0·39 0·09 0·86 100	48·37 0·65 16·98 8·37 0·14 11·73 10·25 2·05 0·23 0·08 1·16 100	47·64 0·74 17·50 8·56 0·15 10·68 10·34 1·98 0·34 0·10 1·96 100
Composition of the primary magmas calculated with the Lee et al. (2009) algorithm	SiO2 TiO2 Al2O3 FeOt MnO MgO CaO Na2O K2O H2O Total	49·29 0·66 16·50 8·51 0·15 12·37 9·16 2·14 0·38 0·85 100	48·15 0·63 16·41 8·44 0·13 13·02 9·91 1·98 0·22 1·12 100	47·32 0·70 16·58 8·67 0·15 12·73 9·80 1·87 0·32 1·86 100
Putirka (2008) Eq.14 Putirka (2008) Eq. 42	T ± 51 °C P ± 0·3 GPa	1319 1·2	1329 1·4	1315 1·4
Putirka (2008) Eq.13 Putirka (2008) Eq. 42	T ± 71 °C P ± 0·3 GPa	1320 1·2	1337 1·4	1329 1·4
Geothermobarometer Lee et al. (2009)	T ± 50 °C P ± 0·2 GPa	1323 1·2	1341 1·4	1321 1·4
Mantle melting High Ti Kelley et al. (2010)	F (± 0·03) CH2O (± 0·10%)	0·22 0·2	0·19 0·2	0·16 0·3
Mantle melting Constant Ti Kelley et al. (2010)	F (± 0·03) CH2O (± 0·10%)	0·17 0·2	0·18 0·2	0·15 0·3

For the High- and Low-MgO samples, the composition of the basalts used in the calculations is the average composition of the samples given in the second row. In order to use the Lee *et al.* (2009) geothermobarometer, the composition of the near primary magmas was first calculated by taking into account fractionation of olivine+plagioclase and then of olivine alone. The H_2O content of the near primary magmas was recalculated considering H_2O as an incompatible component and an initial H_2O content of 2·5 wt % for the Low-MgO basalt, 1·5 wt % for PIC50 and 1·1 wt % for the High-MgO basalt. The composition of the primary magmas, in equilibrium with olivine Fo_{90}, was calculated with the Lee *et al.* (2009) algorithm by incremental addition of olivine only. The temperature and pressure of last equilibration in the mantle were calculated with the Lee *et al.* (2009) and Putirka (2008) geothermobarometers. The amount of mantle partial melting (F) and the H_2O content of the mantle source (CH_2O) were calculated with the procedure of Kelley *et al.* (2010) for high (calculated from TiO_2/Y) and low (constant 0·133 wt %) TiO_2 content in the mantle source. See text for explanation.

The extent of mantle melting (F) and the H_2O content of the mantle source (C^0_{H2O}) can be constrained with a batch melting equation including the TiO_2 content of the primary magmas (C^l_{TiO2}) and estimations of D_{TiO2} (0·04: Kelley *et al.*, 2006) and C^0_{TiO2} (TiO_2 concentration of the mantle source) following the methodology proposed by Kelley *et al.* (2006) and Kelley *et al.* (2010) $\left(F = \frac{\left(C^0_{TiO2} / C^l_{TiO2} - D_{TiO2}\right)}{(1-D_{TiO2})}\right)$. This approach is based on the recognition that, as a 'conservative' element (Pearce & Peate, 1995), TiO_2 in the arc melts is solely contributed by the mantle source and is immobile in the slab component (Kelley *et al.*, 2010). The main unknown is C^0_{TiO2}. It was estimated in two ways. Firstly, we considered a constant TiO_2 content of 0·133 wt % (Salters & Stracke, 2004). Secondly, we followed the procedure of Kelley *et al.* (2006) that uses the TiO_2/Y of MORB. Because these two elements have similar partition coefficients during mantle melting beneath ridges, this ratio shows limited variation in MORB (0·04–0·05: Kelley *et al.*, 2006) and Kelley *et al.* (2006) considered that higher TiO_2/Y in enriched mantle sources is solely due to enrichment in TiO_2 thus enabling the calculation of C^0_{TiO2} $\left(C^0_{TiO2} = \frac{\left(\frac{TiO2}{Y}\right)sample}{\left(\frac{TiO2}{Y}\right)MORB} C^{DMM}_{TiO2}$ with $\left(\frac{TiO2}{Y}\right)$in MORB $=$ 0·04 and $C^{DMM}_{TiO2} = 0·133\right)$. The extent of melting (F) can then be used in the batch melting equation to derive the H_2O content of the mantle source knowing the H_2O content of the primary magmas and D_{H2O} (0·01: Kelley *et al.*, 2006). F values derived with a constant TiO_2 (0·15 to 0·18 : Table 7) are not significantly lower than those derived with the calculated TiO_2 (0·16 to 0·22). The F values of the different samples overlap

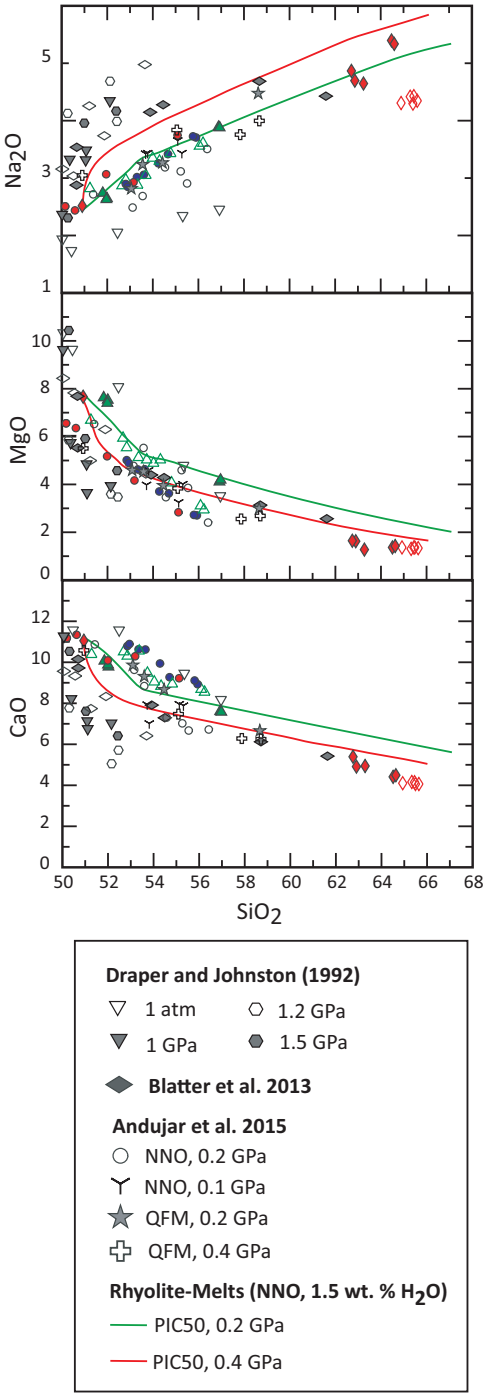

Fig. 16. Comparison of the La Picada trends with the experimental melts of Draper & Johnston (1992), Blatter *et al.* (2013) and Andújar *et al.* (2015) and with the simulations of Rhyolite-MELTS v.1.2.0 (Ghiorso & Gualda, 2015; Gualda *et al.*, 2012) for the basalt PIC50. Analyses recalculated to 100% on a volatile free basis with total Fe as FeO_t.

within errors (± 0·03) (Kelley *et al.*, 2010) (Table 7, Fig. 17b). However, their restricted range combined with the variable $(La/Yb)_N$ ratios (Fig. 11d) point to a possible variation of the extent of mantle partial melting among the samples.

Given the uncertainty on C^0_{H2O} (± 0·10 %) (Kelley *et al.*, 2010), the H_2O content of the mantle source seems to overlap for the different samples of La Picada (0·2 to 0·3 wt % H_2O for the constant and calculated C^0_{TiO2} : Table 7, Fig. 17b). Our results agree with those obtained by Watt *et al.* (2013) for the SVZ (C^0_{H2O} = 0·2–0·6 wt % H_2O) and by Portnyagin *et al.* (2007) for the Kamchatkan arc magmas (C^0_{H2O} = 0·1–0·4 wt % H_2O). Estimates of slab–surface temperatures with Ce and K geothermometry (Cooper *et al.*, 2012; Plank *et al.*, 2009) range from 791 to 920°C (Table 8) and are above the wet-sediment solidus (700°C at about 3 GPa for a pelitic sediment (Hermann & Spandler, 2008); 750°C for a basaltic composition (Lambert & Wyllie, 1972)) suggesting a melt-dominated flux in agreement with trace element data (low Ba/Th; Fig. 11b). A similar temperature (870°C) was obtained by Watt *et al.* (2013) for the Hornopiren–Apagado–Palena–South Minchinmavida rear arc volcanoes.

We currently have no precise constraints on where the differentiation from the primary magmas to the basaltic parent magmas took place. Nonetheless, we note that given their calculated MgO (12·37 to 13·02 wt %) and H_2O (1 to 2 wt %, Table 7) contents, these primary magmas could have fractionated close to the boundary between the lower and upper crust according to Putirka (2017) (their Fig. 3). Moreover, as garnet replaces plagioclase at high pressure and incorporates HREE and Y but not Sr (e.g. Chapman *et al.*, 2015), the low La_N/Yb_N (1·47 to 2·49, Table 1) and Sr/Y (18 to 27, Table 1) ratios of the basaltic parent magmas do not support high pressure fractionation. The occurrence of picritic lavas at the surface of Apagado (Watt *et al.*, 2013) corroborates this hypothesis and even indicates that these highly magnesian magmas can eventually ascend to the upper crust without differentiation. However, given their high density, their fractionation at deeper levels cannot be completely ruled out.

The combination of all geothermobarometric data can be used to draw a schematic sketch of the subduction zone under La Picada, illustrating the estimated location of sub-arc magmatic processes that determine the composition of the magmas (Fig. 18).

Magma differentiation processes

A striking characteristic of the La Picada trends is the occurrence of a Daly Gap. In the following we discuss first the differentiation processes that produced the geochemical variability from basalts to basaltic andesites and then the possible causes of this Daly Gap. As shown in Fig. 16, the La Picada trend overlaps with experimental melts and trends calculated with Rhyolite-MELTS (Ghiorso & Gualda, 2015; Gualda *et al.*, 2012) at 0·2 GPa, suggesting that even if some plagioclase accumulation may have occurred and in contrast with the textural complexity of the basaltic andesites (Fig. 4), the whole-rock trend can be considered as representative of a liquid line of descent, a paradox already

Table 8: Estimated slab surface temperature beneath La Picada

	High MgO PIC04 05 06	High MgO PIC50	Low MgO PIC30 31
H_2O in parent magmas (%)	1·1	1·5	2·5
H_2O in primary magmas (%)	0·86	1·17	1·95
Ce in parent magmas (ppm)	12	13	15
Ce in primary magmas (ppm)	10	10	12
K_2O* in parent magmas (%)	0·50	0·29	0·35
K_2O* in primary magmas (%)	0·39	0·23	0·27
$T(H_2O/Ce)$ (°C)†	920	898	862
$T(K_2O/H_2O)$ (°C)†	911	825	791

*Values for total recalculated at 100%.
†Temperature of the slab surface estimated with the Plank *et al.* (2009) geothermometers. The formula for the K_2O/H_2O thermometer is the corrected one proposed by Watt *et al.* (2013) ($K_2O/H_2O = 6 \times 10^5 \exp(0{\cdot}0098T)$).

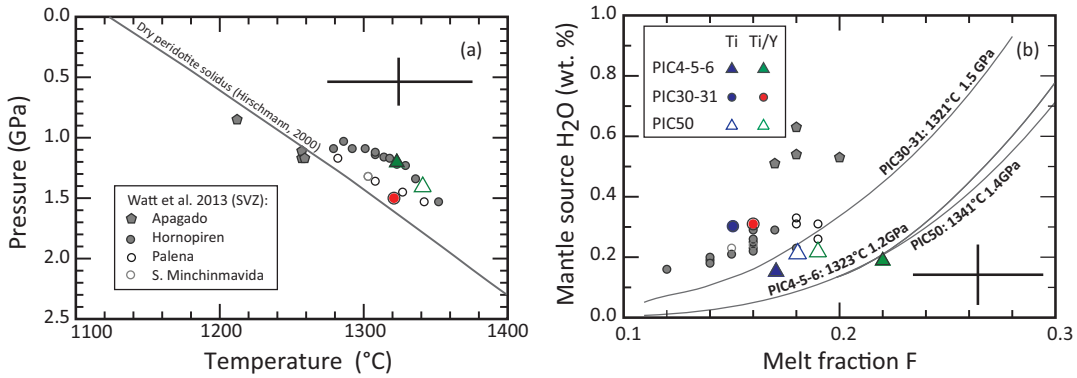

Fig. 17. Estimation of the mantle melting conditions. (a) Pressure and temperature of last equilibration derived with the Lee *et al.* (2009) geothermobarometer for the recalculated primary magmas (same symbols as in Fig. 15) and compared with the dry peridotite solidus of Hirschmann (2000). Errors bars as given by Lee *et al.* (2009). Results from Watt *et al.* (2013) are shown for comparison (see Fig. 1 for the location of Apagado, Hornopiren, Palena an Minchinmavida volcanic centers). (b) Melt fraction (F) *vs* calculated H_2O concentration (in wt %) in the mantle source (C_{H2O}) following (Kelley *et al.*, 2010) for high (calculated from TiO_2/Y) and low TiO_2 (constant 0·133 wt %) contents in the mantle source. The calculated hydrous melting relationships for the different primary magmas are shown as solid curves.

emphasized by Cashman & Blundy (2013). As shown above, clinopyroxenes in equilibrium with the bulk-rock indicate that the differentiation processes took place in the upper crust.

Fractional crystallization versus mixing

Magma mixing and fractional crystallization are the most plausible processes that could produce the chemical diversity between the basalts and the basaltic andesites. It is possible that some contamination occurred in the main magma storage region as gabbroic fragments such as sample PIC11 dated at 9 Ma, have locally been observed. However, these gabbros have overlapping compositions with the La Picada lavas for most major and trace elements (Supplementary Data Fig. S6). Consequently, their assimilation, if it indeed occurred, has probably not significantly affected the composition of the lavas. Isotopic data are not available for the La Picada samples, but here too the gabbroic fragments and the lavas are likely to have overlapping isotopic ratios (Dungan & Davidson, 2004).

Discrimination between mixing and fractional crystallization is hampered by the restricted compositional range from basalt to basaltic andesite (about 5 wt % SiO_2) as curved trends produced by fractional crystallization are usually developed within a much larger range. A potential mixing process has been tested with samples PIC43 (51·27 wt % SiO_2) and PIC44 (56·23 wt % SiO_2), representing respectively the mafic and silicic endmembers, whereas PIC13 (53·72 wt % SiO_2) was considered as possibly resulting from the mixing between these two endmembers. These three samples were chosen because they are aligned in most variation diagrams. The mixing process was tested with the Fourcade & Allègre (1981) method:

$$X = \frac{C_{int} - C_a}{C_b - C_a}$$

where X is the fraction of the mafic endmember, C_a and C_b are respectively the composition of the silicic and mafic endmembers and C_{int} is the composition of the mixed facies. If a mixing process did occur, X should have a value between 0 and 1 and should be the same for all major and trace elements. In the case of the

Table 9: Results of least squares regression modelling

	STEP1			STEP2		
	L0 = PIC43	L1 = PIC34	L1 calculated	L0 = PIC34	L1 = PIC44	L1 calculated
SiO_2	51·27	54·81	54·80	54·81	56·23	56·22
TiO_2	0·96	1·11	1·04	1·11	0·98	1·13
Al_2O_3	18·14	18·43	18·43	18·43	19·20	19·20
FeOt	9·01	8·10	8·11	8·10	7·39	7·37
MnO	0·16	0·15	0·17	0·15	0·13	0·14
MgO	6·64	4·02	4·03	4·02	2·89	2·93
CaO	10·37	8·93	8·95	8·93	8·53	8·54
Na_2O	2·82	3·43	3·62	3·43	3·61	3·74
K_2O	0·45	0·78	0·66	0·78	0·85	0·91
P_2O_5	0·18	0·24	0·27	0·24	0·17	0·28
Phase compositions and proportions (weight %) in the subtracted cumulates.						
Plag	An_{80}	49·7		An_{65}	41·6	
Ol	Fo_{78}	19·9		-		
Cpx	Mg#78	24·0		Mg#72	28·8	
Opx	–			Mg#74	21·9	
Usp*	$Mgt_{72}Usp_{28}$	6·4		$Mgt_{72}Usp_{28}$	7·7	
Σr^2	0·026			0·041		
F†	0·67			0·85		
F total	0·57					
(1-F) total	0·43					

*Composition of a spinel calculated with Rhyolite-Melt (PIC43, NNO, 2 wt % H_2O, T = 1035°C).
†Proportion of residual liquid calculated at each step.
At step 1, plagioclase as well as olivine compositions are from PIC43 and clinopyroxene composition is from PIC36. At step2, plagioclase and orthopyroxene compositions are from PIC 34 whereas clinopyroxene composition is from PIC44.

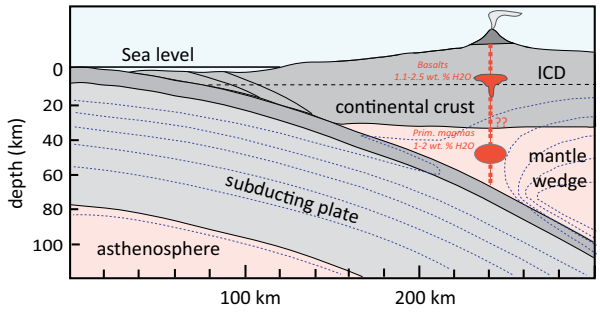

Fig. 18. Schematic sketch of the subduction geometry beneath La Picada illustrating the estimated depth of last equilibration of the primary magma and the location of the main magma storage region. Depth of the intracrustal discontinuity (ICD) separating the upper and lower continental crust from Tassara *et al.* (2006), Moho depth, volcano–trench distance and volcano–slab distance from Syracuse & Abers (2006) (data for Osorno), schematic mantle isotherms (blue dotted lines) from Wada & Wang (2009). Question marks indicate the possible location of differentiation from the primary magmas to the basaltic parent magmas close to the Moho. Scale of the volcano is exaggerated for graphic purposes.

selected samples, Fig. 19a, b shows that most elements plot on the same line in the $C_{int} - C_a$ vs $C_b - C_a$ diagram with a plausible value of 0·63 for X. However, several elements (Rb, Zr, Cu, Ni, Sr, Ba, Ce, Pb, Co, Sc, Ga, Y, SiO_2) do not plot on the same line indicating that a mixing process cannot take into account the complete dataset. If we consider the full differentiation trend from the basalts to the dacites, mixing between a dacite and a basalt to produce a basaltic andesitic composition appears plausible as a few samples plot slightly out of the curved trend shown in the Zr vs Ni diagram (Supplementary Data Fig. S9). However, here too, we note that a mixing process fails to predict all the major and trace element data (Fig. 19c, d). As mentioned above, the larger scatter observed in the Rb vs Ni, La vs Ni and Ba vs Ni diagrams (Supplementary Data Fig. S9) is interpreted as resulting from parent magmas with slightly variable incompatible elements ratios among the La Picada samples (Fig. 11). This could be due to variable mantle source composition (variable contribution of the slab component ?) or to slightly variable extents of mantle partial melting.

Fractional crystallization is supported by several observations. In variation diagrams using two incompatible elements, Ta and Rb as well as Ta and Th (Fig. 20a, b), samples are slightly scattered but define linear trends passing through the origin. In log (Ni)-log (Rb) and log (Y)-log (Rb) diagrams (Fig. 20 c, d), samples are also slightly scattered, but define linear trends in agreement with the Rayleigh distillation law. Finally, in Zr vs Ni and Zr vs Cr diagrams (Supplementary Data Fig. S9), if the dyke 1 dacites are included, samples define a curved trend with a rapid depletion in Ni and Cr. On the other hand, the experimental melts of Draper & Johnston (1992) at 1 atm overlap with the La Picada trend providing additional support for a fractional crystallization process.

Modelling of the fractional crystallization process

The fractional crystallization process was modelled in two steps, using the least square regression method on basalts and basaltic andesites. Subtraction of a

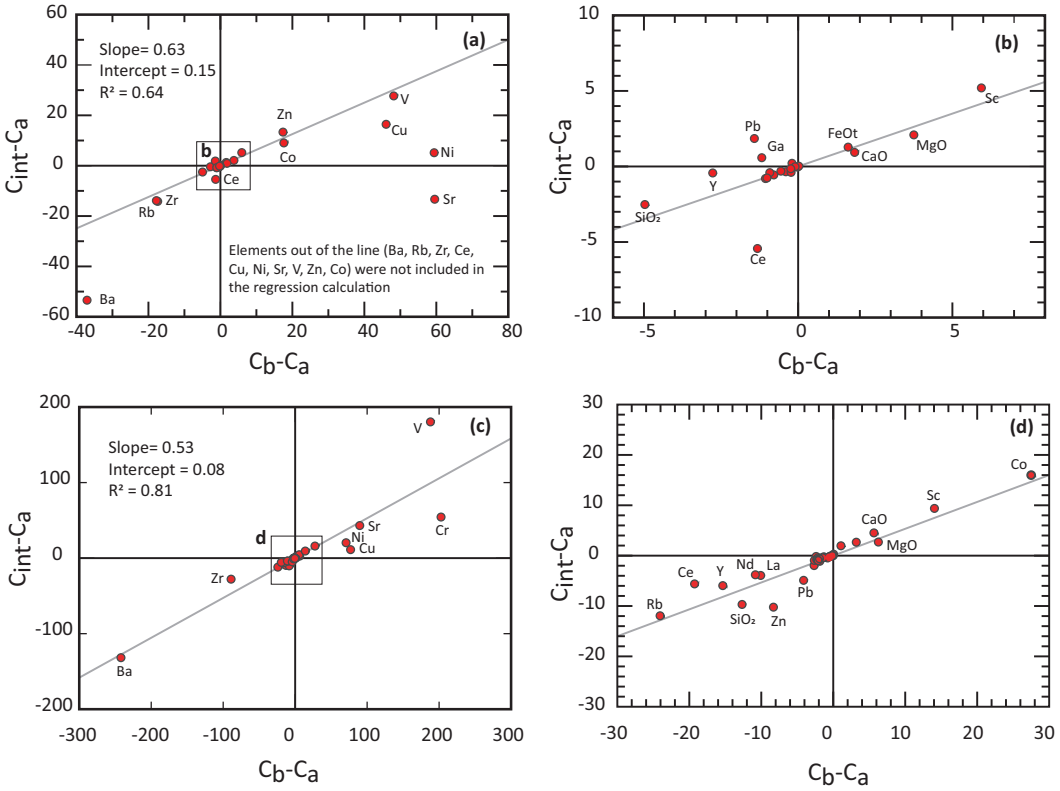

Fig. 19. Test of the mixing process, following the method of Fourcade & Allègre (1981), where C_b, C_a, C_{int} are the concentrations in the mafic, felsic and mixed components. The hypothetical proportion of the mafic end-member (x) in the mixing process is given by the slope of the regression line. (a, b) PIC43, PIC44 and PIC13 are respectively the mafic, acid and intermediate facies. (c, d) PIC04, PIC51 and PIC34 are respectively the mafic, acid and intermediate facies.

gabbroic cumulate from the basaltic parent magma (PIC43) drives the liquid to the composition of a basaltic andesite (PIC34) after 33% fractionation (Table 9). In a second step, separation of a gabbronoritic cumulate produces a residual liquid with the composition of the most evolved basaltic andesite (PIC44) after 15% fractionation. The total fractionation is 43%.

Results from the least square regression model, i.e. fraction of residual liquid and proportions of phases in the cumulates at each step, can be tested using the trace element composition and the calculated bulk partition coefficients in the Rayleigh distillation law :

$$C_L = C_0 \cdot F^{(D-1)}$$

where C_0 and C_L are, respectively, the concentration of the trace element in the parent magma and in the residual liquid, F is the fraction of residual liquid and D is the bulk partition coefficient of the trace element; $D = \Sigma X_i \cdot D_i$ where X_i is the mass fraction of a given mineral in the cumulates and D_i is the partition coefficient of trace element i between this mineral and the liquid. Partition coefficients that were used in this test are given in Table 10. The calculated trace element composition of the residual liquids (Table 11) compares very well with the observed ones, especially for transition elements that are compatible during differentiation. The REE are not well reproduced in the second step as the calculated contents are higher than the observed ones. Samples PIC43 and PIC34 selected in the first step have higher REE contents than most other samples of the Int-MgO trend, including the most evolved sample (PIC44). For example, PIC43 (51·27 wt % SiO_2) has 20·1 ppm Ce compared to 13·2 ppm in sample PIC09 that has a comparable SiO_2 content (52·68 wt % SiO_2). If 13 ppm of Ce are considered in the parent magma at step 1, the calculated residual liquid has 19 ppm Ce; using this value as the starting composition at step 2, the calculated residual liquid has 22 ppm Ce that closely matches the 21 ppm Ce in PIC44.

Origin of the dacites and of the Daly Gap

As previously mentioned, two groups of dacites displaying similar mineralogy (few macrocrysts of plagioclase, orthopyroxene and clinopyroxene in a glassy matrix; Fig. 4), have been distinguished based on their trace elements content. In Harker diagrams with HFSE (Zr, Hf, Nb, Ta, Th, U, Y, TR) and LILE (Rb, Ba, Cs), dyke 2 dacites plot above the main trend. However, both groups of dacites can be extrapolated from the basalts-basaltic andesites trend for major and transition

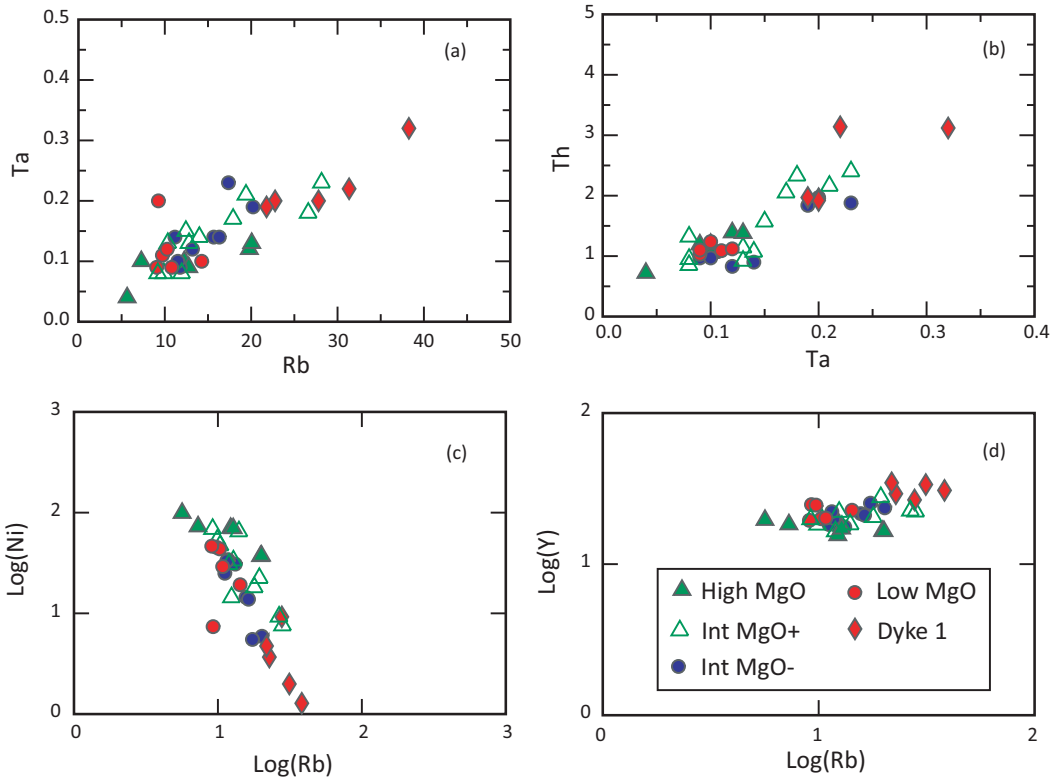

Fig. 20. Test of the fractional crystallization process in diagrams with two incompatible elements (a) Ta vs Rb and (b) Th vs Ta and in bi-logarithmic diagrams (c) Log (Ni) vs Log (Rb) and (d) Log (Y) vs Log (Rb) (note that dacites from dyke 2 and sample PIC14-15 are not shown).

elements (Sc, Cr, V, Cr, Ni, Co, Zn), as well as for Ga. When pairs of incompatible elements are plotted, dyke 1 dacites are aligned with the basalts and basaltic andesites (Fig. 20a, b) whereas dyke 2 dacites define a distinct group except for Th and Rb (Fig. 9). Dyke 2 dacites are indeed two times more enriched than dyke 1 dacites in both Rb and Th, resulting in a constant Rb/Th ratio in all samples from La Picada. The incompatible trace elements composition thus indicate that dyke 1 dacites could be produced by fractional crystallization from the basalts of La Picada, but not dyke 2 dacites. As the dacites from the nearby Calbuco and Osorno volcanoes are compositionally similar to the dyke 1 dacites (Figs 8 and 9), in the current state of knowledge, the dyke 2 dacites cannot be linked to these volcanoes. Lopez-Escobar *et al.* (1995) reported that some mafic facies belonging to small volcanic centers located east of La Picada, Osorno and Calbuco on the Liquiñe–Ofqui Fault zone and referred to as the Minor Eruptive Centers (MEC) are characterized by higher Ba, Sr, Zr, Nb than the major volcanoes of this area (Supplementary Data Fig. S6). It is thus possible that the dyke 2 dacites could be correlated with these mafic facies.

The initial recognition by Bunsen (1851) and Daly (1914) of a compositional Daly Gap giving rise to bimodal mafic–silicic suites was later confirmed in many calc-alkaline, alkaline and tholeiitic magmatic suites and more recently, Reubi & Blundy (2009) pointed out that in arc magmas, melt inclusions indeed display a bimodal distribution of composition with a significantly low amount of andesitic melts. Several processes, not mutually exclusive, have been proposed to predict the occurrence of a Daly Gap: partial melting of country rocks induced by the emplacement of mafic magmas and producing the silicic compositions (e.g. Chayes, 1963); a non uniform compositional distribution of differentiated melts during lower crustal differentiation (Melekhova *et al.*, 2013); bimodality of melts ascending from the lower crust (Reubi & Blundy, 2009); rapid variation in the liquid composition for small temperature decrease, resulting in a small amount of intermediate liquids (Grove & Donnelly-Nolan, 1986); the existence of an immiscibility field along the liquid line of descent (e.g. Charlier & Grove, 2012); and finally a physical control that inihibits the eruption of intermediate compositions (e.g. Brophy, 1991). In the following, we will successively discuss the adequacy of these processes at La Picada.

The dyke 1 dacites and the glass pockets analysed in the basalts and basaltic andesites have overlapping major element composition (Supplementary Data Fig. S6). Moreover, the dyke 1 dacites are aligned with the basalt and basaltic andesite trend passing through the origin in X–Y plots using two incompatible elements and they define the end point of a curved trend in the Ni–Zr and Cr–Zr diagrams (Supplementary Data Fig.

Table 10: Partition coefficients for trace element modelling

	Plagioclase	Olivine	Orthopyroxene	Clinopyroxene	Ti-mgt
Sc	0·04 (1)	0·18 (8)	1·29 (7)	4 (13)	1·7 (19)
V	0·03 (2)	0·096 (9)	0·5 (7)	1·4 (14)	15·8 (14)
Co	0·09 (3)	5·2 (7)	2·48 (7)	0·95 (7)	7·4 (20)
Zn	0·17 (4)	1·8 (10)	2·6 (11)	0·25 (15)	15·5 (4)
Rb	0·01 (3)	0·01 (10)	0·01 (12)	0·01 (16)	0·01 (4)
Sr	1·7/2·36 (5)	0·0005 (7)	0·0021 (7)	0·16 (17)	0·01 (4)
Ba	0·24/0·31 (3)	0·004 (10)	0·01 (11)	0·0058 (17)	0·1 (4)
Ce	0·048/0·045 (6)	0·0001 (10)	0·01 (11)	0·22/0·19 (18)	0·02 (21)
Eu	0·226 (7)	0·004 (10)	0·06 (11)	0·72 (18)	0·02 (21)
Sm	0·024/0·020 (6)	0·003 (10)	0·05 (11)	0·64 (18)	0·02 (21)
Yb	0·003/0·002 (6)	0·049 (10)	0·23 (11)	0·70/0·76 (18)	0·02 (21)

(1) Aigner-Torres *et al.* (2007); (2) Dunn & Sen (1994); (3) Bédard (2006); (4) Ewart & Griffin (1994); (5) Blundy & Wood (1991); (6) Blundy & Wood (2003) (Lattice Strain Model (LSM) with D_0 from Aigner-Torres et al. (2007); (7) Laubier *et al.* (2014); (8) Beattie (1994); (9) Gaetani & Grove (1997); (10) Bédard (2005) use of D_0, $E3^+$ and r_0 in the LSM except for Zn, Rb, Ba for which the empirical regressions were used; (11) Bédard (2007) LSM for the REE, empirical regressions for the other elements; (12) Bacon & Druitt (1988); (13) Gallahan & Nielsen (1992); (14) Toplis & Corgne (2002); (15) Adam & Green (2006); (16) Bédard (2014); (17) Hauri et al. (1994); (18) Wood & Blundy (1997) LSM; (19) Luhr & Carmichael (1980); (20) Dostal *et al.* (1983); (21) Lemarchand *et al.* (1987); X/X, values used respectively for Step1 and Step2.

Table 11: Test of the least squares model with trace elements

	Step1				Step 2			
El	L0 = PIC43	L1 = PIC34	D bulk	L1 calculated	L0 = PIC34	L1 = PIC44	D bulk	L1 calculated
Sc	32	29	1·12	31	29	26	1·59	26
V	251	233	1·39	215	233	203	1·74	207
Co	37	24	1·78	27	24	19	1·42	22
Zn	87	74	1·50	71	74	69	1·90	64
Rb	9·19	19	0·01	14	19	27	0·01	23
Sr	436	396	0·88	457	396	377	1·03	395
Ba	186	252	0·13	266	252	223	0·14	290
Ce	20	28	0·08	29	28	21	0·08	32
Eu	1·05	1·25	0·29	1·4	1·25	1·05	0·32	1·40
Sm	3·11	4·21	0·17	4·4	4·21	3·33	0·21	4·78
Yb	1·87	2·71	0·18	2·6	2·71	2·17	0·27	3·05

S9). These observations indicate that the composition of the dyke 1 dacites can be predicted by fractional crystallization from the basaltic andesites and do not support their origin by partial melting of the crust. As already mentioned, there is no indication that this fractionation process occurred in the lower crust because the Na_2O and K_2O content of the dyke 1 dacites is lower than the experimental high pressure trends (e.g. Draper & Johnston, 1992). Moreover, the macrocryst compositions show no sign of high pressure fractionation (Fig. 13). This implies that the Daly Gap was produced during upper crustal differentiation.

A small amount of intermediate liquids produced during fractionation of assemblages having a nearly flat liquidus slope in temperature–composition space, such as the opx–cpx–plag-magnetite assemblage of step 2 at La Picada (Table 9), was initially proposed by Grove & Donnelly-Nolan (1986) to explain the Daly Gap and is indeed plausible here. Two lines of evidence indicate that fractionation of the La Picada parent magma can produce andesitic melts. Firstly, one of the glass pockets analysed in the basalt PIC50, as well as the calculated composition of the basaltic andesite PIC33 matrix, is andesitic (Supplementary Data Fig. S6). Secondly, in the experimental datasets of Blatter *et al.* (2013) and Andújar *et al.* (2015) performed on starting compositions that are relevant here, two melts are andesitic (Fig. 16).

Textural, mineralogical and geochemical data suggest that a physical control combining critical crystallinity and melt segregation might have produced the observed Daly Gap. The dacites, that were only observed in dykes, are very poor in macrocrysts of minor clinopyroxene and dominant plagioclase, with no or rare inclusions and only slight zoning (Fig. 4d). On the contrary, the basaltic andesites are very rich in crystals dominated by plagioclase, but displaying complex zoning and inclusions patterns (Fig. 4b). The fractional crystallization model indicates that the liquid reaches the composition of the most evolved basaltic andesite when the proportion of crystals is 43%. This represents a minimum value as the parent magma may have been slightly more primitive than our least differentiated sample. This result agrees very well with experimental data, as in run 2380 of Blatter *et al.* (2013) where the proportion of crystals is 48% with a differentiation

degree (54·3 wt % SiO_2) similar to the most evolved basaltic andesite (56·9 wt % SiO_2) and a H_2O content (3%) identical to that deduced for the residual liquid of La Picada. Interestingly, the proportion of crystals is 43% in PIC33 (56·96 wt % SiO_2), which corresponds to the value at which crystals start to form a connecting network (critical crystallinity). Marsh (1981) indeed suggested that critical crystallinity is reached when the proportion of crystals is 50–60%, in agreement with the rigid percolation threshold of about 55% crystals later proposed by Vigneresse *et al.* (1996) for the segregation of felsic magma. Moreover, Philpotts *et al.* (1998) showed that when the proportion of plagioclase crystals is high, critical crystallinity is reached at about 35% crystals. We thus suggest that when the composition of the magma (bulk-rock) reached the composition of the most evolved basaltic andesite, the proportion of crystals was high enough for the magma to behave like a solid, precluding its eruption and thus producing the Daly Gap. As already mentioned, the glass pockets represent melt compositions that are slightly more differentiated than the interstitial melt (matrix) that was initially present in the crystal mush because of microlite crystallization during final magma ascent. The calculated matrix of the most evolved basaltic andesite PIC33 is indeed andesitic compared to the dacitic glass pockets analysed in the basaltic andesites PIC07, PIC10, PIC14. However, because the magmas having a composition corresponding to the critical crystallinity threshold did not erupt and were probably slightly more differentiated than the most evolved basaltic andesite that we sampled, we suggest that their interstitial melts were probably close to a dacitic composition similar to the glass pockets. As these overlap in composition with the dacitic dykes (Supplementary Data Fig. S6), we further propose that the interstitial melt (or a fraction of it) was extracted from the crystal mush, collected and emplaced as dykes. Such a situation is similar to what has been described for crystal-rich dacitic ignimbrites and their associated crystal-poor rhyolitic facies (e.g. Bachmann *et al.*, 2002; Cashman & Blundy, 2000) except that at La Picada, the volume of extracted melt was probably much lower (only two small dacitic domes have been mapped on the nearby Osorno volcano). Consequently, according to this hypothesis, the observed compositional gap would simply result from the subtraction of the crystal load from the basaltic andesitic magma and will be more visible for elements that are enriched in the crystals. Separation of a crystal matrix rich in plagioclase from the basaltic andesitic magma produces a significant compositional gap in SiO_2, CaO, Al_2O_3 and Na_2O (Supplementary Data Fig. S10). Similarly, because the crystal matrix contains Ti-magnetite, the gap is also significant in TiO_2 and V. Contrarily, there is no Daly Gap for Ni because its content is close to zero when the magma reaches the composition of the basaltic andesite. For incompatible elements such as the REE, there is a small gap with a slightly higher content in the dacitic melts because their concentration in the crystals is very low. Using a quantitative approach, Bachmann & Bergantz (2004) proposed that in a crystal mush where critical crystallinity has been reached, extraction from the crystal mush by upward percolation of a buoyant dacitic melt can be produced by a combination of three mechanisms: compaction if the crystal mush was thick enough (Holness *et al.*, 2017; McKenzie, 2011); micro-settling (melt expulsion resulting from textural adjustments of the grains); and hindered settling (settling in a dense suspension). However, Holness (2018) recently questioned the viability of these melt segregation processes. Gas-driven filter pressing and filter pressing can also potentially segregate the melt from the crystal network. Gas-driven filter pressing occurs because of the increasing pressure due to second boiling and the release of this pressure by extraction of the melt from the mush (Sisson & Bacon, 1999). As shown above, the pressure of volatile saturation can be estimated at about 0.25 to 0.3 GPa, suggesting that the magmas were volatile saturated in the main storage region. Gas-driven filter pressing is thus plausible. Filter pressing happens when the magma is squeezed under an external force, possibly resulting from a modification in regional stress. Control by regional stress is possible in the area of La Picada as Cembrano & Lara (2009) showed that in the NE–SW striking chain of Osorno (and nearby La Picada–Puntiagudo–Cordon Cenizos), the morphology and spatial distribution of the volcanoes is partly controlled by transpressional tectonics that dominates between 34° to 46° S with a major transpressional dextral strike-slip structure, the 1200 km long Liquiñe–Ofqui Fault zone stretching from 38° to 47°S (Cembrano & Lara, 2009).

CONCLUSIONS

Fractional crystallization at low pressure is the dominant process that produced the differentiation from the parent tholeiitic basalts to the dacites at La Picada. We argue that the conspicuous compositional (Daly) gap that separates the most evolved basaltic andesites from the dacites was produced because critical crystallinity was reached at the composition of the most evolved basaltic andesites, preventing eruption of more differentiated lavas. The dacitic interstitial melt produced by differentiation from the basaltic andesites was then segregated from the crystal mush and emplaced as dykes that possibly evacuated the dacites as small domes. Moreover, it seems that the basalts and basaltic andesites mainly transported their own crystals. The composition of the recalculated primary magmas indicates last equilibration in the upper mantle and above the dry peridotite solidus suggesting that a component of decompression melting could have taken place. However, because the basalts are enriched in slab components and H_2O (1·1–2·5 wt % H_2O in the basalts, about 1–2 wt % H_2O in the calculated primary magmas) compared to N-MORB, wet melting is highly likely. As no trace of high pressure fractionation was detected in mineral

composition and whole-rock geochemistry, it can be concluded that the basaltic parent magmas differentiated at a depth apparently corresponding to both the site of an intracrustal discontinuity and the level of fluid saturation. There is currently no direct constraint on the depth of differentiation from the primary (12·3 to 13·02 wt % MgO) to the parental magmas, but as the former are not strictly picritic they could have differentiated in the lower or upper crust. As already pointed out by Hickey-Vargas *et al.* (2016b), the rapid magma ascent was probably facilitated by the presence of the Liquiñe–Ofqui Fault zone. Insights from La Picada thus stress the potential role of crustal structure on arc magma processes.

ACKNOWLEDGEMENTS

We are grateful to Luis Lara (SERNAGEOMIN, Chile) for his support in the organization of the field missions. We thank K. Putirka, S. Erdmann and P. Barbey for constructive and thoughtful reviews of an earlier version of this contribution. Additional and insightful comments as well as editorial handling by G. Wörner also contributed to the quality of the paper.

FUNDING

This work was supported by Fonds National de la Recherche Scientifique CDR 19519719 and University of Liège Crédit classique 12/35 to JVDA as well as FNRS and ULiège fieldtrip grants. ON acknowledges support from an Emmy-Noether grant of the Deutsche Forschungsgemeinschaft (Germany).

SUPPLEMENTARY DATA

Supplementary data are available at *Journal of Petrology* online.

REFERENCES

Adam, J. & Green, T. (2006). Trace element partitioning between mica- and amphibole-bearing garnet lherzolite and hydrous basanitic melt: 1. Experimental results and the investigation of controls on partitioning behaviour. *Contributions to Mineralogy and Petrology* **152**, 1–17.

Adam, J., Turner, S. & Rushmer, T. (2016). The genesis of silicic arc magmas in shallow crustal cold zones. *Lithos* **264**, 472–494.

Aigner-Torres, M., Blundy, J., Ulmer, P. & Pettke, T. (2007). Laser ablation ICPMS study of trace element partitioning between plagioclase and basaltic melts: an experimental approach. *Contributions to Mineralogy and Petrology* **153**, 647–667.

Andújar, J., Scaillet, B., Pichavant, M. & Druitt, T. (2015). Differentiation conditions of a basaltic magma from Santorini and its bearing on the production of andesite in arc settings. *Journal of Petrology* **56**, 765–794.

Angermann, D., Klotz, J. & Reigber, C. (1999). Space-geodetic estimation of the Nazca-South America Euler vector. *Earth and Planetary Science Letters* **171**, 329–334.

Annen, C., Blundy, J., Leuthold, J. & Sparks, R. S. J. (2015). Construction and evolution of igneous bodies: towards an integrated perspective of crustal magmatism. *Lithos* **230**, 206–221.

Annen, C., Blundy, J. & Sparks, R. S. J. (2006). The genesis of intermediate and silicic magmas in deep crustal hot zones. *Journal of Petrology* **47**, 505–539.

Assumpção, M., Feng, M., Tassara, A. & Julià, J. (2013). Models of crustal thickness for South America from seismic refraction, receiver functions and surface wave tomography. *Tectonophysics* **609**, 82–96.

Bachmann, O. & Bergantz, G. W. (2004). On the origin of crystal-poor rhyolites: extracted from batholithic crystal mushes. *Journal of Petrology* **45**, 1565–1582.

Bachmann, O., Dungan, M. & Lipman, P. (2002). The Fish Canyon magma body, San Juan volcanic field, Colorado: rejuvenation and eruption of an upper-crustal batholith. *Journal of Petrology* **43**, 1469–1503.

Bacon, C. R. & Druitt, T. H. (1988). Compositional evolution of the zoned calc-alkaline magma chamber of Mount Mazama, Crater Lake, Oregon. *Contributions to Mineralogy and Petrology* **98**, 224–256.

Beattie, P. (1994). Systematics and energetics of trace-element partitioning between olivine and silicate melts: Implications for the nature of mineral/melt partitioning. *Chemical Geology* **117**, 57–71.

Bédard, J. (2005). Partitioning coefficients between olivine and silicate melts. *Lithos* **83**, 394–419.

Bédard, J. (2006). Trace element partitioning in plagioclase feldspar. *Geochimica et Cosmochimica Acta* **70**, 3717–3742.

Bédard, J. (2007). Trace element partitioning coefficients between silicate melts and orthopyroxene: Parameterizations of D variations. *Chemical Geology* **244**, 263–303.

Bédard, J. H. (2014). Parameterizations of calcic clinopyroxene—melt trace element partition coefficients. *Geochemistry, Geophysics, Geosystems* **15**, 303–336.

Biggs, J., Robertson, E. & Cashman, K. V. (2016). The lateral extent of volcanic interactions during unrest and eruption. *Nature Geoscience* **9**, 308–312.

Blatter, D., Sisson, T. & Hankins, W. (2013). Crystallization of oxidized, moderately hydrous arc basalt at mid- to lower-crustal pressures: Implications for andesite genesis. *Contributions to Mineralogy and Petrology* **166**, 861–886.

Blundy, J. & Wood, B. J. (1991). Crystal-chemical controls on the partitioning of Sr and Ba between plagioclase feldspar, silicate melts and hydrothermal solutions. *Geochimica et Cosmochimica Acta* **55**, 193–209.

Blundy, J. & Wood, B. J. (2003). Partitioning of trace elements between crystals and melts. *Earth and Planetary Science Letters* **210**, 383–397.

Bouvet De Maisonneuve, C., Dungan, M. A., Bachmann, O. & Burgisser, A. (2013). Petrological insights into shifts in eruptive styles at volcán Llaima (Chile). *Journal of Petrology* **54**, 393–420.

Brophy, J. (1991). Composition gaps, critical crystallinity and fractional crystallization in orogenic (calc-alkaline) magmatic systems. *Contributions to Mineralogy and Petrology* **109**, 173–182.

Brown, G. (1956). The layered ultrabasic rocks of Rhum, Inner Hebrides. *Philosophical Transactions of the Royal Society of London* **B240**, 1–53.

Bunsen, R. (1851). Uner die processe der vulkanischen gesteinsbildungen islands. *Annalen Der Physik Und Chemie* **83**, 197–272.

Cashman, K. V. & Blundy, J. (2013). Petrological cannibalism: the chemical and textural consequences of incremental

magma body growth. *Contributions to Mineralogy and Petrology* **166**, 703–729.
Cashman, K. V. & Blundy, J. D. (2000). Degassing and crystallization of ascending andesite and dacite. *Philosophical Transactions A: Mathematical, Physical and Engineering Sciences* **358**, 1487–1513.
Cembrano, J., Hervé, F. & Lavenu, A. (1996). The Liquiñe-Ofqui fault zone: a long-lived intra-arc fault zone in southern Chile. *Tectonophysics* **259**, 55–66.
Cembrano, J. & Lara, L. (2009). The link between volcanism and tectonics in the southern volcanic zone of the Chilean Andes: a review. *Tectonophysics* **471**, 96–113.
Chapman, J., Ducea, M., DeCelles, P. & Profeta, L. (2015). Tracking changes in crustal thickness during orogenic evolution with Sr/Y: an example from the North American cordillera. *Geology* **43**, 919–922.
Charlier, B. & Grove, T. (2012). Experiments on liquid immiscibility along tholeiitic liquid lines of descent. *Contributions to Mineralogy and Petrology* **164**, 27–44.
Chayes, F. (1963). Relative abundance of intermediate members of the oceanic basalt-trachyte association. *Journal of Geophysical Research* **68**, 1519–1534.
Chin, E. J., Shimizu, K., Bybee, G. M. & Erdman, M. E. (2018). On the development of the calc-alkaline and tholeiitic magma series: a deep crustal cumulate perspective. *Earth and Planetary Science Letters* **482**, 277–287.
Cooper, L. B., Ruscitto, D. M., Plank, T., Wallace, P. J., Syracuse, E. M. & Manning, C. E. (2012). Global variations in H2O/Ce: 1. Slab surface temperatures beneath volcanic arc. *Geochemistry, Geophysics, Geosystems* **13**.
Costa, F., Scaillet, B. & Pichavant, M. (2004). Petrological and experimental constraints on the pre-eruption conditions of Holocene dacite from volcan San Pedro. *Journal of Petrology* **45**, 855–881.
Daly, R. (1914). *Igneous Rocks and Their Origin*. New York: McGraw Hill.
Davidson, J., Morgan, D., Charlier, B., Harlou, R. & Hora, J. (2007). Tracing magmatic processes and timescales through mineral-scale isotopic data. *Annual Review of Earth and Planetary Sciences* **35**, 273–311.
Deruelle, B., Harmon, R. & Moorbath, S. (1983). Combined Sr–O isotope relationships and petrogenesis of Andean volcanics of South America. *Nature* **302**, 814–816.
Dostal, J., Dupuy, C., Carron, J. P., Le Guen de Kerneizon, M. & Maury, R. C. (1983). Partition coefficients of trace elements-application to volcanic rocks of St-Vincent, West-Indies. *Geochimica et Cosmochimica Acta* **47**, 525–533.
Draper, D. & Johnston, A. (1992). Anhydrous PT phase relations of an Aleutian high-MgO basalt: an investigation of the role of olivine-liquid reaction in the generation of arc high-alumina basalts. *Contributions to Mineralogy and Petrology* **112**, 501–519.
Dungan, M. & Davidson, J. (2004). Partial assimilative recycling of the mafic plutonic roots of arc volcanoes: an example from the Chilean Andes. *Geology* **32**, 773–776.
Dunn, T. & Sen, C. (1994). Mineral/matrix partition-coefficients for orthopyroxene, plagioclase and olivine in basaltic to andesitic systems - a combined analytical and experimental study. *Geochimica et Cosmochimica Acta* **58**, 717–733.
Elliott, T. (2003). Tracers of the slab. In: Eiler, J. (ed.) *Inside the Subduction Factory.* Washington DC: American Geophysical Union, pp. 23–45.
Erdmann, S., Martel, C., Pichavant, M., Bourdier, J.-L., Champallier, R., Komorowski, J.-C. & Cholik, N. (2016). Constraints from phase equilibrium experiments on pre-eruptive storage conditions in mixed magma systems: a case study on crystal-rich basaltic andesites from Mount Merapi, Indonesia. *Journal of Petrology* **57**, 535–560.
Ewart, A. & Griffin, W. (1994). Application of proton-microprobe data to trace-element partitioning in volcanic rocks. *Chemical Geology* **117**, 251–284.
Farner, M. & Lee, C.-T A. (2017). Effects of crustal thickness on magmatic differentiation in subduction zone volcanism: a global study. *Earth and Planetary Science Letters* **470**, 96–107.
Fourcade, S. & Allègre, C. J. (1981). Trace elements behaviour in granite genesis: a case study, the calc-alkaline plutonic association from the Quérigut complex (Pyrénées, France). *Contributions to Mineralogy and Petrology* **76**, 177–195.
Gaetani, G. A. & Grove, T. L. (1997). Partitioning of moderately siderophile elements among olivine, silicate melt and sulfide melt: constraints on core formation in the Earth and Mars. *Geochimica et Cosmochimica Acta* **61**, 1829–1846.
Gallahan, W. & Nielsen, R. (1992). The partitioning of Sc, Y, and the Rare Earth elements between high-Ca pyroxene and natural mafic to intermediate lavas at 1 atmosphere. *Geochimica et Cosmochimica Acta* **56**, 2387–2404.
Ghiorso, M. S. & Gualda, G. (2015). An H_2O-CO_2 mixed fluid saturation model compatible with Rhyolite-melts. *Contributions to Mineralogy and Petrology* **169**, 53–82.
Grove, T. L. & Baker, M. B. (1984). Phase equilibrium controls on the tholeiitic versus calc-alkaline differentiation trends. *Journal of Geophysical Research* **89**, 3253–3274.
Grove, T. L. & Donnelly-Nolan, J. M. (1986). The evolution of young silicic lavas at Medicine Lake volcano by fractionation, assimilation and mixing. *Contributions to Mineralogy and Petrology* **92**, 281–302.
Grove, T. L., Elkins-Tanton, L. T., Parman, S. W., Chatterjee, N., Müntener, O. & Gaetani, G. A. (2003). Fractional crystallization and mantle-melting controls on calc-alkaline differentiation trends. *Contributions to Mineralogy and Petrology* **145**, 515–533.
Grove, T. L., Till, C. B. & Krawczynski, M. J. (2012). The role of H_2O in subduction zone magmatism. *Annual Review of Earth and Planetary Sciences* **40**, 413–439.
Gualda, G., Ghiorso, M. S., Lemons, R. & Carley, T. (2012). Rhyolite-melts: a modified calibration of melts optimized for silica-rich, fluid-bearing magmatic systems. *Journal of Petrology* **53**, 875–890.
Hamada, M. & Fujii, T. (2008). Experimental constraints on the effects of pressure and H_2O on the fractional crystallization of high-Mg island arc basalt. *Contributions to Mineralogy and Petrology* **155**, 767–790.
Hauri, E. H., Wagner, T. P. & Grove, T. L. (1994). Experimental and natural partitioning of Th, U, Pb and other trace elements between garnet, clinopyroxene and basaltic melts. *Chemical Geology* **117**, 149–166.
Hermann, J. & Spandler, C. J. (2008). Sediment melts at sub-arc depths: An experimental study. *Journal of Petrology* **49**, 717–740.
Hickey, R., Gerlach, D. C. & Frey, F. A. (1984). Geochemical variations in volcanic rocks from central-south Chile (33–42°S). In: Harmon, R. and Barreiro, B. (eds) *Andean Magmatism. Chemical and Isotopic Constraints.* Nantwich: Shiva Publishing Limited, Nantwich, pp. 72–95.
Hickey, R. L., Frey, F. A., Gerlach, D. C. & Lopez-Escobar, L. (1986). Multiple sources for basaltic arc rocks from the Southern Volcanic Zone of the Andes (34°-41°S): Trace element and isotopic evidence for contributions from subducting oceanic crust, mantle and continental crust. *Journal of Geophysical Research* **91**, 5963–5983.

Hickey-Vargas, R., Holbik, S., Tormey, D., Frey, F. A. & Moreno Roa, H. (2016). Basaltic rocks from the Andean Southern Volcanic Zone: Insights from the comparison of along-strike and small-scale geochemical variations and their sources. *Lithos* **258–259**, 115–132.

Hickey-Vargas, R., Sun, M. & Holbik, S. (2016). Geochemistry of basalts from small eruptive centers near Villarrica stratovolcano, Chile: Evidence for lithospheric mantle components in continental arc magmas. *Geochimica et Cosmochimica Acta* **185**, 358–382.

Higgins, M., Voos, S. & Vander Auwera, J. (2015). Magmatic processes under Quizapu volcano, Chile, identified from geochemical and textural studies. *Contributions to Mineralogy and Petrology* **170**, 51–67.

Hildreth, W. & Moorbath, S. (1988). Crustal contributions to arc magmatism in the Andes of Central Chile. *Contributions to Mineralogy and Petrology* **98**, 455–489.

Hirschmann, M. (2000). Mantle solidus: experimental constraints and the effects of peridotite composition. *Geochemistry, Geophysics and Geosystems* **1**, 2000GC000070.

Holness, M. (2018). Melt segregation from silicic crystal mushes: A critical appraisal of possible mechanisms and their microstructural record. *Contributions to Mineralogy and Petrology* **173**, 48–64.

Holness, M. B., Vukmanovic, Z. & Mariani, E. (2017). Assessing the role of compaction in the formation of adcumulates: A microstructural perspective. *Journal of Petrology* **58**, 643–673.

Husson, L., Conrad, C. & Faccenna, C. (2012). Plate motions Andean orogeny and volcanism above the South Atlantic convection cell. *Earth and Planetary Science Letters* **317–318**, 126–135.

Irvine, T. & Baragar, W. (1971). A guide to chemical classification of common volcanic rocks. *Canadian Journal of Earth Sciences* **8**, 523–548.

Jacques, G., Hoernle, K., Gill, J., Hauff, F., Wehrmann, H., Garbe-Schönberg, D., van den Bogaard, P., Bindeman, I. & Lara, L. (2013). Across-arc geochemical variations in the Southern Volcanic Zone, Chile (34.5-38.0°S): Constraints on mantle wedge and slab input compositions. *Geochimica et Cosmochimica Acta* **123**, 218–243.

Jarrard, R. (1986). Relations among subduction parameters. *Reviews of Geophysics* **24**, 217–284.

Jerram, D. A. & Martin, V. M. (2008). Understanding crystal populations and their significance through the magma plumbing system. In: Annen, C., Zellmer, G. F. (eds) Dynamics of crustal magma transfer, storage and differentiation. *Geological Society, London, Special Publication* **304**, 133–148.

Kelley, K. A., Plank, T., Grove, T. L., Stolper, E. M., Newman, S. & Hauri, E. H. (2006). Mantle melting as a function of water content beneath back-arc basins. *Journal of Geophysical Research* **111**, B09208.

Kelley, K. A., Plank, T., Newman, S., Stolper, E. M., Grove, T. L., Parman, S. & Hauri, E. H. (2010). Mantle melting as a function of water content beneath the Mariana arc. *Journal of Petrology* **51**, 1711–1738.

Kinzler, R., Grove, T. & Recca, S. (1990). An experimental study on the effect of temperature and composition on the partitioning of nickel between olivine and silicate melt. *Geochimica et Cosmochimica Acta* **54**, 1255–1265.

Kratzmann, D., Carey, S., Scasso, R. & Naranjo, J.-A. (2010). Role of cryptic amphibole crystallization in magma differentiation at Hudson volcano, Southern Volcanic Zone, Chile. *Contributions to Mineralogy and Petrology* **159**, 237–264.

Lambert, I. & Wyllie, P. (1972). Melting of gabbro (quartz eclogite) with excess water to 35 kilobars, with geological implications. *Journal of Geology* **80**, 693–708.

Laubier, M., Grove, T. L. & Langmuir, C. (2014). Trace element mineral/melt partitioning for basaltic and basaltic andesitic melts: An experimental and laser ICP-MS study with application to the oxidation state of mantle source regions. *Earth and Planetary Science Letters* **392**, 265–278.

Lee, C.-T A., Luffi, P., Plank, T., Dalton, H. & Leeman, W. (2009). Constraints on the depths and temperatures of basaltic magma generation on Earth and other terrestrial planets using new thermobarometers for mafic magmas. *Earth and Planetary Science Letters* **279**, 20–33.

Lemarchand, F., Villemant, B. & Calas, G. (1987). Trace element distribution coefficients in alkaline series. *Geochimica et Cosmochimica Acta* **51**, 1071–1081.

Lopez-Escobar, L. (1984). Petrology and chemistry of volcanic rocks of the Southern Andes. In: Harmon, R. and Barreiro, B. (eds.) *Andean Magmatism. Chemical and Isotopic Constraints.* Nantwich: Shiva Publishing Limited.

Lopez-Escobar, L. & Moreno, R. (1994). Geochemical characteristics of the Southern Andes basaltic volcanism associated with the Liquiñe-Ofqui Fault Zone between 39 degrees and 46 degrees S, Chile. *Actas Congreso Geologico Chileno* **7**, 1388–1393.

Lopez-Escobar, L., Parada, M., Hickey-Vargas, R., Frey, F., Kempton, P. & Moreno, H. (1995). Cabulco volcano and minor eruptive centers distributed along the Liquiñe-Ofqui Fault Zone, Chile (41°-42°S): Contrasting origin of andesitic and basaltic magma in the Southern Volcanic Zone of the Andes. *Contributions to Mineralogy and Petrology* **119**, 345–361.

Lopez-Escobar, L., Vergara, M. & Frey, F. A. (1981). Petrology and geochemistry of lavas from Antuco volcano, a basaltic volcano of the Southern Andes (37°–25°S.). *Journal of Volcanology and Geothermal Research* **11**, 329–352.

Lucassen, F., Wiedicke, M. & Franz, G. (2010). Complete recycling of a magmatic arc: Evidence from chemical and isotopic composition of Quaternary trench sediments in Chile (36°–40°S.). *International Journal of Earth Sciences* **99**, 687–701.

Luhr, J. F. & Carmichael, I. S. E. (1980). The Colima volcanic complex, Mexico. I: Post-caldera andesites from volcan Colima. *Contributions to Mineralogy and Petrology* **71**, 343–372.

Mandler, B. E., Donnelly-Nolan, J. M. & Grove, T. L. (2014). Straddling the tholeiitic/calc-alkaline transition: The effects of modest amounts of water on magmatic differentiation at Newberry volcano, Oregon. *Contributions to Mineralogy and Petrology* **168**, 1–25.

Marsh, B. (1981). On the crystallinity, probability of occurrence, and rheology of lava and magma. *Contributions to Mineralogy and Petrology* **78**, 85–98.

McDougall, I. & Harrison, T. (1999). *Geochronology and Thermochronology by the 40Ar/39Ar Method*. Oxford: Oxford University Press.

McKenzie, D. (2011). Compaction and crystallization in magma chambers: towards a model of the Skaergaard intrusion. *Journal of Petrology* **52**, 905–930.

Melekhova, E., Annen, C. & Blundy, J. (2013). Compositional gaps in igneous rock suites controlled by magma system heat and water content. *Nature Geoscience* **6**, 385–390.

Montalbano, S., Namur, O., Schiano, P., Bolle, O. & Vander Auwera, J. (2017). Magma storage conditions and processes at Calbuco volcano (Central Southern Volcanic Zone, Chili). *Goldschmidt Conference*. Paris.

Moreno, H., Lara, L. & Orozco, G. (2010). Geologia del Volcan Osorno, Region De Los Lagos. In: Servicio Nacional de Geología y Mineria (ed.) *Carta Geologica De Chile.* Santiago.

Morris, J., Leeman, W. & Tera, F. (1990). The subducted component in island arc lavas; constraints from B-Be isotopes and Be systematics. *Nature* **344**, 31–36.

Morse, S. A. (1979). Kiglapait geochemistry ii: petrography. *Journal of Petrology* **20**, 591–624.

Müntener, O., Kelemen, P. & Grove, T. (2001). The role of H_2O during crystallization of primitive arc magmas under uppermost mantle conditions and genesis of igneous pyroxenites: An experimental study. *Contributions to Mineralogy and Petrology* **141**, 643–658.

Namur, O., Charlier, B., Toplis, M. J., Higgins, M. D., Hounsell, V., Liégeois, J. P. & Vander Auwera, J. (2011). Differentiation of tholeiitic basalt to A - type granite in the Sept Iles layered intrusion, Canada. *Journal of Petrology* **52**, 487–539.

Namur, O., Humphreys, M. C. S. & Holness, M. B. (2014). Crystallization of interstitial liquid and latent heat buffering in solidifying gabbros: Skaergaard intrusion, Greenland. *Journal of Petrology* **55**, 1389–1427.

Nandedkar, R., Ulmer, P. & Müntener, O. (2014). Fractional crystallization of primitive, hydrous arc magmas: An experimental study at 0.7 GPa. *Contributions to Mineralogy and Petrology* **167**, 1015–1041.

Navez, J. (1995). Détermination d'éléments en traces dans les roches silicatées par ICP-MS. In: Musée Royal de l'Afrique centrale (ed.) Rapport annuel 1993 & 1994. Tervuren (Belgique), 139–147.

Neave, D. & Putirka, K. D. (2017). A new clinopyroxene-liquid barometer and implications for magma storage pressures under icelandic rift zones. *American Mineralogist* **102**, 777–794.

Neave, D. A., Maclennan, J., Hartley, M., Edmonds, M. & Thordarson, T. (2014). Crystal storage and transfer in basaltic systems: The Skuggafjöll eruption, Iceland. *Journal of Petrology* **55**, 2311–2346.

Newman, S. & Lowenstern, J. (2002). Volatilecalc: a silicate melt-H_2O-CO_2 solution model written in visual basic for Excel. *Computers and Geosciences* **28**, 597–604.

Norman, M., Garcia, M. & Pietruszka, A. (2005). Trace-element distribution coefficients for pyroxenes, plagioclase and olivine in evolved tholeiites from the 1955 eruption of Kilauea volcano, Hawaii and petrogenesis of differentiated rift-zone lavas. *American Mineralogist* **90**, 888–899.

Pearce, J. & Peate, D. (1995). Tectonic implications of the composition of volcanic arc magmas. *Annual Reviews of Earth and Planetary Sciences* **23**, 251–285.

Peccerillo, A. & Taylor, S. R. (1976). Geochemistry of Eocene calc-alkaline volcanic rocks from the Kastamonu area, northern Turkey. *Contributions to Mineralogy and Petrology* **58**, 63–81.

Philpotts, A., Shi, J. & Brustman, C. (1998). Role of plagioclase crystal chains in the differentiation of partly crystallized basaltic magma. *Nature* **395**, 343–346.

Plank, T. (2014). The chemical composition of subducting sediments. In: Rudnick, R. (ed.) *Treatise on Geochemistry*, 2nd edn. Oxford: Elsevier, pp. 607–629.

Plank, T., Cooper, L. & Manning, C. (2009). Emerging geothermometers for estimating slab surface temperatures. *Nature Geoscience* **2**, 611.

Plank, T., Kelley, K., Zimmer, M., Hauri, E. & Wallace, P. J. (2013). Why do mafic arc magmas contain $\approx$ 4 wt % water on average? *Earth and Planetary Science Letters* **364**, 168–179.

Plank, T. & Langmuir, C. H. (1988). An evaluation of the global variations in the major element chemistry of arc basalts. *Earth and Planetary Science Letters* **90**, 349–370.

Porter, S. (1981). Pleistocene glaciation in the Southern Lake district of Chile. *Quaternary Research* **16**, 263–292.

Portnyagin, M., Hoernle, K., Plechov, P., Mironov, N. & Khubunaya, S. (2007). Constraints on mantle melting and composition and nature of slab components in volcanic arcs from volatiles (H_2O, S, Cl, F) and trace elements in melt inclusions from the Kamchatka arc. *Earth and Planetary Science Letters* **255**, 53–69.

Putirka, K. D. (2008). Thermometers and barometers for volcanic systems. In: Putirka, K. D. and Tepley, F. I. (eds) *Minerals, Inclusions and Volcanic Processes*. Virginia: The Mineralogical Society of America, pp. 61–120.

Putirka, K. D. (2017). Down the crater: where magmas are stored and why they erupt. *Elements* **13**, 11–16.

Renne, P., Mundi, R., Balco, G., Min, K. & Ludwig, K. (2010). Joint determination of ^{40}K decay constant and $^{40}Ar^*/^{40}Ar$ for the Fish Canyon sanidine standard and improved accuracy for $^{40}Ar/^{39}Ar$ geochronology. *Geochimica et Cosmochimica Acta* **74**, 5349–5367.

Reubi, O. & Blundy, J. (2009). A dearth of intermediate melts at subduction zone volcanoes and the petrogenesis of arc andesites. *Nature* **378**, 571–578.

Reubi, O., Bourdon, B., Dungan, M. A., Koornneef, J. M., Sellés, D., Langmuir, C. H. & Aciego, S. (2011). Assimilation of the plutonic roots of the Andean arc controls variations in U-series disequilibria at volcan Llaima, Chile. *Earth and Planetary Science Letters* **303**, 37–47.

Roeder, P. L. & Emslie, R. F. (1970). Olivine-liquid equilibrium. *Contributions to Mineralogy and Petrology* **19**, 275–289.

Ruprecht, E. H., Bergantz, G. W., Cooper, K. & Hildreth, W. (2012). The crustal magma storage system of volcan Quizapu, Chile and the effects of magma mixing on magma diversity. *Journal of Petrology* **53**, 801–840.

Ruth, D. C. S., Cottrell, E., Cortés, J. A., Kelley, K. A. & Calder, E. S. (2016). From passive degassing to violent strombolian eruption: the case of the 2008 eruption of Llaima volcano, Chile. *Journal of Petrology* **57**, 1833–1864.

Salters, V. & Stracke, A. (2004). Composition of the depleted mantle. *Geochemistry, Geophysics and Geosystems* **5,** Q05B07,

Searle, M., Khan, M., Fraser, J., Gough, S. & Jan, M. (1999). The tectonic evolution of the Kohistan–Karakoram collision belt along the Karakoram highway transect, North Pakistan. *Tectonics* **18**, 929–949.

Sellés, D. & Moreno, H. (2011). Geologia del volcán Calbuco, Región de Los Lagos. In: Servicio Nacional de Geología y Minería Chile (ed.) *Geologia Basica No 130*. Santiago.

Sigmarsson, O., Chmeleff, J., Morris, J. & Lopez-Escobar, L. (2002). Origin of ^{226}Ra-^{230}Th disequilibria in arc lavas from Southern Chile and implications for magma transfer time. *Earth and Planetary Science Letters* **196**, 189–196.

Sisson, T., Ratajeski, K., Hankins, W. & Glazner, A. (2005). Voluminous granitic magmas from common basaltic sources. *Contributions to Mineralogy and Petrology* **148**, 635–661.

Sisson, T. W. & Bacon, C. R. (1999). Gas-driven filter pressing in magmas. *Geology* **27**, 613–616.

Sisson, T. W. & Grove, T. L. (1993). Experimental investigations of the role of H_2O in calc-alkaline differentiation and subduction zone magmatism. *Contributions to Mineralogy and Petrology* **113**, 143–166.

Stern, C. (2004). Active Andean volcanism: its geologic and tectonic setting. *Revista Geologica de Chile* **31**, 161–206.

Stern, C., Futa, K., Muehlenbachs, K., Dobbs, F., Muñoz, J., Godoy, E. & Charrier, R. (1984). Sr, Nd, Pb and O isotope composition of late Cenozoic volcanics, northernmost SVZ (33–34°s). In:Harmon, R. and Barreiro, B. (eds) *Andeam Magmatism. Chemical and Isotopic Constraints.* Nantwich: Shiva Publishing Limited, pp. 96–105.

Sun, S. & McDonough, W. (1989). Chemical and isotopic systematics of oceanic basalts: implications for mantle composition and processes. In: Saunders, A. and Norry, M. (eds.) *Magmatism in the Ocean Basins.* Geological Society, London, Special Publications 42, pp. 313–345.

Syracuse, E. M. & Abers, G. A. (2006). Global compilation of variations in slab depth beneath arc volcanoes and implications. *Geochemistry, Geophysics, Geosystems* **7**.

Syracuse, E. M., Van Keken, P. & Abers, G. (2010). The global range of subduction zones thermal models. *Physics of the Earth and Planetary Interiors* **183**, 73–90.

Tassara, A. & Echaurren, A. (2012). Anatomy of the Andean subduction zone; three dimensional density model upgraded and compared against global-scale models. *Geophysical Journal International* **189**, 161–168.

Tassara, A., Götze, H.-J., Schmidt, S. & Hackney, R. (2006). Three-dimensional density model of the Nazca plate and the Andean continental margin. *Journal of Geophysical Research* **111**, B09404.

Toplis, M. & Carroll, M. (1995). An experimental study of the influence of oxygen fugacity on Fe-Ti oxide stability, phase relations, and mineral-melt equilibria in ferro-basaltic systems. *Journal of Petrology* **36**, 1137–1170.

Toplis, M. & Corgne, A. (2002). An experimental study of element partitioning between magnetite, clinopyroxene and iron-bearing silicate liquids with particular emphasis on vanadium. *Contributions to Mineralogy and Petrology* **144**, 22–37.

Tormey, D., Hickey-Vargas, R., Frey, F. A. & Lopez-Escobar, L. (1991). Recent lavas from the Andean volcanic front (33–42 degrees S); interpretations of along-arc compositional variations. *Special Paper - Geological Society of America* **265**, 57–77.

Turner, S., Langmuir, C., Katz, R., Dungan, M. & Escrig, S. (2016). Parental arc magma compositions dominantly controlled by mantle-wedge thermal structure. *Nature Geoscience* **9**, 772–776.

Turner, S. J. & Langmuir, C. H. (2015a). The global chemical systematics of arc front stratovolcanoes: Evaluating the role of crustal processes. *Earth and Planetary Science Letters* **422**, 182–193.

Turner, S. J. & Langmuir, C. H. (2015b). What processes control the chemical compositions of arc front stratovolcanoes? *Geochemistry, Geophysics, Geosystems* **16**, 1865–1893.

Vigneresse, J.-L., Barbey, P. & Cuney, M. (1996). Rheological transitions during partial melting and crystallization with application to felsic magma segregation and transfer. *Journal of Petrology* **37**, 1579–1600.

Wada, I. & Wang, K. (2009). Common depth of slab-mantle decoupling: reconciling diversity and uniformity of subduction zones. *Geochemistry, Geophysics and Geosystems* **10**, Q10009.

Waters, L. & Lange, R. (2015). An updated calibration of the plagioclase-liquid hygrometer-thermometer applicable to basalts through rhyolites. *American Mineralogist* **100**, 2172–2184.

Watt, S. F. L., Pyle, D. M., Mather, T. A. & Naranjo, J. A. (2013). Arc magma compositions controlled by linked thermal and chemical gradients above the subducting slab. *Geophysical Research Letters* **40**, 2550–2556.

Wood, B. J. & Blundy, J. (1997). A predictive model for rare earth element partitioning between clinopyroxene and anhydrous silicate melt. *Contributions to Mineralogy and Petrology* **129**, 166–181.

Wörner, G., Mamani, M. & Blum-Oeste, M. (2018). Magmatism in the central Andes. *Elements* **14**, 237–244.

Yoder, H. (1976). *Generation of Basaltic Magma*. Washington DC: National Academy of Sciences.